UNIVERSITY OF CALIFORNIA
RIVERSIDE

Morphological Analysis of Galaxies in the CANDELS Fields

A Dissertation submitted in partial satisfaction
of the requirements for the degree of

Doctor of Philosophy

in

Physics

by

Laura Michelle DeGroot

August 2015

Dissertation Committee:

Dr. Bahram Mobasher, Chairperson
Dr. Brian Siana
Dr. Gillian Wilson

The Dissertation of Laura Michelle DeGroot is approved:

_____

_____

_____

Committee Chairperson

University of California, Riverside

Acknowledgements

I am grateful to everyone who made this Ph.D. dissertation possible. While a complete list of all people important to this process is not possible, there are a few people who immediately come to mind.

My advisor, Bahram Mobasher, provided me with many opportunities to work with various experts around the world as well as pushed me to take on new challenges such as leading the morphological study of galaxies in the MOSDEF survey. I thank Brian Siana and Gillian Wilson for serving on my thesis committee and providing me with critical feedback, as well as the rest of the astronomy department at UCR for all of the support throughout graduate school. Swara Ravindranath has also provided me with an amazing amount of knowledge and support in studying galaxy morphology, and helped me apply for the US-India Travel Grant Program through the American Physics Society, while also hosting me after receiving the award.

I thank my husband, Andrew, for all of his support throughout all of graduate school and especially in the last few months of dissertation research in the form of help with our family. I thank my son, Tristan, for providing enormous amounts of smiles and giggles to brighten my day after stressful days of dissertation writing. My amazing parents, Bob and Darlene, were incredibly supportive, in more ways than I can express, and I couldn't have completed this without them.

My friends have also played intricate roles in helping me achieve success in graduate school. Alexandra Saum was an amazing supporter over the years, even from far away, and without the support from all of my family and friends, this work would not have been possible.

Additionally, collaborations have provided unlimited opportunities for me to succeed in my dissertation research including the CANDELS collaboration and the MOSDEF survey. I'm thankful for the unlimited knowledge and opportunities I have received from both teams of astrophysicists.

ABSTRACT OF THE DISSERTATION

Morphological Analysis of Galaxies in the CANDELS Fields

by

Laura Michelle DeGroot

Doctor of Philosophy, Graduate Program in Physics
University of California, Riverside, August 2015
Dr. Bahram Mobasher, Chairperson

Knowledge of the morphology of galaxies is essential in studying galaxy formation and evolution. When combined with other observable characteristics, a detailed understanding of the properties of galaxies can be acquired. In this study, I analyze parametric morphology using the code GALFIT of two galaxy samples in the CANDELS fields by applying a single Sérsic function and a two-component fit to the surface brightness distribution of the galaxies. I quantify morphological properties, such as galaxy Sérsic index, bulge-to-total flux ratio, and size to study the evolution and correlation with other galaxy properties. When my parametric measurements are compared with non-parametric techniques, such as the Gini-M_{20} diagram, I find that the different methods show overall agreement.

I find that galaxies selected with MIPS 24 μm detection, characteristic of dusty, star-forming galaxies, in the GOODS-S field are primarily disk galaxies with a range of bulge fractions, although some galaxies with elliptical profiles are present. Many of these galaxies have AGN candidates, another source of 24 μm emission, while the remaining elliptical galaxies could contain obscured AGN. In comparison, I find that galaxies without 24μm emission are primarily disks but with a larger sample of elliptical galaxies that show an observed evolution is bulge-dominance with redshift.

For galaxies observed in the MOSDEF survey, I find little to no correlation between the relations of SFR-M_* and MZR with galaxy n. The star forming main sequence is observed to form a tighter, steeper correlation for galaxies with low B/T than other populations indicating that higher mass, disky galaxies have higher SFRs with smaller bulge fractions. This relation also shows that galaxies with high B/T have much flatter slopes indicating that they may be evolving to quiescence. I examine the necessity for a morphological k-correction when studying morphology across multiple redshifts, and discover that galaxy n and r_e show wavelength dependence when comparing observed optical and infrared morphologies, while the B/T shows significant scatter in all wavelengths and redshifts. Overall I find that a morphological k-correction is necessary when studying galaxies across a wide redshift range.

Contents

List of Figures

List of Tables

Chapter 1

Introduction

Galaxy morphology, represented by the distribution of star light, gas and dust, has long been studied through various methods. The most notable study of galaxy structure began with Hubble (1926), who performed visual classifications of galaxies using photographic plates. Depending on their appearance galaxies were placed into one of three main categories: elliptical, spiral, or irregular. The "Hubble Tuning Fork" was established as a possible evolution scenario where late-type spiral galaxies eventually evolved into the early-type, or elliptical, galaxies (Hubble, 1936; Sandage, 1961). With advancements in technology, observations transitioned from photographic plates to charge-coupled devices (CCD) enabling pixel-by-pixel analysis of the surface brightness distribution of galaxies. Galaxy morphology quickly transitioned from a qualitative visual classification to more quantitative approaches in representing and analyzing the galaxy light distribution. New techniques have emerged including parametric and non-parametric approaches to determining galaxy type, summarized in Section 1.2 with further detail in Chapter 2, which have led to a better understanding of galaxy formation and evolution.

1.1 A Brief Introduction to Galaxy Morphology

Galaxy structure provides one of the most fundamental ways of observing galaxy properties as well understanding galaxy evolution. One of the major criteria for distinguishing different

Hubble Type galaxies is star formation. It is well known that at higher redshifts, $z > 1$, there is a well-defined relation between star-formation rate and stellar mass of a galaxy, such that higher-mass galaxies have a higher rater of star formation (Noeske et al., 2007; Bauer et al., 2011; Conselice, 2014). This relation is important to morphology, in that galaxies with ongoing star formation can have very different structure, such as star forming knots and spiral features, compared to passive galaxies. Another well-known relation is between the stellar mass and metallicity of galaxies indicating that galaxies with lower stellar mass have lower metallicity than those with higher M_* (Tremonti et al., 2004; Kewley and Ellison, 2008; Andrews and Martini, 2013), although it has been found to evolve with redshift in that a given stellar mass will have a lower metallicity at higher redshift (Erb et al., 2006; Maiolino et al., 2008; Henry et al., 2013; Maier et al., 2014; Maseda et al., 2014; Steidel et al., 2014; Sanders et al., 2015). Since metallicity correlates with mass and therefore star formation, the galaxy morphology should also have a metallicity dependence that would evolve with time. It has also been found that morphological *k*-correction effects exist for galaxies due to the fact that at shorter wavelengths the morphologies and quantitative structures are tracing the distribution of star formation directly (Windhorst et al., 2002; Taylor-Mager et al., 2007). Dusty galaxies can also have a significant fraction of their light absorbed, leading to differences in their observed morphological properties. All of these galaxy characteristics infer that overall morphology, including more detailed structure, and spectral features are correlated, and since these various properties evolve with time, the galaxy structure must also show evolution. Not only due changes in star formation activity and other galactic properties affect the overall morphology, but interactions with other objects, including merging, can affect the bulge growth, shape, and detailed structure of a galaxy. The structure provides a way to examine how galaxies are assembled, when combined with observed qualities, as it permits us to determine which modes of formation are active within a galaxy (Conselice, 2014). By observing galaxy morphology at different rest-frame wavelengths, and comparing these measurements to observed characteristics such as star formation, metallicity, stellar mass, and other spectral properties, a more detailed understanding of galaxy formation and evolution scenarios can be achieved. In order to complete

this comparison, accurate measurements of morphology must first be completed. There are a wide variety of methods used to achieve accurate measurements of different galaxy types and structural properties, all providing an accurate measure of galaxy morphology.

1.2 Morphological Techniques

Over the years, many different methods have been developed to determine galaxy morphology. Original classifications completed using photographic plates offered new information into galaxy formation and evolution, but with further advancements in technology more quantitative analyses are now possible. Here I give an overview of the various techniques developed since Edwin Hubble's 1926 Classification of Nebulae into various Hubble Types (Hubble, 1926).

1.2.1 Visual Morphologies

The Hubble Tuning Fork, or Hubble's classification scheme shown in Figure 1.1, roughly separates galaxies into two broad types, elliptical and spiral galaxies (Hubble, 1936; Sandage, 1961). Elliptical galaxies were identified by their ellipticity, $e = 1 - b/a$, where b and a are respectively the semi-minor and semi-major axis from the surface brightness profile. Elliptical galaxies were given a classification of En, where $n = 0, 1, 2, 3, ..., 7$. In this classification a galaxy with $n = 0$ is a round, low-ellipticity elliptcal, and $n = 7$ is a highly elliptical galaxy. Spiral galaxies were separated into two classes, those with and without a central bar component, leading to the tuning fork shape of the Hubble scheme. All spirals were found to have a high ellipticity, $e > 0.7$, and there were three additional criteria that separated out the spiral galaxies along each class from each other: the relative size of the central bulge component, the extent to which the spiral arms are unwound, and the degree of resolution of the spiral arms (Hubble, 1922, 1926). This general classification scheme is still widely used today, and has lead to the continued study of galaxy structure.

With advancements in technology, collaborative visual morphology classifications can independently be performed. Projects like *Galaxy Zoo* (Lintott et al., 2008) provide a web-based

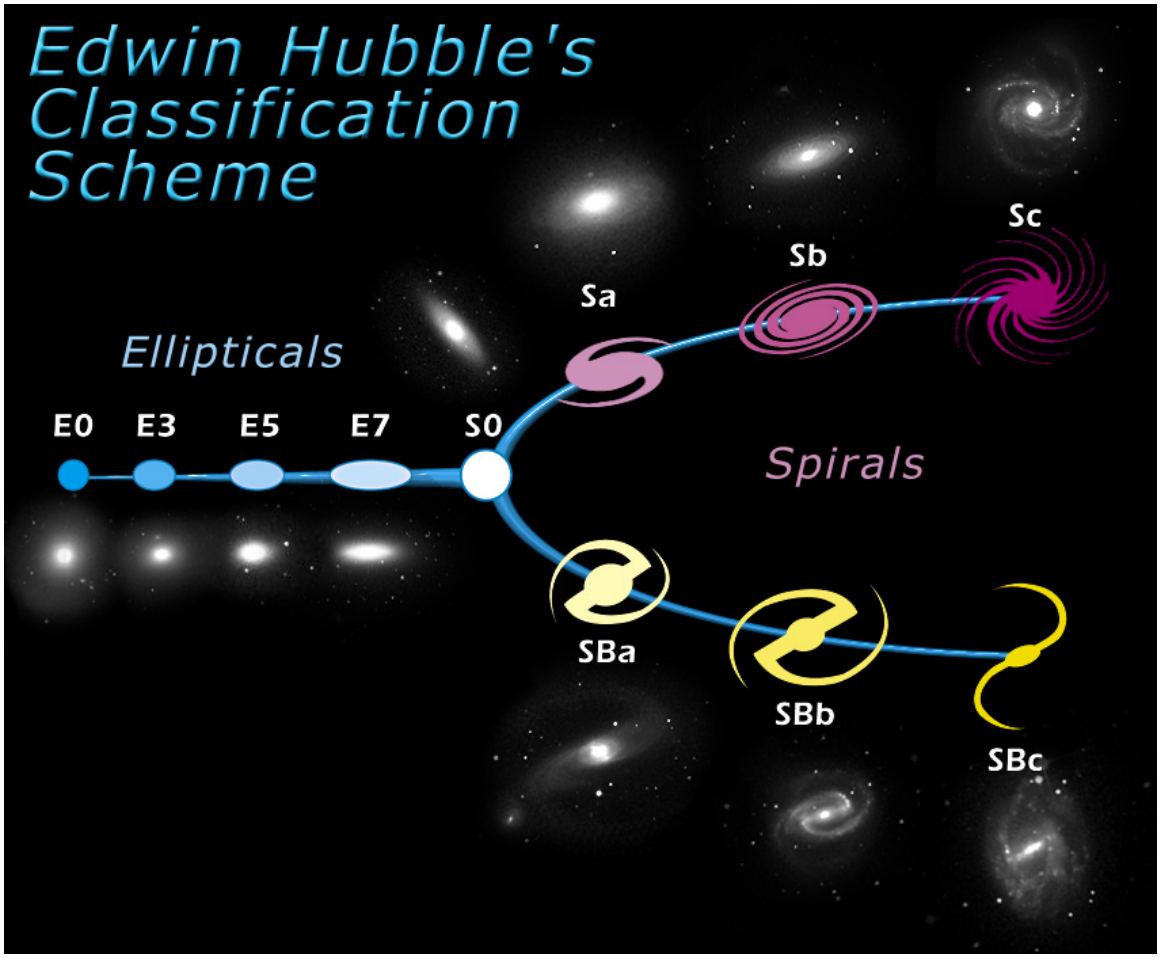

Figure 1.1: Edwin Hubble's classification scheme of galaxies developed in 1926. The diagram is roughly divided into two main categories: elliptical galaxies and the tuning fork is composed of spiral galaxies with and without bars. Ellipticals are classified based on their ellipticity where 0 is round, while 7 is highly elliptical, and spirals classified from a-c are characterized on the compactness of their arms. In addition, there are also irregular galaxies that do not lie along the tuning fork of the Hubble Classification Scheme. (Image by ESA/Hubble (M. Kornmesser))

visual morphology classification scheme that allows astronomers, amateur and professional, from around the world to participate in a collaborative morphology project. Other large astronomy collaborations, such as the Cosmic Assembly Near-Infrared Deep Extragalactic Legacy Survey (CANDELS; Grogin et al., 2011; Koekemoer et al., 2011) provide another perspective on collaborative morphology. In this study, 65 team members have visually classified all galaxies in the five CANDELS fields down to a limiting magnitude of $H < 24.5$. The classifications were completed on a GUI plaltform, and to ensure accurate results and for the consistency of

classifications, each galaxy was classified by a minimum of three classifiers. Training sets were developed to make sure that classifiers were familiar with the scheme, and information is obtained about galaxy type, interactions, and clumpiness. For more information about the first release of the CANDELS visual classifications see Kartaltepe et al. (2014). While visual morphology can provide information about galaxies that is hard to obtain through an automated computer routine, the results are often hard to replicate, the method is subjective, and quantitative values are not available to statistically compare the results.

1.2.2 Non-parametric Morphologies

Non-parametric morphology is a quantitative method of classifying galaxy surface brightness profiles without assuming an analytical function for the galaxy's light distribution (Lotz et al., 2004). These techniques are easily applied to irregulars as well as the standard Hubble-type galaxies. Below we summarize the main non-parametric morphology determination methods found in literature.

1.2.3 Petrosian Radius

The Petrosian radius r_p is defined as the radius at which the ratio of the surface brightness at r_p to the mean surface brightness within r_p is equal to a fixed value (Petrosian, 1976). This is given by the equation

$$\eta = \frac{\mu(r_p)}{\overline{\mu}(r < r_p)}, \tag{1.1}$$

where η is typically set to 0.2. The measurement of r_p is based on a curve of growth, which is insensitive to variations in the limiting surface brightness and S/N. The Petrosian radius is used to set the the flux threshold for pixels assigned to a galaxy, which enables accurate and consistent measurements of other non-parametric morphologies. This is the radius typically used for all non-parametric techniques.

CAS: Concentration, Asymmetry, and Clumpiness

A widely used non-parametric morphology method is from the CAS (Conselice, 2003), which makes no assumptions about the underlying form of the galaxy structure but aims to capture the major features.

The concentration index (C; Bershady et al., 2000; Conselice et al., 2003) of a galaxy is determined by taking the ratio of the radius containing 80% of a galaxy's light, r_{80}, to the radius at which 20% of the galaxy's light is contained, r_{20},

$$C = 5\log\left(\frac{r_{80}}{r_{20}}\right), \tag{1.2}$$

where r_{20} and r_{80} are Petrosian radii described above. Morphologically, a high concentration value indicates that the light is concentrated towards the center of the galaxy similar to bulge-dominated spiral galaxies (early-type spirals), point sources, and elliptical galaxies, while low concentration values are indicative of late-type spiral galaxies with weak or no bulge (Peth et al., 2015).

The asymmetry of a galaxy (A; Conselice et al., 2000), measures the difference between a galaxy image, and the galaxy's image rotated 180 degrees. The basic formula for calculating the asymmetry index is

$$A = \min\left(\frac{\sum|I_0 - I_{180}|}{\sum|I_0}\right) - \min\left(\frac{\sum|B_0 - B_{180}|}{\sum|I_0}\right) \tag{1.3}$$

where I_0 is the original galaxy image, I_{180} is the image rotating 180 degrees along the line-of-sight center axis of the galaxy, and B_0 and B_{180} are the background in a blank area of the image and the background after 180 degree rotation. Elliptical galaxies tend to be very symmetrical giving low asymmetry values (A $\sim$ 0.02), spiral galaxies have values between A $\sim$ 0.07 and 0.20 (Conselice, 2014), and A is most sensitive to irregular galaxies, which have A $\gtrsim$ 0.3 for mergers remnants (Conselice et al., 2003).

Clumpiness (S), otherwise known as the smoothness parameter, is used to describe the frac-

tion of light that is contained in clumpy distributions (Conselice, 2003, 2014). Elliptical galaxies are rather smooth systems with low S values, while galaxies with ongoing star formation and HII regions tend to have very clumpy structures with high S values. S is determined using the equation

$$S = 10 \times \left[\frac{\sum(I_{x,y} - I^{\sigma}_{x,y})}{\sum I_{x,y}} - \frac{\sum(B_{x,y} - B^{\sigma}_{x,y})}{\sum I_{x,y}} \right], \tag{1.4}$$

where $I_{x,y}$ is the original image, $I^{\sigma}_{x,y}$ is the blurred image, σ is the smoothing kernel, and similar for the background, B.

Gini Coefficient

The Gini coefficient is a statistic based on the Lorenz curve, the rank-ordered cumulative distribution function of a population's wealth, which has been translated for astronomical use as a function of a galaxy's pixel values (Abraham et al., 2003; Lotz et al., 2004; Peth et al., 2015). The Lorenz curve is given by

$$L(p) = \frac{1}{\overline{X}} \int_0^p F^{-1}(u) du \tag{1.5}$$

where p is the percentage of the faintest pixels, $F(x)$ is the cumulative distribution function, and $\overline{X}$ is the mean over all pixel flux values (Lorenz, 1905). The Gini Coefficient (G) is then determined by the ratio of the Lorenz curve and the curve of "uniform equality" (where $L(p) = p$) and the area under the curve of uniform equality. The pixels are ranked in increasing flux value, and G is then determined by

$$G = \frac{1}{\overline{X} n(n-1)} \sum_i^n (2i - n - 1) X_i, \tag{1.6}$$

where n is the number of pixels in a galaxy's segmentation map and X_i is the pixel flux at the rank i pixel. The light is equally distributed similar to an elliptical galaxy for G close to 0, while for G closer to 1 a larger fraction of light will be concentrated on fewer pixels similar to disk galaxies with bright, central bulges (Peth et al., 2015).

M_{20}: Second-order Moment

The second-order moment of the brightest regions of a galaxy (M_{20}; Lotz et al., 2004) traces the spatial distribution of any bright clumps. This parameter is similar to the concentration index in that it gives a value indicating if the light is concentrated within an image (Conselice, 2014). M_{20} is best used in combination with G for galaxy morphology in being an effective tool in differentiating galaxies with off-center clumps compared to those with bright, dominant central bulges. The second-order moment is calculated using the form

$$M_{20} = \log\left(\frac{\sum_i M_i}{M_{tot}}\right), \text{ where} \tag{1.7}$$

$$M_{tot} = \sum_i^n M_i = \sum_i^n f_i[(x_i - x_c)^2 + (y_i - y_c)^2], \text{ and} \tag{1.8}$$

$$\sum_i f_i < 0.2 f_{tot}. \tag{1.9}$$

Here M_{tot} is the total second-order moment, f_i is the flux in each pixel at position x_i and y_i, and x_c and y_c are the galaxy's center. Values for M_{20} range between -0.5 and -2.25. Elliptical galaxies have values closer to -0.5 indicating a lack of off-center bright clumps, while disk galaxies tend to have $M_{20} < -1.6$ due to bright star-forming knots (Peth et al., 2015; Lotz et al., 2004).

MID Statistics: Multi-Mode, Intensity, and Deviation

These three new statistics presented in Freeman et al. (2013) are intended to identify galaxies with disturbed morphologies, such as merging systems. The Multi-Mode Statistic (M) is the ratio of the two brightest regions of the galaxy, in pixels. Brightest regions are determined through a threshold method where q_l, the intensity quantile, denotes the normalized flux value, and l is the percent of pixel intensities inside a segmentation map smaller than the value of q_l. This is then represented in a binary value where 1 represents fluxes larger than q_l in the map, while 0

denotes those with fluxes less than q_l (Eq. 1.10). This results in the definition of a new image,

$$g_{i,j} = \begin{cases} 1 & f_{i,j} \geq q_l \\ 0 & \text{otherwise} \end{cases}, \tag{1.10}$$

where $f_{i,j}$ is the observed flux at pixel (i, j). This resulting image will be primarily 0, but there will be m groups with values of 1. For these groups, the number of pixels are determined in a group, $A_{l,m}$, which are then put in descending order by area. The two largest groups define an area ratio

$$R_l = \frac{A_{l,(2)}}{A_{l,(1)}} A_{l,(2)}. \tag{1.11}$$

The ratio is sensitive to noise, so it is multiplied by $A_{l,(2)}$, which tends towards 0 if the second group is noise dominated. This overall area ratio tends towards 1 if double nuclei are present, and 0 if not. The maximum value of the area ratio then gives the M statistic

$$M = \max R_l. \tag{1.12}$$

The next statistic, Intensity (I), is the flux ratio of the two brightest regions. To calculate the intensity, the image must first be smoothed by a bivariate Gaussian kernel, and using maximum gradient paths, regions are defined consisting of pixels linked to a unifying local maximum. The fluxes within these groups are summed and sorted in descending order resulting in the intensity ratio:

$$I = \frac{I_{(2)}}{I_{(1)}} \tag{1.13}$$

When I $\sim$ 0, this is indicative of an object with a bright central bulge, like an elliptical galaxy, while late-type spiral galaxies with have an intensity ratio of I $\sim$ 1 (Peth et al., 2015).

The final component of the MID statistics is deviation (D), which measures the distance between the intensity centroid of a galaxy and center of the brightest region. For disk or spheroidal galaxies, the brightest region tends to be the center of the galaxy giving a deviation value of $D \sim 0$, but a higher D value indicates that bright star forming knots could exist within the galaxy.

The intensity centroid of the galaxy is defined as

$$(x_{cen}, y_{cen}) = \left(\frac{1}{n_{seg}} \sum_i \sum_j i f_{i,j}, \frac{1}{n_{seg}} \sum_i \sum_j j f_{i,j} \right), \tag{1.14}$$

with the summation over n_{seg} pixels within the SExtractor segmentation map (Bertin and Arnouts, 1996). The distance from (x_{cen}, y_{cen}) to the maximum associated with $I_{(1)}$, is then normalized for the galaxy radius, giving the final D statistic of:

$$D = \sqrt{\frac{\pi}{n_{seg}}} \sqrt{(x_{cen} - x_{I_{(1)}})^2 + (y_{cen} - y_{I_{(1)}})^2} \tag{1.15}$$

This statistic was specifically designed to capture evidence of galaxy asymmetry. More detailed discussion about the MID statistics can be found in Freeman et al. (2013), as well as further applications in Peth et al. (2015).

1.2.4 Parametric Morphologies

Parametric morphological studies describe a galaxy by modeling the distribution of light as projected into the plane of the sky with a prescribed analytic function (Lotz et al., 2004). Surface brightness profiles have long been quantified using $R^{1/4}$ light distributions for elliptical galaxies (de Vaucouleurs, 1948, 1953) and an exponential profile for disks of late-type, spiral galaxies (Patterson, 1940; de Vaucouleurs, 1956). Parametric functions have become standard in describing galaxy morphology, due to the nature of quantitative morphology, in that the results are reproducible and any biases can be well understood (Marleau and Simard, 1998). These aspects make quantitative morphology advantageous over visual classifications, and enable morphological analysis of more distant, high-redshift galaxies. Quantitative morphology takes two general types of galaxy fitting. There are analyses that perform one-dimensional fitting of surface brightness profiles, and the more commonly used two-dimensional fitting of galaxy images. One-dimensional methods are simple to implement, but there is always the possibility that galaxies may have different profiles along their major and minor diameters (Ferrarese et al., 1994),

and instead most studies rely on two-dimensional fitting algorithms. We choose to fit an analytic function to model galaxy morphology of the samples analyzed in this work.

In Chapter 2, I present the different parametric codes available for measuring galaxy morphology as well as the technical aspects I use in these measurements, and I perform a comparison of non-parametric and parametric morphologies in Chapter 3. In Chapter 4, I examine the morphology of a sample of MIPS 24 μm detected galaxies in the GOODS-S field using HST observations. Chapter 5 investigates how galaxy morphology compares with other galaxy properties including star-formation rate, stellar mass, and metallicity. Finally, Chapter 6 summarizes the most important findings.

Chapter 2

Quantitative Morphology Measurements

2.1 Introduction

Deep multi-wavelength surveys are essential for understanding of the formation and evolution of galaxies. In particular, the high resolution imaging completed by the Hubble Space Telescope (HST) have enabled detailed image analysis important to the study of galaxy morphology. While visual classifications are useful in explaining the structure of a galaxy's light profile qualitatively, it is very limited in its repeatability as well as to only nearby, highly-resolved objects. In order to extend morphological studies to higher redshifts, quantitative approaches are necessary. Throughout this work, I measure quantitative morphology of different galaxy samples with high resolution imaging in a parametric approach. Here we summarize quantitative, parametric analyses of galaxy morphology available, as well as the approach that we take throughout this work.

2.2 Morphology Measurements

2.2.1 Sérsic Function

It was originally shown by de Vaucouleurs (1948) that many elliptical galaxies follow an $r^{1/4}$ light distribution dependence known as the deVaucouler's $R^{1/4}$ function. Disk galaxies were instead found to follow an exponential profile describing their light distributions (Patterson, 1940; de Vaucouleurs, 1956). These profiles were generalized into a function by J.L. Sérsic called the Sérsic function, which is frequently used today to model the overall light distribution of galaxies (Sersic, 1968). This function describes the surface brightness of a galaxy and takes the form of:

$$\Sigma(r) = \Sigma_e \exp\left[-\kappa\left(\left(\frac{r}{r_e}\right)^{\frac{1}{n}} - 1\right)\right], \tag{2.1}$$

where Σ_e is the surface brightness within the effective radius, r_e, n is the Sérsic index, and κ is the correction factor that is coupled to n so that half of the total flux of the object lies within the effective radius. This generalized function is applicable to the surface brightness profile of galaxies, and can be used to distinguish different galaxy populations. When $n < 1$ the surface brightness profiles of galaxies are shallower at inner radii, and fall off rapidly with increasing radius. On the other hand, galaxies with $n > 1$ have steep inner profiles and level off at larger radii. Due to large differences in the surface brightness profiles of galaxies above and below $n = 1$, different physical mechanisms including formation, evolution, and interactions would be expected for systems with different n values (MacArthur et al., 2003).

2.2.2 Bulge-Disk Decomposition

Galaxy structure is much more complicated than a single surface brightness profile, and it is also known that bulges of spiral galaxies follow the $r^{1/4}$ power law, while the flattened, rotationally

supported disk are consistent with an exponential profile (Freeman, 1970), taking the form:

$$\Sigma(r) = \Sigma_0 \exp\left(-\frac{r}{r_s}\right), \tag{2.2}$$

where Σ_0 is the central surface brightness and r_s is the disk scale length, which relates to the effective radius presented in the general Sérsic function as

$$r_e = 1.678 r_s, \tag{2.3}$$

for $n = 1$ profiles only. Alternate descriptions of bulges of disk galaxies were later proposed in that bulges of late-type spiral galaxies, those with less prominent bulges, followed exponential forms, but the bulges of early-type spirals still seemed to follow closer to the $r^{1/4}$ law (Kent et al., 1991; Andredakis and Sanders, 1994; Andredakis et al., 1995). Since this realization, other studies have found that the $r^{1/4}$ profile of bulges holds as long as all bulges of disk galaxies are indeed classical bulges formed through violent processes, which would be similar to scaled ellipticals with a surrounding disk, however, not all bulges are formed through the same process. Secular processes and disk instabilities can lead to slower bulge formation creating pseudo-bulges that are formed over much longer time-scales (Wyse et al., 1997; Kormendy and Kennicutt, 2004; Gadotti, 2009). In order to accurately model the surface brightness profile of galaxy bulges and disks, one must allow a range of bulge profiles to take into account different formation and evolution scenarios, which is why in this work I complete bulge-disk decompositions of galaxies using an exponential disk profile ($n = 1$), as is done classically in other studies, and a Sérsic function for the bulge component of the galaxy where the Sérsic index, n, is a free parameter within the range of $0.2 < n < 8.0$. These concepts are all applied today into parametric morphology measurements of nearby and distant galaxies through many different techniques. Here we describe some of the codes available for completing parametric galaxy morphology.

2.3 Parametric Morphology Techniques

Parametric morphology models the light distribution of galaxies by assuming an analytic function to describe the galaxy surface brightness enabling a quantitative method of determining the galaxy morphology. There are many publicly available codes to measure parametric morphology. Here we list many of these codes that have been developed to complete two-dimensional galaxy surface brightness fits.

GIM2D, GASP2D, GASPHOT, and BUDDA

GIM2D (Galaxy Image Two-Dimensional) is a two-dimensional decomposition fitting program written to perform detailed surface brightness profile decompositions of galaxies in a fully automated way (Simard, 1998; Marleau and Simard, 1998). This IRAF package fits a maximum of 12 different parameters in decomposing galaxies into their bulge and disk components. It measures the total flux of the galaxy, the bulge-to-total flux ratio (B/T), the effective radius of the bulge component r_e, the ellipticity of the bulge component ($e = 1 - b/a$), the bulge position angle in the sky, the scale length of the disk component r_d, the inclination of the disk, the disk position angle, x and y offsets of the galaxy center, the background level, and the galaxy Sérsic index n. The code models the galaxy bulge with a Sérsic profile, and the disk with an exponential form.

GASP2D (GAlaxy Surface Photometry 2 Dimensional Decomposition), similar to GIM2D, is a two-dimensional automated fitting algorithm that adopts a Levenberg-Marquardt algorithm to fit the two-dimensional surface brightness of galaxies. This Interactive Data Language (IDL) code assumes surface brightness profiles to be the sum of a bulge and disk component described by elliptical isophotes with constant ellipticity and position angle on the sky. A Sérsic law is used to describe the bulge profile, while an exponential law is used to model the disk component of the galaxy. GASP2D takes into account seeing affects by convolving the model with a circular two-dimensional Gaussian point-spread function (PSF), which has a full-width half maximum (FWHM) chosen to match foreground stars in images. The code is based on χ^2 minimization

technique, and the galaxy model convolved with the PSF is subtracted from the original image to show the residual (Méndez-Abreu et al., 2008).

The photometry package GASPHOT (Galaxy Automatic Surface PHOtometry Tool) is aimed to determine reliable global parameters for large galaxy samples, while substantially reducing the amount of interaction for the user. GASPHOT is a hybrid 1D/2D approach to modeling galaxies with a single Sérsic law to quantify the galaxy morphology in an automated method. Instead of being a classic 2D approach (like GIM2D and GASP2D), GASPHOT uses more of a 1D approach similar to the IRAF-ELLIPSE package (Jedrzejewski, 1987). The 1D approach makes the fitting less sensitive to peculiar features of galaxies, while the 2D approach is well suited for accurate modeling of well-sampled objects. It uses a 1D technique while still implementing a PSF convolution, and it uses χ^2 method to test goodness of the fit. For details about GASPHOT see Pignatelli et al. 2006.

BUDDA (BUlge/Disk Decomposition Analysis) is a FORTRAN code that, like GIM2D and GASP2D, performs two-dimensional bulge and disk decompositions of galaxies. This code also fits the bulge component with a Sérsic profile and the disk with an exponential, while also taking into account atmospheric seeing by applying a Gaussian smearing (similar to a PSF convolution) of the brightness profile, which only affects the very center of the profile. The code iterates until it reaches the smallest χ^2 value, resulting in a total of 11 fit parameters: x and y position, central effective surface brightness for the bulge and disk, position angle of the bulge and disk, bulge and disk ellipticity, bulge effective radius, and disk scale length, h (de Souza et al., 2004).

Many similarities exist between these various 2D or hybrid 1D/2D surface brightness modeling codes, which have been developed for different programming languages. Many complications exist in installing as well as implementing these codes, which makes them less user friendly even if they provide a very robust, automated method for analyzing galaxy morphology. Another code exists that is extremely user friendly with excellent technical support that is most commonly used to analyze galaxy morphology.

GALFIT

GALFIT (Peng et al., 2002, 2010) is a two-dimensional image decomposition program written in the C language, however, this code is packaged as a binary for a wide variety of operating systems making it easy to use. Installation is not necessary as the binary can be used from the directory that it is placed in, making Galfit one of the most widely used surface brightness modeling codes. This two-dimensional fitting routine can model the surface brightness profile of an observed galaxy using a variety of functions, including a Sérsic function, exponential disk, DeVaucouleur's $r^{1/4}$ profile, and many more. The code takes into account atmospheric seeing by convolving the galaxy model with a PSF input by the user. GALFIT also offers the ability to simultaneously fit as many profiles as necessary to reach a good surface brightness model, although too many profiles can be very computationally expensive. Just like GASP2D, the algorithm adopts a Levenberg-Marquardt algorithm to fit the two-dimensional surface brightness of galaxies, and determines the goodness of fit using a χ^2 minimization. GALFIT combines many aspects of the above codes in that it can fit a single Sérsic profile to galaxies or more complicated, multi-profile fits. The flexibility of the code application as well as ease-of-use makes GALFIT one of the most commonly used codes to analyze galaxy morphology parametrically. Throughout this work, I use GALFIT to analyze the 2D surface brightness profiles of galaxies for single component fits as well as bulge-disk decompositions.

2.4 Measuring morphologies with GALFIT

2.4.1 Technical Aspects

Galaxy morphology is determined by modeling the two-dimensional surface brightness distribution with a Sérsic function. This is done using GALFIT (Peng et al., 2002, 2010), which convolves the 2D analytical model with the PSF using the Levenberg-Marquardt algorithm for χ^2 minimization giving the optimum fit. In order to consistently compare galaxy properties at different redshifts, we measure their Sersic parameters at the same rest-frame wavelength.

Galfit requires individual postage stamps for each of the galaxies, and the optimum size of a postage stamps must be determined to enclose the total light of the galaxy without being too large and computationally expensive. Postage stamp sizes are determined using the same technique as in the program GALAPAGOS (Galaxy Analysis over Large Areas: Parameters Assessment by GALFITting Objects from SExtractor, see Barden et al. 2012 for further details about GALAPAGOS). This was done using parameters from SExtractor and calculated using the following criteria.

$$X_{size} = 3.0a \cdot kron\,(|sin(\theta)| + (1-e)|cos(\theta)|)\,, \tag{2.4}$$

$$Y_{size} = 3.0a \cdot kron\,(|cos(\theta)| + (1-e)|sin(\theta)|)\,, \tag{2.5}$$

where a is the output parameter semi-major axis, $kron$ is the $Kron$ Radius, which is the typical size of the aperture that creates a ring or ellipse around object, θ is position angle in the sky, and e is the ellipticity calculated using the semi-major, a, and semi-minor, b, axes through the equation $e = \frac{a-b}{a}$. When modeling the light distribution of a galaxy it is important to include all of the light of the target galaxy as well as enough background sky pixels to accurately measure the total flux of the galaxy, but be a reasonable size as to keep the total fitting time from being excessive, and postage stamp sizes designed using these criteria are able to achieve this.

Background estimation is another very important step in using Galfit to accurately measure galaxy morphology. It has been found in previous studies that obtaining a precise measurement of the sky level is the most critical systematic in galaxy surface brightness profile fitting (de Jong, 1996; Barden et al., 2012; Häussler et al., 2007). Ideally, Galfit has the ability to include the sky as a free parameter while modeling the galaxy profile, but in order to do so the image must be as a large as possible to include the flux of the target galaxy, the majority of the flux of any surrounding galaxies, and a large amount of empty sky pixels, which may not always be feasible. Large postage stamps also become very computationally expensive once too many neighboring sources are included. We instead use a fixed sky value as obtained using a flux growth method. In this method, neighboring galaxies are masked out using elliptical apertures, as shown in Figure 2.1, and elliptical annuli centered around the object of interest are used to measure the

average background flux. As a function of radius, this background flux is determined, and when the slope of the average flux vs. radius graph levels off, the background sky is determined from those last few annuli (Barden et al., 2012). This ensures an accurate background measurement that is more robust than the typical value obtained from SExtractor. Another important step in running GALFIT is creating masks to remove contamination from nearby galaxies. In order to do this, ellipses were created using SExtractor (Bertin and Arnouts, 1996) parameters and enlarged to enclose all of the galaxy light. This is done for all of the objects in an enlarged postage stamp. Any object whose ellipse overlaps with the ellipse of the primary object is fitted simultaneously using a Sérsic profile. The remaining ellipses that did not overlap were used to mask out the additional objects during the fit (Barden et al., 2012; Häussler et al., 2007).

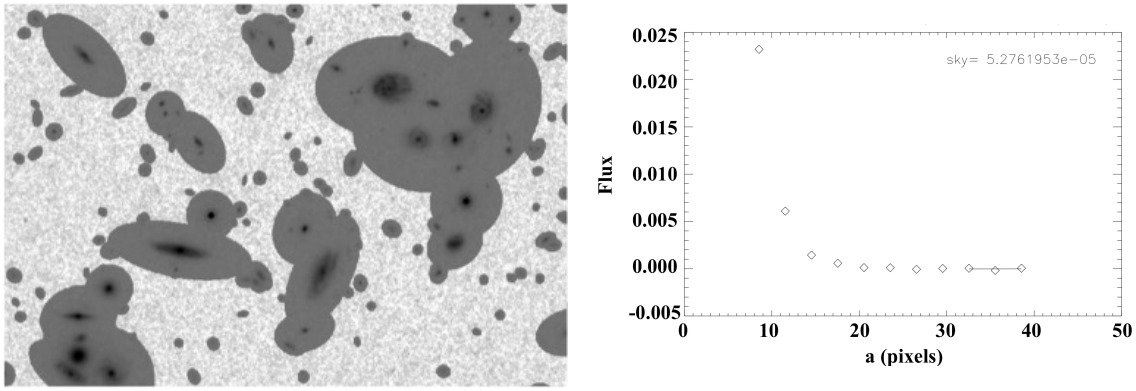

Figure 2.1: Determination of background estimation for running Galfit 2D surface brightness modeling. (Left) Ellipses used to mask out light of surrounding galaxies. If ellipses are found to overlap ellipse of target galaxy, these galaxies are fit simultaneously. (Right) Flux growth curve for measuring background value After galaxies are masked out using ellipses from the left image, elliptical annuli are used to determine the background value. The average flux value is determined in each annuli and when the profile plateaus for the second time, the background value is determined from the final three measurements.

The input parameters for GALFIT for each galaxy include position, total magnitude, effective radius or scale length, Sérsic index, ellipticity, position angle, and the sky background at the center of the fitting region. Input values for total magnitude, effective radius, ellipticity and position angle are taken from the SExtractor catalogs, which are good estimates of the galaxy photometry. Galfit also convolves the modeled galaxy Sérsic function with a point-spread function (PSF), which is either measured from star-stacked PSFs or by using the IRAF DAOPHOT

program (Stetson, 1987). For further details about using IRAF DAOPHOT to create PSFs are described in the Appendix. A constraint file is used to limit the central x and y position of the galaxy within 3 pixels of the input position, and to also restrict the Sérsic index to a desired range, $0.2 < n < 8.0$ for this work.

For the single Sésic function fit to the galaxy sample, the output parameters include total magnitude, effective radius, r_e, the Sérsic index, n, ellipticity, and position angle. The Sérsic index, a measure of the concentration of the light profile, is constrained between the values of 0.2 and 8.0 in order to avoid arbitrarily large values caused by active galactic nuclei (AGN) or compact, central point sources (Ravindranath et al., 2006). Goodness of fit is also determined using two main parameters, the reduced χ^2 and the ratio of the error in the effective radius, r_e, and the actual r_e value. Those with large χ^2 errors and large r_e errors relative to the effective radius, as well as objects that have been flagged for unreliable measurements by Galfit, are rejected after fitting. We typically reject galaxies with $\chi^2 > 5.0$ and if $\frac{r_e error}{r_e} > 0.2$. Most often rejected galaxies are double nuclei, low surface brightness, or extended objects.

In addition to the overall galaxy Sésic function fit with GALFIT, morphological classifications are also completed using a two-component fit of the bulge and disk of the galaxy simultaneously. I use the same procedure described above for including masks, background measurements, and postage stamp creation. In order to account for the two components separately, I fit a Sérsic function to the bulge, where the Sésic index, n, is a free parameter ranging between 0.2 and 8.0, and the disk is fit using an exponential disk, where the Sésic index is fixed to $n = 1$. All other parameters (total magnitude, r_e or r_s, axis ratio, and position angle) are allowed to vary independently. The input parameters are determined in the same manner as for a single-component fit, however we initially input a ratio of $r_{e,b}/r_{e,d} = 0.4$, where b represents the bulge and d represents the disk. This enables the determination of an initial input scale length from the disk using the relation $r_e = 1.678 r_s$ (Peng et al., 2010). A two-component fit adds additional free parameters resulting in larger errors, so a reliable bulge-disk decomposition is harder to accomplish, but from these measurements we can calculate the bulge-to-total flux ratio as another quantity to classify galaxy morphology.

2.5 Summary

In this study, I use the code GALFIT to complete parametric morphology measurements of selected galaxy samples. The technique requires accurate background estimation completed using a flux-growth method. Precise measurements of the background have been found to be vital in properly fitting the galaxy surface brightness. Additionally, the use of either a mask to remove other sources or fit them simultaneously is, and the creation optimally sized postage stamps for surface brightness analysis are important in ensuring only the light of the target galaxy is taken into account during the modeling. Finally determination of goodness of fit using χ^2 and checking error estimates is used throughout this work to ensure accurate morphological analysis.

Chapter 3

Comparison of Parametric and Non-Parametric Morphology Measurements

3.1 Introduction

Parametric measurements of galaxy morphology provide insight into the overall surface brightness profile of a galaxy. Non-parametric techniques also determine the galaxy type, but some methods are better suited for finding irregularities in the light distributions of galaxies. While most studies choose either a parametric or non-parametric approach to their morphological study, it is of interest to combine different methods to further understand the nature of the galaxy sample. The Gini coefficient is a statistic taken from economics that has been applied to astronomical images to rank pixel values, while the second-order moment of the brightest regions of a galaxy, M_{20}, traces the light concentration within an image (Lotz et al., 2004; Peth et al., 2015). The combination of information provided by these two non-parametric approaches can be used to indicate if a galaxy is bulge-dominated, disk-dominated, or a merging or irregular system. GALFIT provides a method of parametrically measuring galaxy morphology by modeling the surface brightness distribution using a Sérsic function. Multiple functions can

also be applied enabling the use to separate the bulge and disk component of the galaxy. The morphology can be determined using the Sérsic index, n, due to high n values correponding to steep inner profiles, like elliptical galaxies, and low n values corresponding to smoother light distributions , like disk galaxies. When combined with the overall bulge-to-total flux ratio of the galaxy, these classifications can be further divided into their Hubble Types (Hubble, 1926).

In this section, I take parametric morphology measurements of a galaxy sample, and compare these results with the non-parametric Gini coefficient and M_{20} measurements. First I will describe the data used in this study, and explain how I choose the galaxy sample. Next, I will show how galaxy Sérsic index and bulge-to-total flux ratios compare to these measurements individually and combined, and, finally, I will summarize my findings.

3.1.1 Data and Sample Selection

Cosmic Assembly Near-Infrared Deep Extragalactic Legacy Survey: CANDELS

CANDELS is a high-resolution, extra-galactic survey that covers approximately 800 arcmin^2, and consists of two different surveys. The deep survey covers ∼125 arcmin^2 within the Great Observatories Origins Deep Survey (GOODS)-N and GOODS-S (Giavalisco et al., 2004), and the wide survey covers the GOODS fields as well as the Extended Groth Strip (EGS, Davis et al. 2007), a sub-area of the Cosmological Evolution Survey (COSMOS, Scoville et al. 2007), and Ultra-deep Survey (UDS, Lawrence et al. 2007; Cirasuolo et al. 2007). The Wide survey images to $\sim$ 2 orbit depth with the Hubble Space Telescope (HST) Wide-Field Cameral 3 (WFC3) in the infrared (IR) with parallel optical Advanced Camera For Surveys (ACS) observations. The Deep Survey images to ∼12 orbit depth in the two fields. I summarize the depth and filters used in this work for the survey in Table 3.1. The survey is designed to document the first third of galactic evolution from $z = 8$ to 1.5, and additional details about the survey can be found in Grogin et al. (2011) and Koekemoer et al. (2011). The high-resolution imaging from the survey combined with other ancillary data, makes CANDELS ideal for detailed morphological studies.

Table 3.1: Details of the CANDELS survey

		Wide Survey	Deep Survey[a]	
Instrument/Camera	Filter	Limiting Magnitude[b] (5σ)	Limiting Magnitude[b] (5σ)	Zeropoint
		GOODS-North Field		
ACS/WFC	F435W	27.7	27.7	25.67
ACS/WFC	F606W	28.0	28.2	26.47
ACS/WFC	F775W	27.5	28.0	25.65
ACS/WFC	F850LP	27.5	27.6	24.86
WFC3/IR	F105W	27.1	28.2	26.27
WFC3/IR	F125W	27.1	28.0	26.25
WFC3/IR	F160W	27.0	27.8	25.96
		GOODS-South Field		
ACS/WFC	F435W	27.8	27.7	25.67
ACS/WFC	F606W	28.0	28.3	26.51
ACS/WFC	F775W	27.5	27.6	25.68
ACS/WFC	F850LP	27.3	27.6	24.88
WFC3/IR	F125W	27.5	27.9	26.25
WFC3/IR	F160W	27.3	27.6	25.96
		UDS		
ACS/WFC	F606W	27.2	-	26.49
ACS/WFC	F814W	27.2	-	25.94
WFC3/IR	F125W	27.1	-	26.25
WFC3/IR	F160W	26.9	-	25.96
		EGS		
ACS/WFC	F606W	28.0	-	26.49
ACS/WFC	F814W	27.9	-	25.94
WFC3/IR	F125W	27.1	-	26.25
WFC3/IR	F160W	27.0	-	25.96
		COSMOS		
ACS/WFC	F606W	27.2	-	26.49
ACS/WFC	F814W	27.2	-	25.94
WFC3/IR	F125W	27.1	-	26.25
WFC3/IR	F160W	26.9	-	25.96

[a] Only available in GOODS-N and GOODS-S fields.
[b] All magnitudes are in AB. Limits correspond to 5× the photometric error within a 0.2 arcsec^2 aperture.

The MOSFIRE Deep Evolution Field (MOSDEF) Survey

The MOSDEF survey is a large multi-year survey with the MOSFIRE multi-object spectrometer on the Keck I telescope (McLean et al., 2012). The aim of the survey is to obtain rest-frame optical spectra of $\sim$ 1500 H-selected galaxies to study their stellar, gaseous, metal, dust, and black hole content. The MOSDEF observations are conducted in three main fields (AEGIS, COSMOS, GOODS-N), and due to the range of field visibility two additional CANDELS fields, GOODS-S and UDS, were observed in the December 2012 pilot run. The survey targets three redshift bins: $1.37 \leq z \leq 1.70$, $2.09 \leq z \leq 2.61$, and $2.95 \leq z \leq 3.80$. Targets for spectroscopy are prioritized by their H-band magnitude and the availability of spectroscopic, grism, and photometric redshifts, down to $H = 24.0$, 24.5, and 25.0 magnitude, for each redshift bin respectively. Details of the survey strategy, observations, data reduction, and characteristics of the full galaxy sample are described in Kriek et al. (2015). Galaxy morphology is analyzed for objects observed through the first two seasons of the survey, and the combination of high-resolution image analysis of galaxy morphology and detailed galaxy spectral properties enables a much more in depth study of galaxy evolution.

Sample Selection

The Gini-M_{20} sample used in this study was derived from catalogs produced by the CANDELS team (Grogin et al., 2011; Koekemoer et al., 2011) similar to Peth et al. (2015). In this study, they use CANDELS *H*-band selected multi-wavelength catalogs for UDS, COSMOS, GOODS-S, and EGS (Galametz et al., 2013; Guo et al., 2013; Nayyeri, prep), and photometric redshift catalogs (Dahlen et al., 2013). They also obtain stellar mass estimate, SED and rest-frame photometry catalogs using FAST (Kriek et al., 2009). From these catalogs, the non-parametric morphologies described in Chapter 1 are determined. From these morphology catalogs, I select galaxies in the range of $1.0 \leq z \leq 3.0$, similar to the lower redshift bins of the MOSDEF survey. Morphology measurements are compared at rest-frame *B*-band optical wavelengths, so *J*-band non-parametric measurements were taken for galaxies with $z \leq 1.70$ and *H*-band for $z > 1.70$. Any galaxies flagged for unreliable fits were excluded.

This sample was then matched to galaxies from the MOSDEF parent sample described above and further discussed in Chapter 5 in two of the main fields, COSMOS and AEGIS, as well as the two additional fields targeted in the pilot run due to field visibility, GOODS-S and UDS. Single Sérisic modeling and bulge-disk-decompositions were applied to the galaxy sample, and only those with reliable fits are used in this study. After combining the two samples, this results in a sample of 2251 galaxies in the redshift range $1.0 \leq z \leq 3.0$ with reliable, rest-frame B-band measurements of galaxy Sérsic index, B/T, Gini coefficient, and M_{20}.

3.2 Comparison with Gini-M_{20}

Parametric morphology is well studied using various codes, and has become one of the dominant morphological techniques due to the availability of high resolution multi-waveband galaxy surveys. It is important to keep in mind how these measurements compare to other techniques, including non-parametric morphology measurements. While the various non-parametric measurements are important for different types of galaxies, the Gini-M_{20} relation from Lotz et al. (2004) has been found to separate normal galaxies, consisting of early- and late-type galaxies, and mergers by applying dividing lines on the relation. We show the overall Gini-M_{20} diagram for the sample in Figure 3.1.

I compare the morphological properties determined from GALFIT in Figures 3.2 and 3.3. I first show the dependence on the galaxy Sérsic index n in Figure 3.2, which shows agreement with the dividing lines that separate out different galaxy types. Galaxies with $n \geq 2.5$ have been found to be early-type elliptical galaxies, which on the Gini-M_{20} diagram are found in the right panel. I find a large group of these galaxies in that section, as well as a little scatter in the disk-dominated section of the diagram, and some merging or irregular systems, as indicated by the upper panel. For the parametric morphology disk galaxies, they are more plentiful in the sample, and dominate the lower right section of the Gini-M_{20} diagram, which is where late-type galaxies are expected (Peth et al., 2015; Lotz et al., 2004). The other parametric morphology parameter that I compare with the Gini-M_{20} non-parametric morphology, is the galaxy B/T,

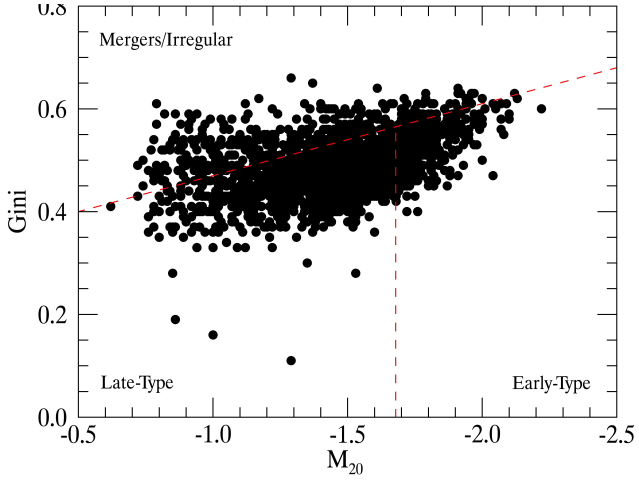

Figure 3.1: Rest-frame optical Gini-M_{20} Diagram for galaxies from the MOSDEF survey parent sample in four CANDELS fields, COSMOS, GOODS-S, UDS, and AEGIS. The dividing lines are from Peth et al. (2015) and are the modified dividing lines from Lotz et al. (2004) that separate different galaxy population. Mergers typically occupy the upper left, early-type, bulge-dominated galaxies on the right, and disk-dominated, late-type spirals are typically found in the bottom, left wedge of the diagram.

which is shown in Figure 3.3. I observe no correlation in the diagram with the measured B/T of the galaxies, but when combining the two parametric morphologies, n and B/T, a better understanding of the galaxy morphology can be achieved.

I combine the two parametric morphologies to separate out early-type elliptical galaxies, early-type spiral, and late-type spiral galaxies, shown in Figure 3.4. The general separation of galaxies into elliptical and disk galaxies using $n \geq 2.5$ and $n < 2.5$, respectively, does not take into account irregular type galaxies or mergers. In order to further investigate this, different ranges of the galaxy n are compared. In Figure 3.4 the top row consists of galaxies with $n \geq 2.5$ ($B/T \geq 0.5$ on the left, $B/T < 0.5$ on the right), and we separate this sample into galaxies with $n > 6.0$ shown in black, and galaxies with $2.5 \leq n \leq 6.0$ in green. Galaxies in the range of $2.5 \leq n \leq 6.0$ and $B/T \geq 0.5$ are more commonly elliptical galaxies, which would be expected to occupy only the right panel of the Gini-M_{20} diagram, however while I do find the majority of the galaxies in that section, there is still a large scatter into the merger/irregular section of the diagram. Galaxies with $n > 6.0$ could be compact galaxies or galaxies with very bright

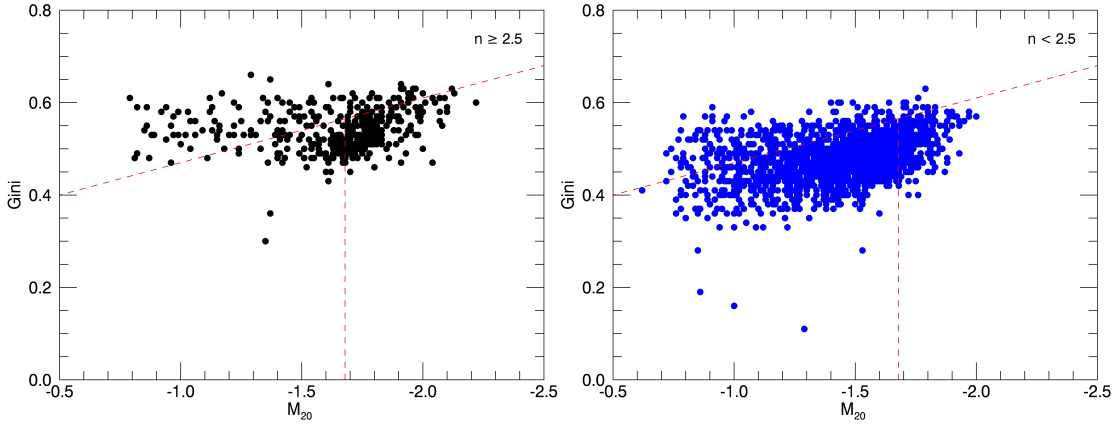

Figure 3.2: Rest-frame optical Gini-M_{20} Diagram for galaxies from the MOSDEF survey parent sample in four CANDELS fields, COSMOS, GOODS-S, UDS, and AEGIS including the galaxy Sérsic index as measured using GALFIT. The dividing lines are the same as Figure 3.1. On the left we show galaxies with $n \geq 2.5$, which is typically indicative of early-type, elliptical galaxies, while galaxies with $n < 2.5$, disk galaxies, are shown on the right.

central components that dominate the galaxy, or galaxies with very high Sérsic indices can also be misclassifed. I would still expect these galaxies to fall in the bulge-dominated section of the Gini-M_{20} diagram. Very few galaxies with this range of Sérsic index were found but with a large scatter, making it hard to understand the significance. Galaxies with a high n and low B/T are most commonly low surface brightness or compact objects, which should still lie in either the bulge-dominated or irregular section of the Gini-M_{20} diagram. I find very few of these objects in the disk-dominated, lower section of the diagram, showing morphological agreement between the two techniques.

In the lower plots of Figure 3.4, I investigate agreement between disk-like morphological classifications from parametric morphology compared to the Gini-M_{20} diagram. There is an overall agreement between these classifications showing that the majority of galaxies with $n <$ 2.5 lie in the lower section of the diagram. There is a little scatter into the merger/irregular section of the diagram and early-type galaxies, but overall the majority of the galaxies land in the lower left section. In previous studies, galaxies with $n < 0.8$ have been found to be merging or irregular systems instead of classic disk galaxies (Ravindranath et al., 2006). We separate these galaxies, shown in green, to see if they lie in the merger/irregular section of the Gini-M_{20}

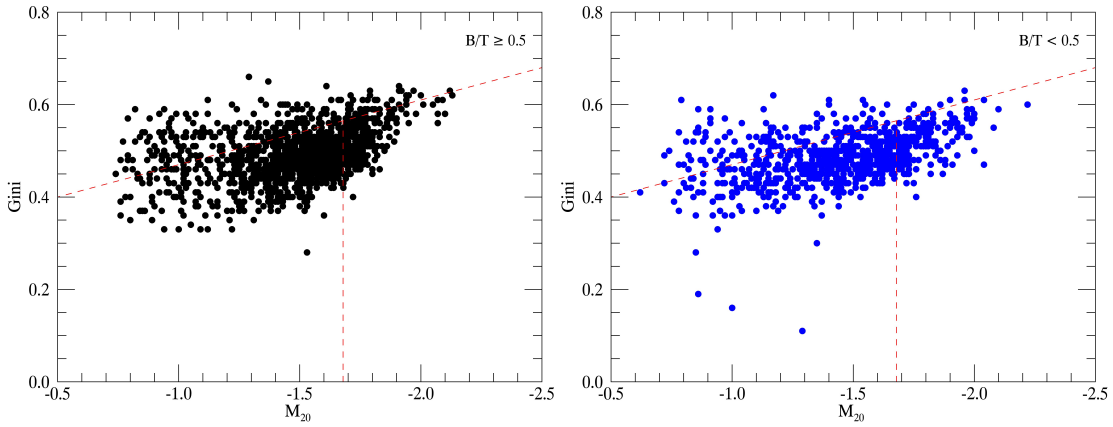

Figure 3.3: Rest-frame optical Gini-M_{20} Diagram for galaxies from the MOSDEF survey parent sample in four CANDELS fields, COSMOS, GOODS-S, UDS, and AEGIS including the B/T measured using GALFIT. The dividing lines are the same as Figure 3.1 and 3.2. On the left we show galaxies with $B/T \geq 0.5$, which are bulge-dominated galaxies, while galaxies with $B/T < 0.5$, disk-dominated galaxies, are shown on the right.

diagram, or remain in the disk-dominated classification. We find that, these galaxies are almost completely contained in the disk-dominated section of the diagram indicating that these are perhaps not merging systems. Some of the disk galaxies do lie in the early-type section of the diagram, and more of them with high B/T than with low B/T. These would be early-type disk galaxies that have larger bulge fractions possibly evolving into quiescence.

3.3 Summary and Conclusion

Overall, I find agreement between the parametric and non-parametric morphology measurements of the CANDELS galaxies. The best agreement is between galaxy Sérsic index and the Gini-M_{20} diagram. I find no correlation between the B/T of the galaxy sample with Gini-M_{20} by itself, but by combining the information obtained through the galaxy Sérsic index and the B/T I find better agreement between the two different morphology approaches. Due to the agreement found between the parametric and non-parametric morphology measurements, I find that using parametric Galfit measurements of the galaxy n and B/T in combination is sufficient in quantifying and classifying the galaxy type for the study of morphology.

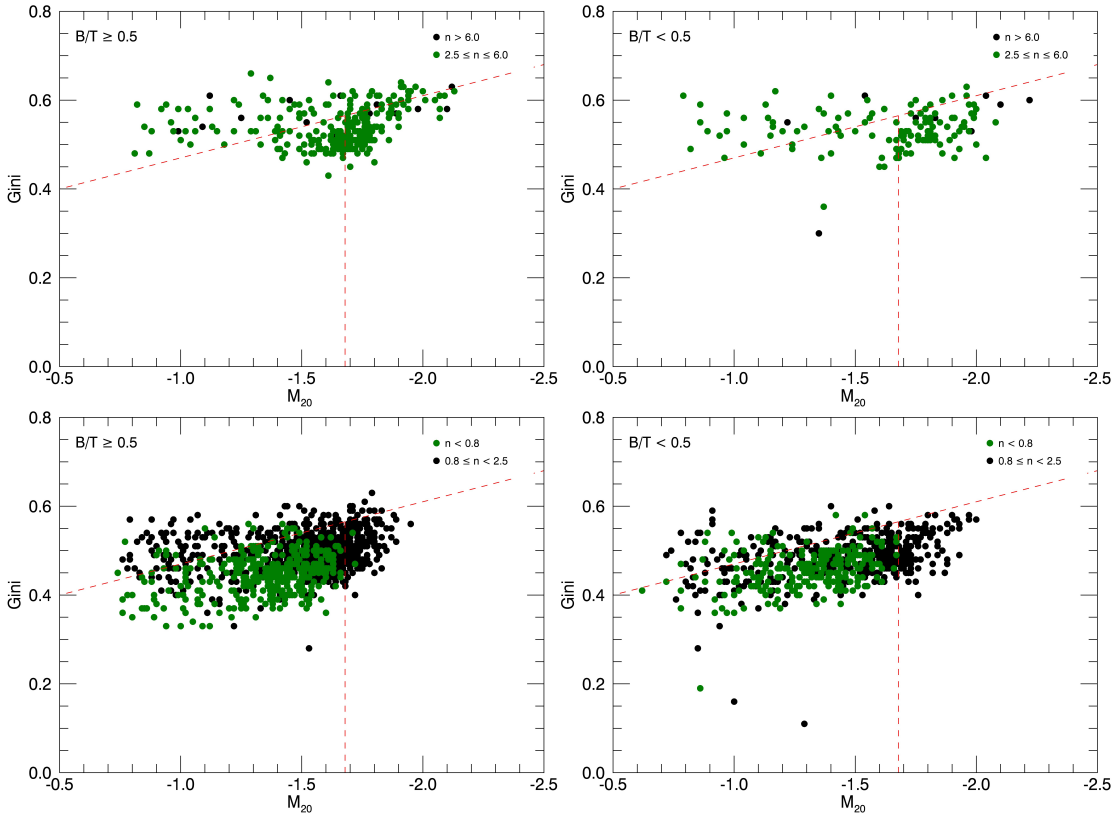

Figure 3.4: Rest-frame optical Gini-M_{20} Diagram for galaxies from the MOSDEF survey parent sample in four CANDELS fields, COSMOS, GOODS-S, UDS, and AEGIS including the galaxy Sérsic index and B/T as measured using GALFIT. The dividing lines are the same as described in Figures 3.1, 3.2 and 3.3. On the left we show galaxies with $B/T \geq 0.5$, which is typically indicative of bulge-domainted galaxies, while galaxies with $B/T < 0.5$, disk galaxies, are shown on the right. The top and bottom plots in the figure show galaxies with Sérsic index $n \geq 2.5$ and $n < 2.5$, respectively.

Chapter 4

Rest-frame Optical Morphologies of Galaxies Selected at Mid-Infrared (24 μm) Wavelength

4.1 Introduction

Far-infrared luminosity of galaxies at 24 μm provides a reliable and independent diagnostic for star formation activity in galaxies, as well as nuclear activity. It measures the contribution from HII regions in galaxies suggesting that this emission is primarily produced by young, ionizing stars within galaxies (Zhu et al., 2008; Calzetti et al., 2005, 2007; Dale et al., 2005). This enables us to observe dust emission from young stellar populations because it avoids most of the vibrational emission from the polycyclic aromatic hydrocarbons (PAH) and instead samples the continuum emission of very small dust grains (Wu et al. 2005). Therefore, galaxies with significant emission in 24 μm band are mostly dominated by disk-like, star-forming systems. However, the mid-infrared (MIR) continuum can also easily be contaminated from dust heated by active galactic nuclei (Wu et al. 2005), so as we observe morphological trends with redshift, we can observe the role of starbursts as well active galactic nuclei (AGNs) in the 24 μm band.

Due to the star forming nature and nuclear activity associated with 24 μm emission, observ-

ing galaxies with passive, elliptical morphologies and 24 μm detection provide a curious sample of galaxies. By studying the nature of these galaxies, it is possible to gain a better understanding of evolution scenarios of galaxies as they transition from star-forming systems to quiescence as well as nuclear properties of centrally concentrated systems.

In the present chapter, we use 2-D decomposition of deep multi-wavelength HST ACS images to obtain morphologies of $\backsim$ 470 galaxies with 24 μm detection in the GOODS southern field. We have determined morphology using single Sérsic function fits to the galaxy surface brightness as well as two-component, bulge-disk decompositions of the galaxy sample. In this chapter, we compare the morphological classification from each of these fits of MIPS sources as well as how these properties change as a function of redshift. By studying 24 μm sources in the redshift range of $0.25 \leq z \leq 1.25$, I am able to obtain rest-frame optical morphologies of galaxies observed in the Hubble Space Telescope (HST) Advanced Camera for Surveys (ACS) optical bands. Furthermore, I study the nature of elliptical galaxies that show 24 μm emission. The chapter is organized as follows: in §2 we summarize the data sets and catalogs used to construct the 24 μm sample and control sample of galaxies analyzed in the present study, and we discuss the selection of the 24 μm and control galaxy samples in §3. In §4 we discuss the morphological analysis, and in §5 we discuss possible biases and selection effects in our sample. Our results are discussed in §6 and conclusions summarized in §7. Throughout we quote all magnitudes in AB magnitudes (Oke and Gunn, 1983). We also adopt a flat ΛCDM cosmology of $\Omega_m = 0.3$, $\Omega_\Lambda = 0.7$, and use the Hubble constant in terms of $h \equiv H_0/100$ km s^{-1} Mpc$^{-1} = 0.70$.

4.2 Sample Selection

In this study, we aim to measure rest-frame optical morphologies of galaxies, which enables us to take into account a morphological *k*-correction allowing us to compare the morphologies at the same wavelength. This requires both multi-wavelength imaging and a reliable redshift estimation, which is available through the CANDELS (Grogin et al., 2011; Koekemoer et al., 2011). Our multi-wavelength data set focuses on the CANDELS/GOODS-S field, which has been

imaged with the HST ACS instrument in four passbands, F435W, F606W, F775W, and F850LP, hereafter referred to as *B, V, i*, and *z* band respectively, as part of the GOODS *Hubble* Treasury Program (PI: M. Giavalisco). The GOODS multiwavelength, deep survey covers $\backsim$ 320 arcmin^2 in two fields, the Chandra Deep Field-South (CDF-S) and the Hubble Deep Field-North (HDF-N). The *HST/ACS* images used in our analysis are version v3.0 of the mosaiced, drizzled images of the GOODS HST/ACS Treasury program (Giavalisco et al., 2004), which cover the CANDELS GOODS-S $10'x16'$ *HST/WFC3* IR region resulting in a final plate scale of 0.06 arcsec pixel^{-1} (Grogin et al., 2011; Koekemoer et al., 2011). The GOODS-S field also has infrared imaging using HST WFC3 through CANDELS in the *H* and *J* filters.

Redshifts of the sample are from the CANDELS GOODS-S photometric redshift catalog (Dahlen et al., 2013), which incorporates spectroscopic redshifts when available. This catalog was produced by combining photometric redshift (photo-z) estimations of 11 different photometric redshift codes. The photometry used ranges from U-band through mid-infrared filters, and was derived using the template-fitting method (TFIT) method. This measures galaxy photometry from prior high resolution imaging. This is done by using the position and two-dimensional surface brightness profiles from these high resolution images to measure the fluxes at lower resolution and other passbands (Laidler et al., 2007; Dahlen et al., 2010). This method reduces uncertainties in photometric measurements of objects by maximizing signal to noise, improving deblending of objects, and providing a better estimate of the flux of an object. Results from the TFIT measurements were used to test the photometric redshifts (photo-z), and then determine the best photo-z estimate for each galaxy in the catalog. The primary test catalog used for the study includes the *HST/WFC3 H*-band selected TFIT multi-band photometry. A detailed description of the CANDELS GOODS-S TFIT catalog is given in Guo et al. (2013), and the methodology to derive the photometry is described in Galametz et al. (2013). The available spectroscopic redshifts are compiled from a set of publicly available data, which was used to evaluate the accuracy of the photometric redshifts (see Dahlen et al. 2013 for more details).

Galaxies with 24 μm emission are drawn from the MIPS 24 μm catalog, which uses data from the Multiband Imaging Photometer for Spitzer (MIPS) through the GOODS Spitzer Legacy

Program (Magnelli et al., 2011; Dickinson et al., 2003). This catalog enabled us to limit the sample of galaxies in the GOODS-S field to only those galaxies with MIPS 24 μm flux detection. Through Monte Carlo simulations, Magnelli et al. 2011 estimated that the 24 μm observations reach an 80% completeness limit at 30 μJy, so in matching we only consider those with MIPS 24 μm flux greater than 30 μJy, reducing chance of spurious detections and increasing accuracy of the sample (please see Magnelli et al. 2011 for further information about the MIPS catalog).

The main aim of this chapter is to explore the rest-frame optical morphological properties of a complete sample of MIPS 24 μm selected galaxies in the redshift range $0.25 \lesssim z \lesssim 1.25$. In order to achieve this, we use a MIPS 24 μm detected sample and compare the measured morphologies to a control sample selected to be undetected at MIPS 24 μm band. Color images of disk-dominated and bulge-dominated galaxies at different redshift intervals selected from our MIPS sample are presented in Figure 4.1.

Figure 4.1: Color images of MIPS 24 μm galaxies at different redshift intervals. Left to right are images of galaxies in the redshift intervals: $0.25 \leq < 0.5$, $0.5 \leq z < 0.75$, $0.75 \leq z < 1.0$, and $1.0 \leq z \leq 1.25$, while the top and bottom rows consist of disk-dominated and bulge-dominated galaxies, respectively, as classified by both morphological classifications.

For this study, we use the following criteria to select our MIPS sample:

- Use CANDELS GOODS-S photometric redshift catalog

- Select sources with MIPS 24 μm detection
- Limit the sample to the sources in the range $0.25 \lesssim z \lesssim 1.25$ to obtain rest-frame optical morphology measurements using HST ACS images.
- Restrict the absolute magnitude range to $-18 < M_B < -21$ to allow selection from the same part of the luminosity function at different redshift and hence, reducing the bias as a function of redshift

Beginning with the CANDELS GOODS-S photometric redshift catalogs these sources are then matched to the MIPS 24 μm catalog, using a 1.5" matching radius (i.e. FWHM of the IRAC 3.6 μm observations). This final sample of MIPS 24 μm sources is then limited to only those with photometric redshifts (although spectroscopic redshifts were used when available) in the range $0.25 \lesssim z \lesssim 1.25$.

To carefully analyze and study the significance of MIPS detection, we need a control sample, selected in exactly the same way as the main sample but without MIPS detection. We used the same process as described above starting with the CANDELS GOODS-S photometric redshift catalog and selected galaxies within the CANDELS WFC3 F160W field without any MIPS detection. In order for this sample to be truly representative, we then limited the sample to only those with photometric redshifts (or spectroscopic when available) in the range of $0.25 \lesssim z \lesssim 1.25$.

Ideally, when comparing the morphologies of MIPS 24 μm selected galaxies and the control sample, one needs a complete and unbiased sample. This is needed to study the evolution of galaxies with redshift. Moreover, the selection must be the same for both the MIPS and control samples. As discussed in Casey et al. 2014, MIPS 24 μm flux density decreases drastically with redshift, so a possible bias could be caused by electing MIPS 24 μm detected galaxies out to redshift $z \sim 1.25$ (see Figure 3 in Casey et al. 2014). We limited the rest frame absolute magnitude between $-21 < M_B < -18$ to reduce this bias, as shown in Figure 4.2. We applied these magnitude limits to both the MIPS 24 μm detected and control galaxy samples, respectively, in order to compare the same part of the luminosity function reducing the possibility of false trends in morphology. This selection reduced the original MIPS detected sample of 737 galaxies

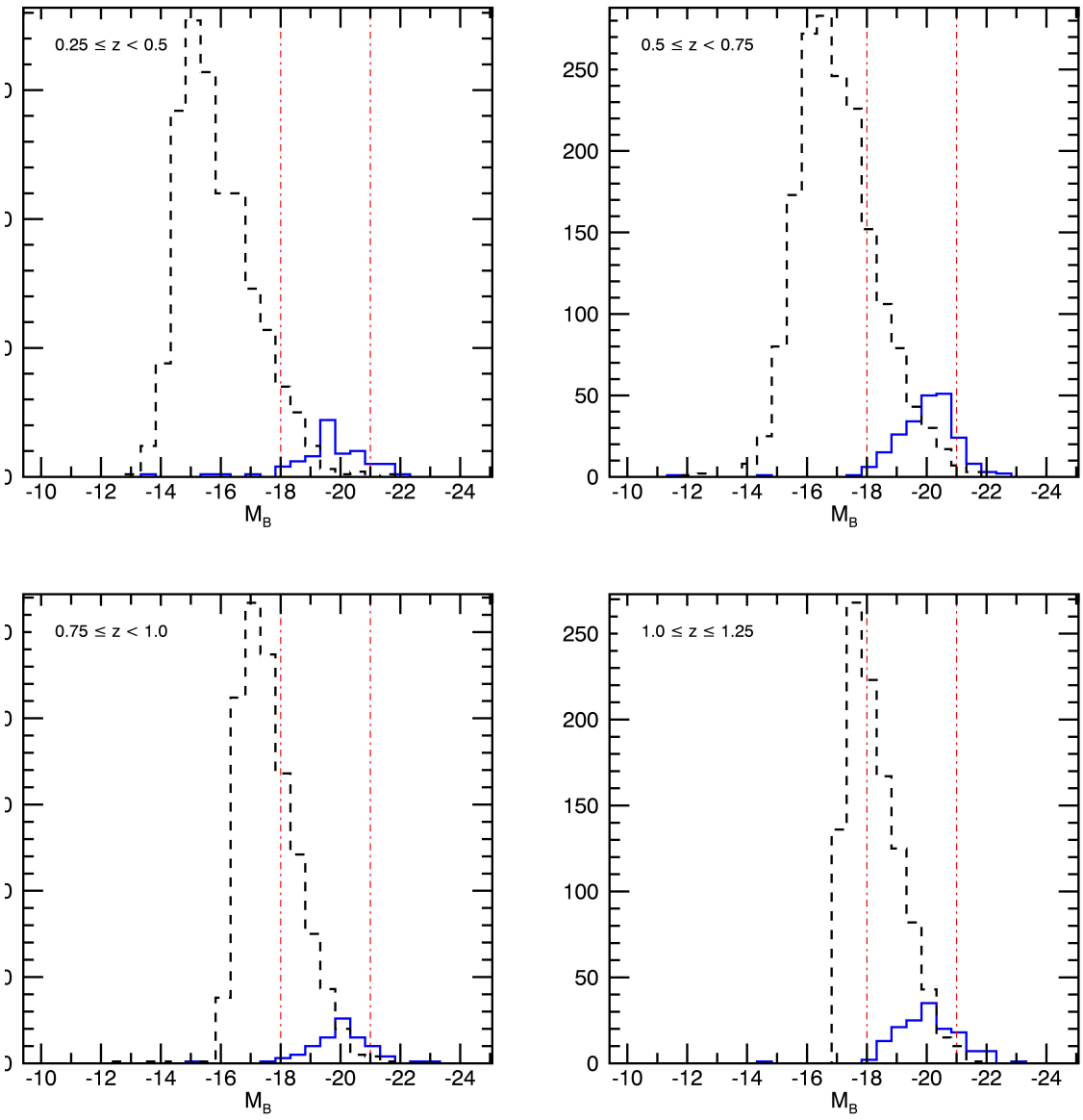

Figure 4.2: Rest-frame absolute magnitude distribution of original MIPS 24 μm sample (solid line) and the control sample (dashed line). The dotted lines indicate the limits imposed on the absolute magnitude so that the same section of the luminosity function is analyzed.

spanning a wide range of absolute magnitudes, down to the sample of 470 galaxies. This also had a major affect on the control sample taking it from 5179 galaxies to the sample of 1109 in the selected absolute magnitude range. The control sample tends to be a much brighter sample with absolute magnitudes peaking between -15 M_B and -18 M_B, shown in Figure 4.2, and by

selecting those in the same range as the MIPS detected sample we are able to compare similar samples.

4.3 Morphological Analysis

We measure the morphology of the MIPS 24 μm galaxies by modeling the two-dimensional surface brightness distribution with a Sérsic function (de Vaucouleurs, 1948; Sersic, 1968). This is done using the GALFIT software (Peng et al., 2002, 2010), which convolves the 2D analytical model with the PSF using the Levenberg-Marquardt algorithm for χ^2 minimization giving the optimum fit. In order to consistently compare galaxy properties at different redshifts, we measure their Sersic parameters at the same rest-frame wavelength. To allow such measurements over our selected redshift range, in a wavelength as close as possible to optical, we use multi-wavelength ACS images to measure the rest-frame optical B-band (4297 Å) morphologies of both galaxy samples.

Galfit is designed to fit one galaxy at a time, and requires individual postage stamps for each of our MIPS galaxies. Postage stamp sizes were determined using the same technique as using in the IDL program GALAPAGOS (Galaxy Analysis over Large Areas: Parameters Assessment by GALFITting Objects from SExtractor, see Barden et al. 2012 for further details about GALAPAGOS). Masks were created using SExtractor (Bertin and Arnouts, 1996) parameters to determine elliptical profiles. Ellipses that overlapped the target galaxy were then removed from the mask, and a simultaneous Single Sérsic fit was performed on any additional galaxies.

The input parameters for GALFIT for each galaxy include position, total magnitude, effective radius or scale length, Sérsic index, ellipticity, position angle, and the sky background at the center of the fitting region, were taken from SExtractor catalogs. These catalogs were produced by the CANDELS team, which are selected based on the *H*-band SExtractor catalog for all GOODS-S ACS observed bands (F435W, F606W, F775W, and F850LP). We use a fixed sky value that we obtain through the flux growth method, which calculates the average flux in elliptical annuli centered around the object of interest, while excluding flux from neighboring

sources (Barden et al., 2012). Galfit also convolves the modeled galaxy Sérsic function with a point-spread function (PSF). The PSFs used for the convolution were generated by the CANDELS team using stacked stars, which have FWHM of $\sim 0.''08, 0.''08, 0.''08$, and $0.''09$ for *B, V, i*, and z bands, respectively.

For the single Sésic function fit to the galaxy sample, the output parameters include total magnitude, effective radius, r_e, the Sérsic index, n, ellipticity, and position angle. The Sérsic index, a measure of the concentration of the light profile, were constrained between the values of 0.2 and 8.0 in order to avoid arbitrarily large values caused by active galactic nuclei (AGN) or compact, central point sources due to the steep inner profile(Ravindranath et al., 2006). We reject $\backsim$ 20% of the MIPS 24 μm galaxies due to large χ^2 errors, those with large r_e errors relative to the effective radius, and objects that have been flagged for unreliable measurements. These are rejected if if the fits indicate $\chi^2 > 5.0$ and if $\frac{r_e error}{r_e} > 0.2$. After visual examination, we find that most of the rejected galaxies are double nuclei, low surface brightness, or extended objects. We also select galaxies with $b/a > 0.3$, since morphology of high inclination galaxies is not a reliable measurement. After removing these galaxies from our sample, we find that 274 out of the 470 (58%) MIPS 24 μm detected galaxies and 605 of the 1109 (55%) control galaxies have low inclination and reliable single component, Sésic function fits.

In addition to the overall Sésic function fit with GALFIT, morphological classifications were also completed using a two-component GALFIT of the bulge and disk components simultaneously. For the bulge component, we fit a Sérsic function, where the Sésic index, n, is a free parameter ranging between 0.2 and 8.0. The disk component of the bulge-to-disk decomposition is fit using an exponential disk, where the Sésic index is fixed to $n = 1$. All other parameters (total magnitude, r_e or r_s, axis ratio, and position angle) are allowed to vary independently. The input parameters are determined in the same manner as for a single-component fit, however we initially input a ratio of $r_e, bulge/r_e, disk = 0.4$, which enabled us to determine an initial input scale length from the disk using the relation $r_e = 1.678 r_s$ (Peng et al., 2010). A two-component fit adds additional free parameters resulting in larger errors, but after removing objects flagged for unreliable measurements as well as those with $b/a < 0.3$ to eliminate galaxies that nearly

edge-on disk galaxies (Oohama et al., 2009), we find that 132 of the 470 (28%) MIPS 24 μm galaxies and 292 out of the 1109 (26%) control galaxies meet this criteria. We compose our final sample of low inclination galaxies to be just those with reliable single component Sérsic fits and reliable two-component bulge-disk decompositions, resulting in final samples of 100 MIPS 24 μm and 226 control galaxies.

4.4 Results

We adopt a simple morphological classification based on the Sérsic index, n, and bulge-to-total flux ratio, B/T. Previous literature indicates that galaxies with higher Sérsic indices ($n \geq 2.5$) represent more quiescent, bulge-dominated galaxies, while lower values of n are typical of disk-dominated galaxies (Ravindranath et al., 2006; Lang et al., 2014; Bruce et al., 2012). We also classify bulge-dominated and disk-dominated galaxies by bulge-to-total ratio using a cut-off of $B/T \sim 0.5$. Ravindranath et al. (2006) also distinguish a third class of irregular galaxies, which have a Sérsic index of $n < 0.8$, but for now we will classify the morphology as either bulge-dominated or disk-dominated only.

4.4.1 Disk- and Bulge-Dominated Galaxies

Since MIPS 24 μm emission is primarily due to dust emission of absorbed light from young stars, iit provides an independent measure of star formation in galaxies. We therefore expect the MIPS sample to be dominated by star forming, disk-like galaxies, while we expect the control sample, which has no MIPS 24 μm detection, to have a higher population of elliptical galaxies. However, if we find MIPS detected galaxies with elliptical morphologies, this 24 μm emission could be due to the presence of AGN. With this in mind, we first compare the MIPS galaxy morphologies with the morphologies of the control sample of galaxies. In Figure 4.3 we show the distribution of rest-frame B-band Sérsic parameters measured from 2-D modeling of the images and the two-component B/T of the MIPS detected and the control samples respectively. We observe a disk-dominated MIPS population from both Sérsic index and B/T classifications,

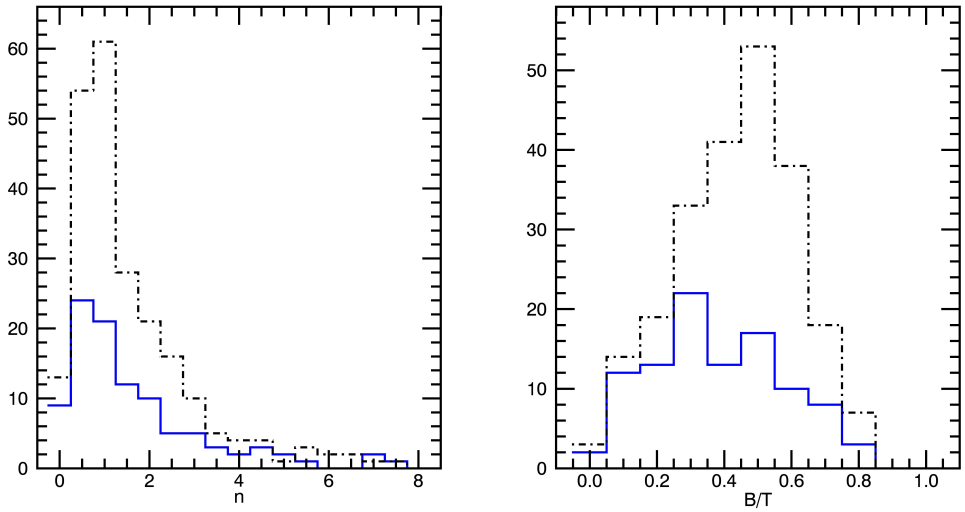

Figure 4.3: Rest-frame optical morphology distributions for the MIPS 24 μm sample (blue, solid line) and control sample (black, dashed line). On the left we show the Sérsic Index distribution, while on the right we show the bulge-to-total flux ratio of the samples. Bulge-dominated galaxies are considered to be those with $n \geq 2.5$ and $B/T \geq 0.5$, while disk-dominated galaxies have $n < 2.5$ and $B/T < 0.5$

where $\backsim$ 76% of the MIPS 24 μm sample have disk-dominated Sérsic indices and $\backsim$ 62% have $B/T < 0.5$. This is consistent with the majority of MIPS detected galaxies being disk-dominated galaxies indicating that star-formation is the source of the 24 μm emission in these galaxies. The control sample is also dominated by disk galaxies with $\backsim$ 78.3% and $\backsim$ 48.7% having disk-like morphologies by Sérsic Index and B/T, respectively, but this is also consistent with findings of galaxy type dependence luminosity functions. In order to further investigate the fraction of bulge-dominated and disk-dominated galaxies classified by each technique, we further analyze the galaxy morphologies at different redshift intervals.

We observe that through all redshifts, both the control sample and MIPS 24 μm sample are disk-dominated by Sérsic index, similar to that of the overall distributions of the galaxies. The B/T indicates that the MIPS 24 μm sample is disk-dominated over the redshift ranges of $0.25 \leq z < 0.5$, $0.5 \leq z < 0.75$, and $1.0 \leq z < 1.25$. However, we find that the MIPS 24 μm sample is bulge-dominated in the redshift range of $0.75 < z < 1.0$, which may be due to the small sample size of only 16 MIPS 24 μm detected galaxies in this redshift range. The control sample instead

Table 4.1: Percentages of galaxies classified as bulge-dominated or disk-dominated by both Sérsic Index and B/T flux ratio for the (a) MIPS 24 μm and (b) control sample galaxies.

MIPS 24 μm Sample					
		n		B/T	
Redshift	N_{gal}	Bulge-dominated	Disk-dominated	Bulge-dominated	Disk-dominated
$0.25 \leq z < 0.50$	9	11.1%	88.9%	33.3%	66.7%
$0.50 \leq z < 0.75$	41	39.0%	61.0%	39.0%	61.0%
$0.75 \leq z < 1.00$	16	0.0%	100.0%	56.2%	43.8%
$1.00 \leq z \leq 1.25$	34	20.6%	79.4%	29.4%	70.6%
All	100	24.0%	76.0%	38.0%	62.0%
Control Sample					
		n		B/T	
Redshift	N_{gal}	Bulge-dominated	Disk-dominated	Bulge-dominated	Disk-dominated
$0.25 \leq z < 0.50$	20	25.0%	75.0%	25.0%	75.0%
$0.50 \leq z < 0.75$	56	17.9%	82.1%	42.9%	57.1%
$0.75 \leq z < 1.00$	43	18.6%	81.4%	53.5%	46.5%
$1.00 \leq z \leq 1.25$	107	24.3%	75.7%	59.8%	40.2%
All	226	21.7%	78.3%	51.3%	48.7%

follows a trend of increasing bulge fraction with redshift. This could be explained due to disks not being formed by $z \sim 1$, and indicative of the epoch of bulge formation.

In order to compare these fractions in Figure 4.4 as a function of redshift. We bin the data into four redshifts bins, $0.25 \leq z < 0.5$, $0.5 < z < 0.75$, $0.75 < z < 1.0$, and $1.0 < z \leq 1.25$. The results of this binning are shown in Table 4.1. After examining the Sérsic indices and B/T ratios for the two galaxy samples, we also compared the values for each galaxy in the sample. In Figure 4.5, we show B/T vs. n for each galaxy in the MIPS 24 μm and the control samples. Overall, we observe a large scatter in the B/T for galaxies with $n < 2.5$, indicative of disk galaxies not following classic DeVaucouleur bulge profiles. We also show the average B/T with n in blue for the MIPS 24 μm sample and in black for the control sample.

On average, the MIPS selected sample consists of $B/T < 0.5$ indicating that the sample is a bulge-dominated population. The few high Sérsic index galaxies could be due to bright central components with a low surface brightness disk. The control sample shows a slight increase in B/T with increasing n in agreement with previous studies but with a much shallower slope. By applying a morphological k-correction, we were able to compare morphologies at the same rest-frame wavelength over the redshift range of $0.25 \leq z \leq 1.25$. It is also of interest to see how these relations change with redshift, and in Figure 4.6 we show how the B/T vs. n relation

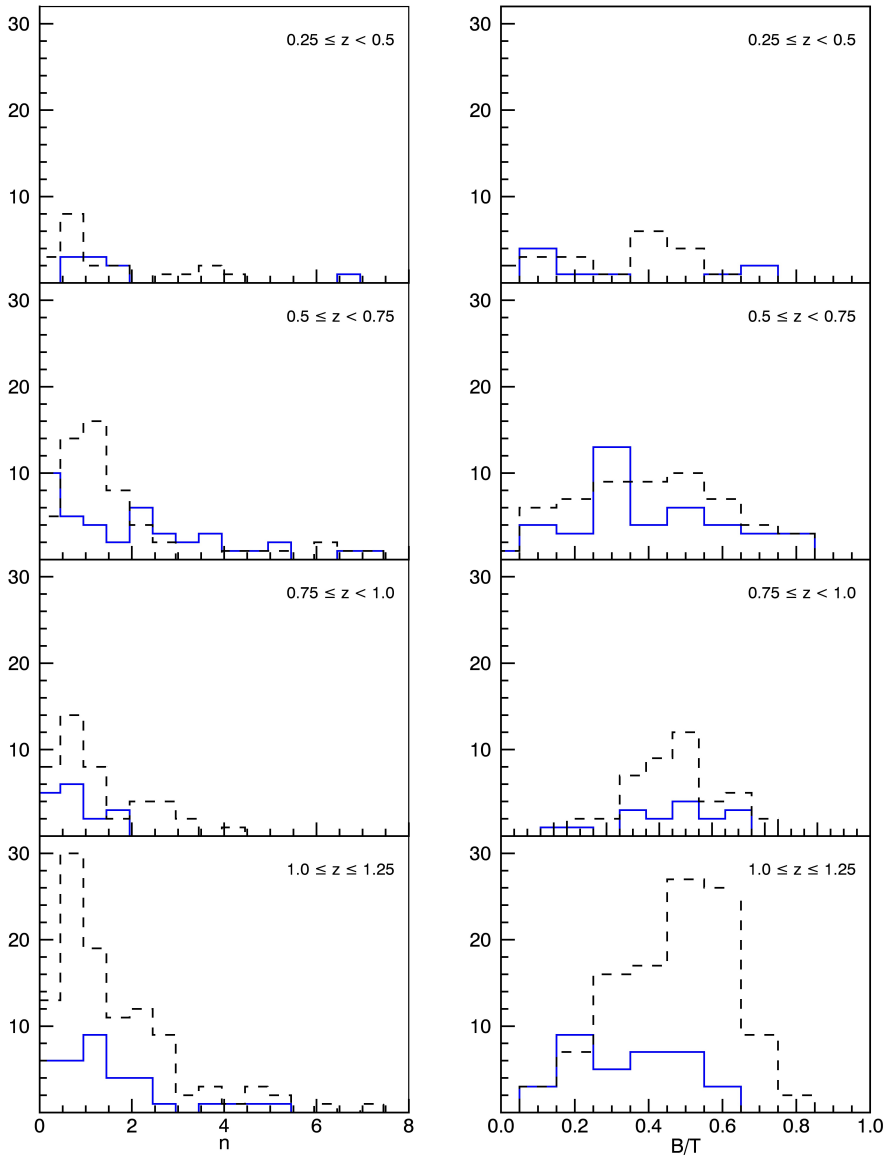

Figure 4.4: Rest-frame optical morphology distributions for the MIPS 24 μm sample (blue, solid line) and control sample (black, dashed line) in four different redshift bins. On the left we show the Sérsic Index distribution, while on the right we show the bulge-to-total flux ratio of the samples. Redshift increases down the page for the redshift bins $0.25 \leq z < 0.5$, $0.5 < z < 0.75$, $0.75 < z < 1.0$, and $1.0 < z \leq 1.25$. Bulge-dominated galaxies are considered to be those with $n \geq 2.5$ and $B/T \geq 0.5$, while disk-dominated galaxies have $n < 2.5$ and $B/T < 0.5$

evolves with redshift for the galaxy samples. We find that very few high Sérsic index galaxies are found in the redshift ranges $0.25 \leq z < 0.5$ and $0.75 \leq z < 1.0$, which could be due to

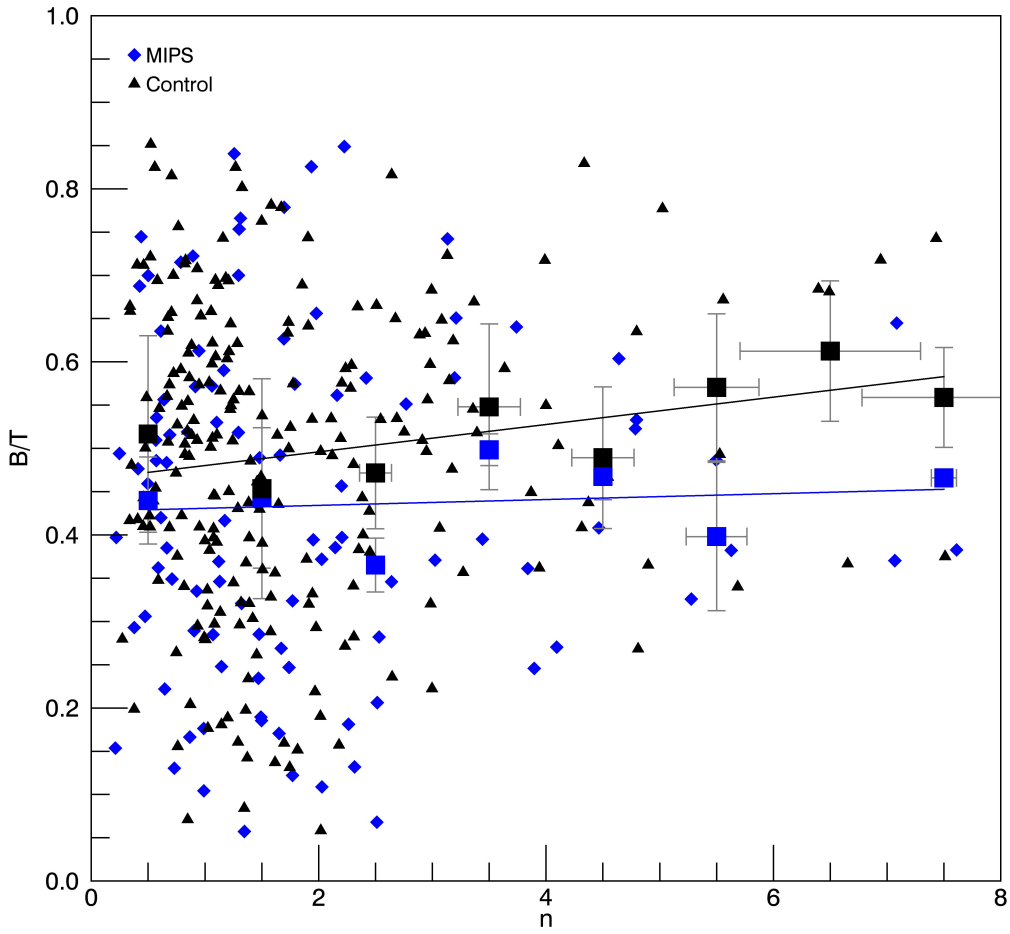

Figure 4.5: Rest-frame optical B/T vs. n morphology measurements for the MIPS 24 μm sample (blue) and control sample (black). Average errors are shown for the data binned in various Sérsic index ranges.

selection effects suggesting possible biases in the sample.

Our low redshift samples, $0.25 \leq z < 0.5$, suffer from small numbers due to the limited volume sampled at that redshift. However, in each redshift bin it appears that the general trend of increasing B/T with n does follow. The scatter in the B/T for galaxies with low n disagrees with previous work, which instead found an increasing linear trend between B/T and n. In

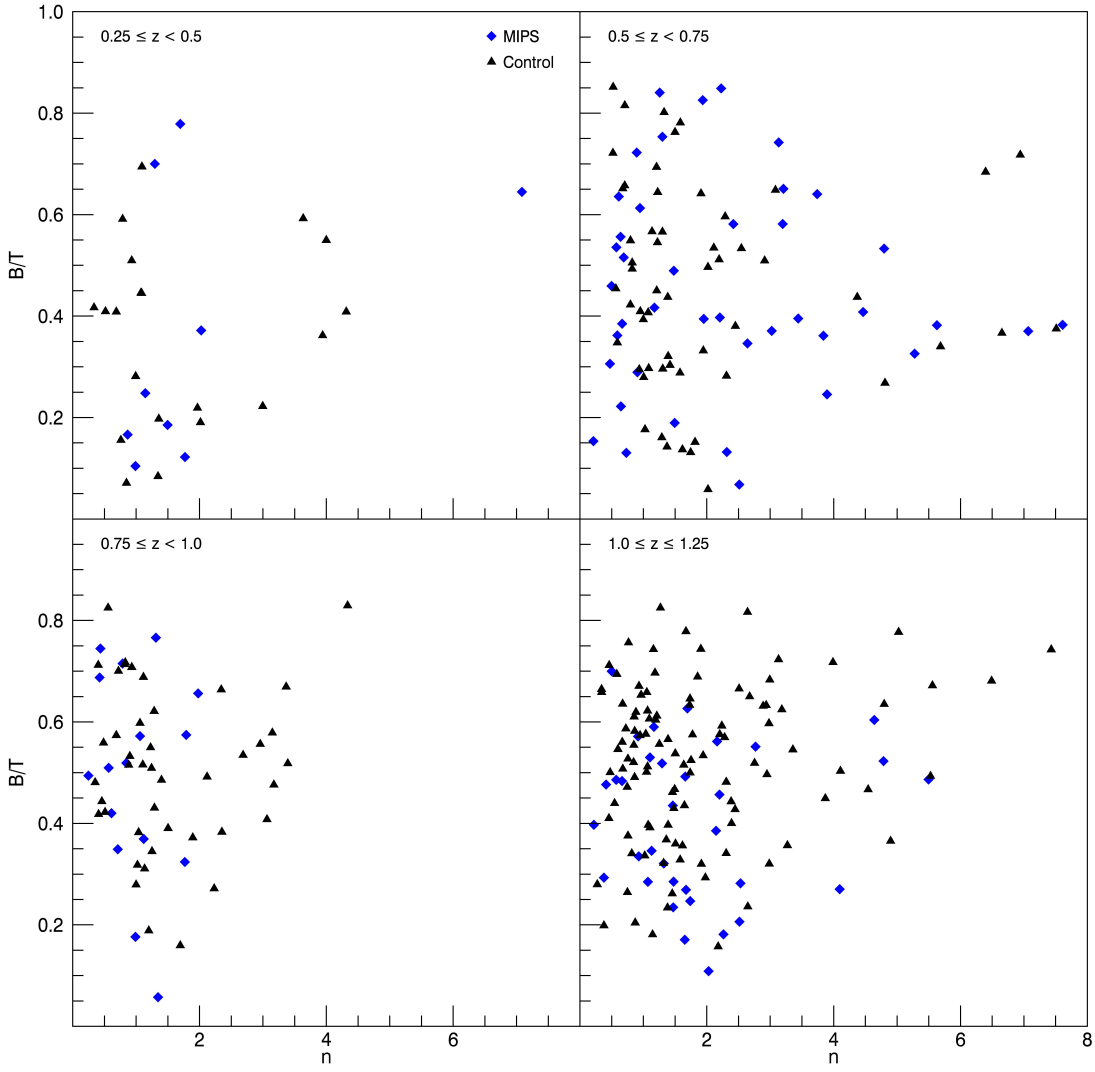

Figure 4.6: Rest-frame optical B/T vs. n morphology measurements for the MIPS 24 μm sample and control sample in four different redshift ranges.

these studies, the B/T was determined by fitting an $n = 4.0$ Sérsic function to the bulge and $n = 1.0$ Sérsic function to the disk of the galaxies (Bruce et al., 2012; Lang et al., 2014). This deceases the number of free parameters that Galfit must fit, which then decreases the odds of the fit being trapped in a local χ^2 minimum, but it is also applying constraints to a bulge which may not follow a DeVaucouleur's ($n = 4$) profile. In fact, it has been found that not all galaxy bulges follow a classical bulge light distribution, and instead consist of classical bulges ($n = 4$), pseudo

bulges ($n = 1$), as well as classical ellipticals with no disk component (Gadotti, 2009). With this is mind, we look at the disagreement between galaxies classified as disk galaxies by Sérsic index to their classification by B/T . We find that of the 76 galaxies classified as disk-dominated by Sérsic index ($n < 2.5$), 29 (38.2%) have $B/T \geq 0.5$, while 47 (61.8%) have agreement between the two morphological classifications. We also find that the control sample disagreement for the 177 disk-dominated galaxies, by Sérsic index, is very similar with 85 (48.0%) having $B/T \geq 0.5$ and 92 (52.0%) with $B/T < 0.5$. As shown in Gadotti 2009, the cause of this scatter is likely due to the sample containing galaxies with both classical and pseudobulges.

While the scatter in the B/T for disk-dominated galaxies is not entirely surprising, it is interesting to explore the fraction of the MIPS and control sample that are bulge-dominated. Since we expect the MIPS 24 μm detected sample to consist mainly of star-forming galaxies, we would not expect elliptical galaxies, yet we find that 24% MIPS 24 μm detected galaxies have Sérsic indices consistent with elliptical galaxies, $n \geq 2.5$. We find that 9 (37.5%) of these galaxies are also classified as bulge-dominated by B/T , while 15 (62.5%) instead have disk-dominated B/T flux ratios. The control sample has a little more agreement with 31 of the 49 (63.2%) ellipticals also having bulge-dominated B/T , and only 18 (36.7%) with disk-dominated B/T flux ratios. Due to the nature of MIPS 24 μm detected sources, we expect very few bulge-dominated galaxies in the sample, and we further investigated the nature of the MIPS 24 μm detected galaxies with bulge-dominated morphologies. The first possibility is whether the galaxy morphology has been misclassified. After visual inspection of galaxies with $n \geq 2.5$ and $B/T \geq 0.5$, we find that galaxies close to the $B/T \sim 0.5$ cut-off start to resemble lenticular galaxies, but are still bulge-dominated indicating that misclassification is not the issue. Once misclassification is ruled out, another possiblity for MIPS detection in an elliptical galaxy could be the presence of an AGN. We use the Chandra Deep Field-South (CDFS) Survey 4 Ms source catalog to determine if galaxies in our study have x-ray detection, as well as if that x-ray detection is indicative of the presence of an AGN (Xue et al., 2011). The CDFS Survey covers a total area of 464.6 arcmin^2, and the source catalogs from Xue et al. (2011) contain 740 sources detected in at least one of three X-ray bands (0.5-8 keV, full band; 0.5-2 keV, soft band; and 2-8 keV, hard band). In the

catalog, the sources have been identified as AGN, galaxies or stars with X-ray detection. This classification utilized distinct AGN physical properties as well as optical spectroscopic information to identify AGN candidates (see Xue et al. (2011) for more details). From this catalog, we find that 21 of the MIPS 24 μm galaxies and 2 of the controls sample have X-ray detection, and of these 11 of the MIPS 24 μm sources and both of the control galaxies have properties consistent with AGN. Of these galaxies, we find that this results in 25% of the galaxies classified as elliptical by Sérsic index and 10.5% of the galaxies classified as bulge-dominated by B/T have X-ray detection indicative of an AGN in the MIPS 24 μm sample, while the 2 galaxies that are AGN candidates in the control sample were classified as bulge-dominated by both morphological classification techniques. MIPS 24 μm detection is expected for disk-dominated galaxies, but there is still the possibility of additional flux due to an AGN. Of those classified as disk dominated by Sérsic index or B/T , we find that only 6.6% and 11.2%, respectively, contain an AGN. When combining the two morphological classifications, 22.2% of the MIPS 24 μm detected galaxies classified as bulge-dominated ellipticals have an AGN. This still leaves a significant fraction of bulge-dominated galaxies with MIPS 24 μm detection. The possibility of AGN is not completely removed, and the presence of an obscurred AGN could be the source of 24 μm emission, however these galaxies could also be dusty with centrally concentrated light distributions. We summarize the results of elliptical, MIPS detected galaxies in Table 4.2.

4.4.2 Morphological Inconsistencies

We look closer at galaxies that have a disagreement between their morphological classification by Sérsic index and the measured B/T. For the 15 galaxies classified as bulge-dominated or elliptical by Sérsic index but disky by B/T , we find that there is a mixture of morphologies. Most of the galaxies do appear to have a major bulge component, but more complicated structure, such as rings or barred spiral arms. We investigate the Galfit output for these galaxies in the form of the original postage stamp, model for the galaxy, and residual, and figure 4.7 shows a sample of these galaxies. We also find that 4 of these galaxies are AGN candidates. Many of these galaxies have B/T close to the cut-off limit of 0.5 or have Sérsic index values close the

Table 4.2: Summary of Elliptical Galaxies

Type[a]	N_{gal}[b]	Fraction AGN[c]
MIPS Detected Sample		
$n \geq 2.5$	24	25.0%
$B/T \geq 0.5$	38	10.5%
$n \geq 2.5$, $B/T \geq 0.5$	9	22.2%
$n \geq 2.5$, $B/T < 0.5$	15	44.4%
Control Sample		
$n \geq 2.5$	49	4.1%
$B/T \geq 0.5$	116	1.7%
$n \geq 2.5$, $B/T \geq 0.5$	31	6.5%
$n \geq 2.5$, $B/T < 0.5$	18	0%

[a] Determined by n, B/T or combination of the two. .
[b] Number of galaxies with specified morphology classification.
[c] Percentages of galaxies with X-ray detection indicative of AGN candidates.

cut-off of $n \geq 2.5$ for bulge-dominated, elliptical morphologies. Overall, we see this group of galaxies as an intermediate class between bulge-dominated disk galaxies and elliptical galaxies.

When we looked further into the 29 galaxies with disk-like Sérsic indices, but bulge-dominated B/T , we find the galaxies have an overall disk structure, but with large central bulges, more like SA/SB Hubble Type galaxies. We also find that 4 of these galaxies are AGN candidates, which could lead to a larger bulge flux fraction. In this study we find that the combination of galaxy Sérsic index and B/T , determined using a free Sérsic fit to the bulge, for disk galaxies can help to separate different Hubble types from those that are considered early-type (Sa-Sb) and late-type spirals (Sc-Sd). Through knowledge of the overall galaxy Sérsic index as well as the bulge strength obtained through B/T, a better understanding of the different spiral galaxies is obtained.

4.4.3 Size Evolution

While the B/T and n measurements are important in studying the morphology of the samples, another interesting study into the morphology of the MIPS 24 μm sample is the size evolution with redshift. In figure 4.8, we separate the high and low Sérsic index galaxies to investigate how the sizes, in this case the effective radius r_e, of these different galaxy populations evolve

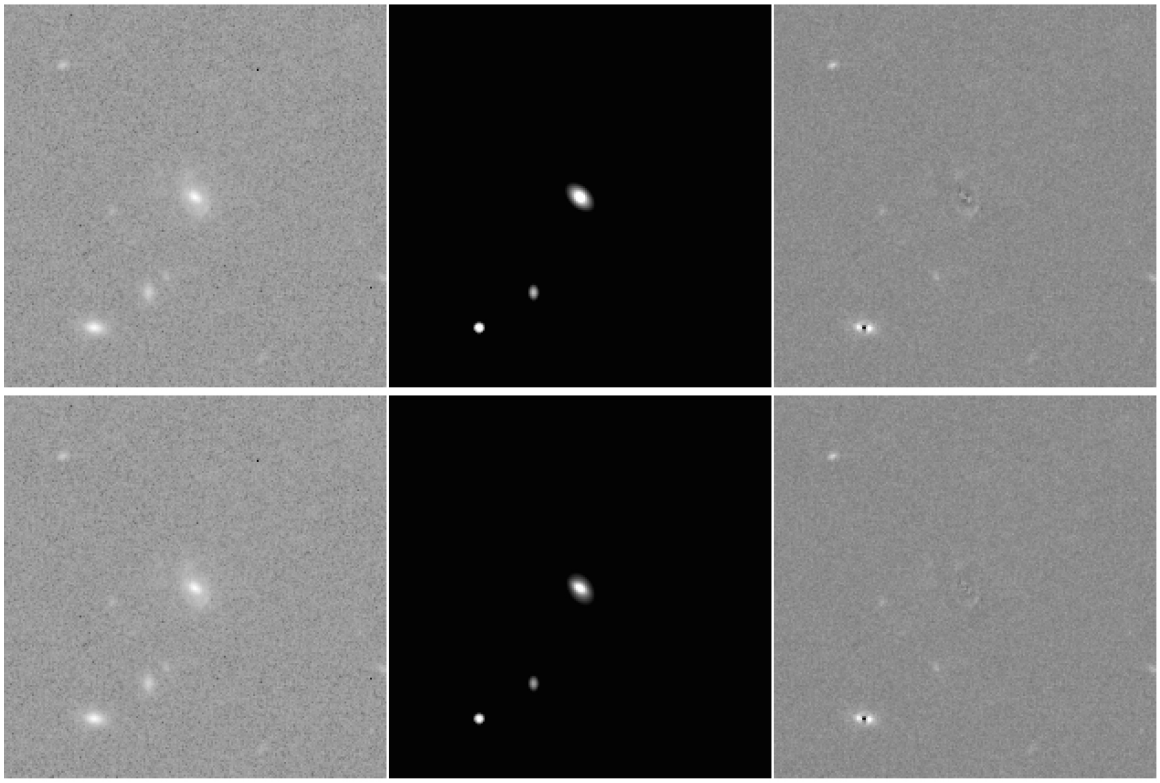

Figure 4.7: Restframe optical Galfit output images for a MIPS 24 μm detected galaxy with $n \geq 2.5$, but with $B/T < 0.5$. (a) We show the original HST image, Galfit single Sérsic model, and residual (left to right) of the galaxy. (b) The same as (a) but for a two component, bulge-disk decomposition.

with time. We observe a large scatter in the size measurements of the galaxies with no apparent trend in galaxy size evolution. If we further separate these galaxy samples in to high and low Sérsic index galaxies with bulge-dominated and disk-dominated morphologies, we still see no apparent evolution with time. These findings are in agreement with other studies, which find that present-day spiral and elliptical galaxies were formed beyond $z = 1$ with very little size evolution occurring after this epoch (Lilly et al., 1998; Simard et al., 1999; Im et al., 2002; Stanford et al., 2004; Ravindranath et al., 2004; Barden et al., 2005).

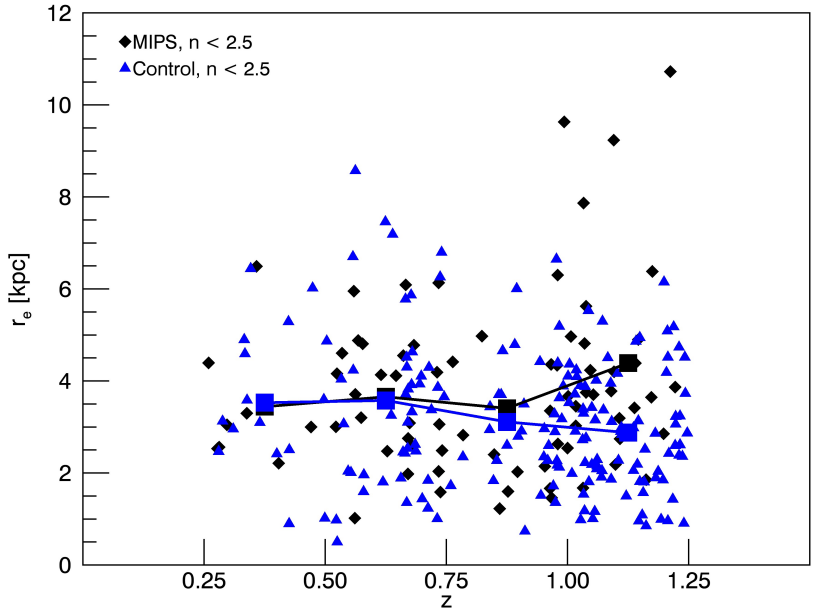

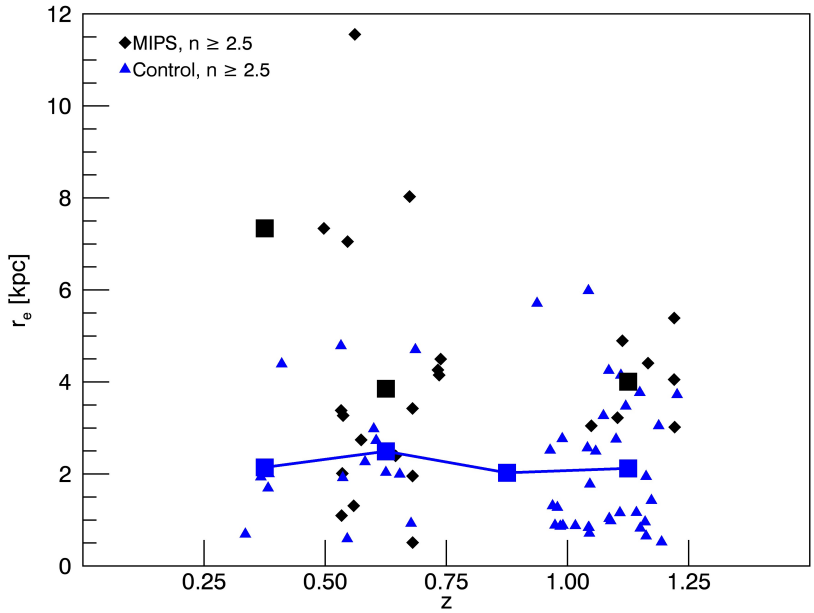

Figure 4.8: Rest-frame B-band effective radii r_e, of the MIPS 24 μm (diamonds) and control galaxies (triangles) as a function of redshift. In figure (a) we show the galaxies with $n < 2.5$ and (b) galaxies with $n \geq 2.5$.

4.5 Discussion and Conclusions

We have analyzed the morphology of 470 MIPS 24 μm detected galaxies in the GOODS-S field, for which after removing galaxies with low axis ratios, we successfully fit both single Sérsic function fits as well as a bulge and disk component to a final sample of 100 galaxies. We find that the sample is dominated by disk galaxies through all redshift bins when classified by Sérsic index, as expected. We also decomposed the galaxies into bulge and disk components as another morphological analysis indicated bulge-dominated and disk-dominated systems. Previous studies have found that the systematic change of B/T along the morphological sequence is not caused by disks but mostly by bulges (Oohama et al., 2009), indicating that galaxies with larger n values would systematically have larger B/T values. By fitting an $n = 4.0$ Sérsic function to the bulge and $n = 1.0$ Sérsic function to the disk of the galaxies, these studies determined that disk-dominated galaxies consisted of those with $0 < n < 2$ and $B/T < 0.5$, while bulge-dominated galaxies are those with $n > 2$ and $B/T > 0.5$ (Bruce et al., 2012). Other studies, however, have indicated that galaxy bulges cannot all be assumed to be a perfect deVaucouleur's profile light distribution, but instead consist of classical bulges ($n = 4$), pseudo bulges ($n = 1$), as well as classical ellipticals with no disk component (Gadotti, 2009). With this in mind, we fit a free Sérsic fit to the bulge and along with an exponential disk component allowing for the possibility of classical bulges and pseudo bulges. We find that for the majority of the redshift ranges studied, MIPS 24 μm detected galaxies are disk-dominated, however the higher redshift range of $0.75 < z < 1.0$ was found to be bulge-dominated. After further analysis, we find that these galaxies are, for the most part, disk galaxies with central bulge contribution, similar to Sa/Sb Hubble types. Overall, we do find an expected population of disk galaxies with MIPS 24 μm detection, but with varying B/T .

We compared the morphology of the MIPS 24 μm detected sample to a control sample of 1109 galaxies without MIPS 24 μm detection, which after removing edge-on galaxies with low axis ratios and keeping those with successful single Sérsic and bulge-disk decompositions resulted in a final sample of 226 galaxies. In comparison to the MIPS 24 μm detected galaxies,

we observe a more consistent fraction of galaxies with elliptical Sérsic indices, as well as a significant fraction of the galaxies as bulge-dominated. Also, while the galaxies at higher redshift are bulge-dominated, we notice an increasing fraction of disk-dominated galaxies, as we move closer to present day, with the sample becoming disk-dominated at the $0.5 < z < 0.5$ redshift interval. Seeing as redshift range of the samples are after the peak of star formation, this would indicate that galaxies should be evolving into older, less star-forming populations, which would be bulge-dominated. However, if the bulge formation actually occurs before the buildup of the disk (Bouwens et al., 1999), then could be indicative of the end of the epoch of bulge formation. Another possible cause of this trend could be the volume limited sample as we get to lower redshift not being indicative of the Universe as a whole.

We do, however, find a fraction of the MIPS 24 μm galaxies with elliptical, bulge-dominated morphologies, which is unexpected due to the nature of MIPS 24 μm emission. Another source of MIPS 24 μm emission could be due to AGN, which are powerful UV emitters, and we find that 25% of the elliptical galaxies, classified by Sérsic index, contain AGN candidates. This still leaves a large fraction of elliptical galaxies with unexpected MIPS 24 μm detection. To further investigate the cause of this, we further examine the galaxies without X-ray detection indicative of AGN, taking into account mean errors, to see if the scatter could change the morphological classification of the galaxies. Two of these galaxies classified as elliptical by Sérsic index have n values close to the 2.5 cut, which could result in a different classification by error. For the remaining galaxies with elliptical light profiles, we further investigate whether any of the fits resulted in Sérsic indices of $n > 6.0$. Galaxies with Sérsic indices greater than 6.0 could be contaminated by AGN or central point-sources. A disk with a bright, central point source could easily be misclassified as an elliptical galaxy by the bulge-dominance of the light profile. Of the galaxies with elliptical morphologies, we find that only 3 of the 24 galaxies have large Sérsic indices, one of which is an AGN candidate, still leaving 16 galaxies with an unknown cause of MIPS 24 μm detection. One hypothesis we have as to why these galaxies that should no longer be star forming to have MIPS 24 μm detection could be due to obscurred AGN, not detected in X-ray observations. For those galaxies with elliptical Sérsic indices and bulge-dominated B/T ,

we hypothesize that these galaxies could be dust obscured star-forming galaxies, which would explain the MIPS 24 μm detection for a galaxy with a high Sérsic index, and would also result in a bulge-dominated multi-component morphology. After visual inspection, we find that these galaxies do show morphologies consistent with this hypothesis.

Aside from morphological analysis, we also compared the size evolution of the MIPS 24 μm detected sample of galaxies compared to those in the control sample. We overall found no size evolution for our MIPS 24 μm detected of control sample galaxies within the redshift range of $0.25 \leq z \leq 1.25$ in the GOOD-S CANDELS field.

In this chapter, we studied a sample of 470 MIPS 24 μm detected galaxies in the GOODS-S field in order to characterize the morphological properties and possible evolution within the redshift range of $0.25 \leq z \leq 1.25$. We use 2D modeling with GALFIT to determine the Sérsic index by fitting a single Sérsic function to the galaxy light profiles, as well as a two component fit to the bulge and disk of the galaxies to obtain the B/T flux ratio. We find that the overall population of these star-forming galaxies is dominated by disk-like galaxies (47%), as classified by both morphological techniques, and we find that 76% of the MIPS galaxies have a disk-like morphology as classified by Sérsic index. We compare this galaxy sample to a control sample selected using the same methods as the MIPS detected sample but without 24 μm detection resulting in a sample of 1109 galaxies. We observe a clear dominance of disk galaxies in the MIPS sample with very few elliptical galaxies. Of the elliptical galaxies with 24 μm emission, we find that 25% of these galaxies contain AGN candidates, which could be the source of the 24 μm flux. After eliminating the possibility of misclassification, the remaining bulge-dominated galaxies' MIPS detection could be due obscured AGN. We see a large population of disk galaxies in the control sample as well, but also observe a larger percentage of elliptical galaxies in comparison to the MIPS sample. This agrees with our expectations that MIPS 24 μm emission comes primarily from young, massive stars that would be located in actively star-forming, disk galaxies.

Chapter 5

The MOSDEF Survey: Rest-frame Optical Morphological Analysis

5.1 INTRODUCTION

Observations of galaxy morphology at various look-back times provide important insight into processes associated with galaxy formation. Through morphological studies, it is believe that the Hubble Sequence was already in place by $z \sim 1$ (Abraham et al., 1996; Schade et al., 1999; Brinchmann et al., 1998; Lilly et al., 1998; Marleau and Simard, 1998; Im et al., 1999; van den Bergh, 2001; Trujillo and Aguerri, 2004; Conselice et al., 2005) indicating that the formation and evolution of the bulge and disk components of galaxies must have occurred at higher redshift (Ravindranath et al., 2006). By comparing observed morphological properties to other galaxy properties, such as mass, star formation rate (SFR), and metallicity, a detailed evolution model can be studied and help us to understand how galaxies assembled into the structures we see today.

Additional insight into galaxy evolution scenarios can be traced through observations and morphological analysis in multiple wavelengths. In order to accurately compare galaxy samples, it is important to probe the same rest-frame wavelength. With the currently available deep surveys carried out over the years, a vast quantity of data is available to probe galaxy properties

across a wide range of rest-frame wavelengths and look-back times. Some studies have found that a morphological *k*-correction is unnecessary due to a limited impact on conclusions (Wuyts et al., 2011; Bond et al., 2011), but an importance should still be placed upon understanding morphology in the same rest-frame wavelength to ensure that logical comparisons of similar galaxy properties can be achieved.

The star-formation rate (SFR) and stellar mass (M_*) relationship for star-forming galaxies has shown to form a sequence, so-called main sequence of star formation, at $z \sim 0$, which has been shown to hold out to $z \sim 2.5$ (Wuyts et al., 2011). Correlating this with parametric measurements of galaxy morphology, those lying on the star-forming main sequence would have lower Sérsic indices than those off the relation, while massive galaxies with low SFR would be red with higher Sérsic indices (Peth et al., 2015). The study of chemical abundances in galaxies throughout time also provides important insight into their evolution. From the local universe to $z \sim 3.5$, a clear relationship between the stellar mass (M_*) of a galaxy and its gas-phase oxygen abundance, known as the mass-metallicity relationship (MZR), has been found indicating that galaxies with lower stellar mass have lower metallicity than those with higher M_* (Tremonti et al., 2004; Kewley and Ellison, 2008; Andrews and Martini, 2013), although it has been found to evolve with redshift in that a given stellar mass will have a lower metallicity at higher redshift (Erb et al., 2006; Maiolino et al., 2008; Henry et al., 2013; Maier et al., 2014; Maseda et al., 2014; Steidel et al., 2014; Sanders et al., 2015). One interesting aspect that has not been studied, is how the stellar mass and metallicity relation correlates with galaxy morphology. By understanding how the MZR evolves for different morphological types with time, important insight can be gained if the underlying physical processes are understood. The local MZR has been found to depend on SFR following a two-dimensional surface with a scatter of only 0.05 dex in metallicity when comparing the M_*-SFR-metallicity space (Mannucci et al., 2010). Seeing as previous work has shown that the SFR-M_* relation shows a morphological dependence, one would also expect such a correlation for MZR.

In this work, we present the results on the morphological analysis of observations from the MOSFIRE Deep Evolution Field (MOSDEF) Survey, which will contain rest-frame optical spectra

of ∼1500 galaxies at $1.37 \leq z \leq 3.5$ upon completion. We focus on the redshift ranges of $1.37 \leq z \leq 1.70$ and $2.09 \leq z \leq 2.61$ for which reliable parametric morphology measurements can be completed. The outline of the chapter is as follows. In Section 5.2, we present the properties of our sample and the measurements of morphology, SFRs, stellar masses, and metallicities. In Section 5.3, we present the morphological analysis of the galaxies from the MOSDEF sample, as well as morphological dependence of other galaxy properties. Finally, we summarize and discuss our results in Section 5.4. We assume standard ΛCDM cosmology throughout with $\Omega_m = 0.3$, $\Omega_\lambda = 0.7$, and $H_0 = 70$ km s^{-1} Mpc^{-1}.

5.2 Sample Selection

5.2.1 The MOSDEF Survey

As described in Chapter 3, the MOSDEF survey is a large multi-year survey with the MOSFIRE multi-object spectrometer on the Keck I telescope (McLean et al., 2012). The aim of the survey is to obtain rest-frame optical spectra of ∼ 1500 H-selected galaxies to study their stellar, gaseous, metal, dust, and black hole content by targeting strong nebular emission lines as well as stellar continuum and absorption features. The MOSDEF observations are conducted in three CANDELS fields Koekemoer et al. (2011); Grogin et al. (2011)), consisting of AEGIS, COSMOS, GOODS-N, covering ∼500 arcmin^2 and targeting three redshift bins: $1.37 \leq z \leq 1.70$, $2.09 \leq z \leq 2.61$, and $2.95 \leq z \leq 3.80$. Targets for spectroscopy are prioritized by their H-band magnitude and the availability of spectroscopic, grism, and photometric redshifts, down to H = 24.0, 24.5, and 25.0 magnitude, for each redshift bin respectively, using the photometric and spectroscopic catalogs from the 3D-HST survey (Skelton et al., 2014). The survey requires two or three filters per slit mask in order to obtain multiple rest-frame optical emission lines for each galaxy. For the lowest redshift interval, $1.37 \leq z \leq 1.70$, Hβ and [OIII] are targeted in the J band, while Hα, [NII] and [SII] are targeted in the H band. Additionally, for targets at the high end of this redshift bin, $z \geq 1.61$, [OII] can also be targeted in the Y band. For the middle redshift range, $2.09 \leq z \leq 2.61$, the same features appear in J, H, and K, while for the highest range, $2.95 \leq z$

≤ 3.80, [OII] falls in the H band and Hβ and [OIII] appear in the K band. Other features such as Balmer absorption features, the 4000 break, and other continuum features and absorption lines are targeted to fully investigate galaxy formation, evolution and content in this regime. Details of the survey strategy, observations, data reduction, and characteristics of the full galaxy sample are described in Kriek et al. (2015). In this analysis, we use the data accumulated from the first two years of the survey as well as the parent catalogs selected from the 3D-HST survey.

5.2.2 Main Sequence of Star Forming Galaxies

As described in Shivaei et al. (2015), a sample of 342 galaxies were selected from the full MOSDEF sample with secure redshifts and coverage of both Hα and Hβ lines. The sample was then selected based on the following criteria:

1. Redshifts spanning the range $1.37 \leq z \leq 1.70$ and $2.09 \leq z \leq 2.61$
2. Galaxies not flagged as AGN, which removed 49 based on their IR and X-ray properties, as well as high [NII]/Hα ratios (Coil et al., 2015)
3. S/N ≥ 3 for Hα and Hβ
4. Galaxies that are not quiescent as determined using a rest-frame UVJ color selection (Williams et al., 2009)

This resulted in a final sample of 215 galaxies detected in both Hα and Hβ

5.2.3 Mass-Metallicity Sample

A sample of star-forming galaxies at $z \sim 2.3$ were selected from the MOSDEF sample using the criteria from Sanders et al. (2015).

1. Redshift in the range of $2.08 \leq z \leq 2.61$ in order to have spectral coverage of Hα, Hβ, [OIII] λ5007, and [NII] λ5484.
2. S/N ≥ 3 for Hα and Hβ to reliably measure the dust-corrected star formation rate.

3. Galaxies not flagged as an AGN.

4. If [NII] is detected, we also require that log([NII]/Hα) < -0.3

This results in a sample of 143 $z \sim 2.3$ star-forming galaxies, consisting of 84 individual detections and 59 upper limits. This now includes season two MOSDEF observations, and the sample size has increased since the results of Sanders et al. (2015). Throughout the remainder of this chapter, the term metallicity refers to the gas-phase oxygen abundance (12 + log(O/H)), which acts as a proxy for the true gas-phase metallicity.

5.2.4 Morphological Measurements

We begin with the MOSDEF parent sample, which was adopted from photometric catalogs and grism spectra provided by the 3D-HST collaboration across the three redshift bins in the five different fields. We then matched the parent catalogs to SExtractor catalogs (Bertin and Arnouts, 1996) prepared by the CANDELS team in all available wavelengths (GOODS-N & GOODS-S: F160W, F125W, F105W, F850LP, F775W, F606W, F435W; COSMOS, AEGIS, & UDS: F160W, F125W, F814W, F606W), which have high-resolution HST WFC3 and ACS imaging critical for morphology measurements.

Morphology of the galaxies is measured by modeling the two-dimensional surface brightness distribution with a Sérsic function (de Vaucouleurs, 1948; Sersic, 1968). This is done using the GALFIT software (Peng et al., 2002, 2010), which convolves the 2D analytical model with the PSF using the Levenberg-Marquardt algorithm for χ^2 minimization giving the optimum fit. In order to consistently compare galaxy properties at different redshifts, we measure their Sersic parameters at the same rest-frame wavelength. To allow such measurements over our selected redshift range, in a wavelength as close as possible to optical, we use multi-wavelength Hubble Space Telescope Wide-Field Camera 3 (HST WFC3) images to measure the rest-frame *B*-band morphologies of the galaxy sample. This was completed using *J*-band measurements for the $1.37 \leq z \leq 1.70$, and *H*-band for the $2.09 \leq z \leq 2.61$ sample. However, morphological measurements were completed in all available passbands.

The input parameters for GALFIT for each galaxy were taken from the SExtractor catalogs produced by the CANDELS team, which are psf-matched to the H-band SExtractor detections. The background sky value was held fixed for the Galfit measurement, and was determined using a flux growth method outlined in Barden et al. (2012), which calculates the average flux in elliptical annuli centered around the object of interest, while excluding flux from neighboring sources. We convolve the model galaxies produced by Galfit with PSFs generated by the CANDELS team using stacked stars. For the single Sérsic function fit to the galaxy sample, the Sérsic index, a measure of the concentration of the light profile, has been constrained between the values of 0.2 and 8.0 in order to avoid arbitrarily large values caused by active galactic nuclei (AGN) or compact, central point sources (Ravindranath et al., 2006). In addition to the overall Sérsic function fit with GALFIT, morphological classifications were also completed using a two-component GALFIT fit of the galaxy bulge and disk components simultaneously. For the bulge component, we fit a Sérsic function, where the Sérsic index, n, is a free parameter ranging between 0.2 and 8.0. The disk component of the bulge-to-disk decomposition is fit using an exponential disk, where the Sésic index is fixed to $n = 1$. All other parameters (total magnitude, r_e or r_s, axis ratio, and position angle) are allowed to vary independently. A two-component fit adds additional free parameters resulting in larger errors, and we reject galaxies with large χ^2 values and objects that have been flagged for unreliable measurements for both the single Sérsic fit and the two-component bulge-disk decomposition. In Figure 5.1 we show an example galaxy from the GOODS-N field, with successful morphological measurements in all seven passbands. Lastly, we apply a morphological k-correction to measure and compare the same rest-frame morphologies using the J- and H—band (F125W and F160W) measurements for the $1.37 \leq z \leq 1.70$ and $2.08 \leq z \leq 2.61$ redshift bins, respectively, obtaining rest-frame optical morphology measurements. This resulted in a final sample of 194 galaxies with reliable, rest-frame optical, single- and two-component morphology measurements with available rest-frame optical spectral lines.

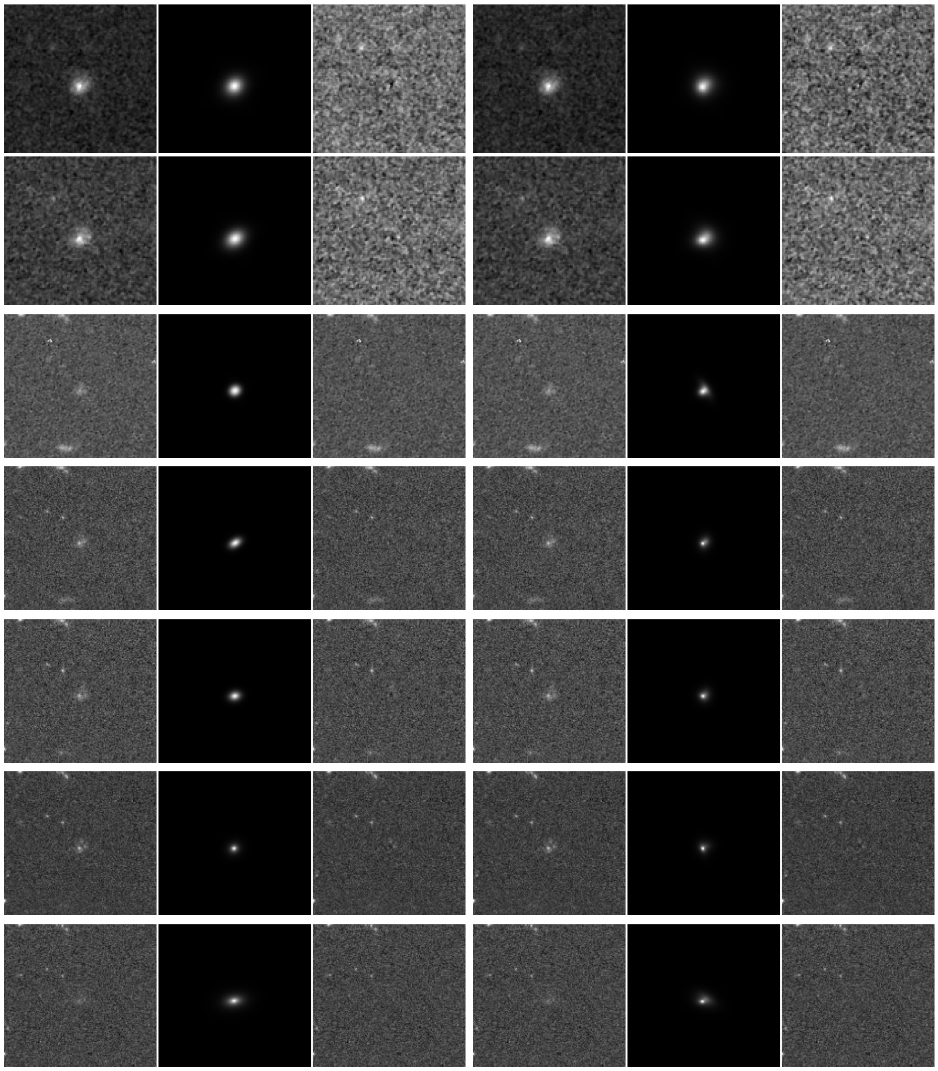

Figure 5.1: Galfit output images for an example galaxy from the GOODS-N field. On the left we show single Sérsic component fits to the galaxy in 7 different passbands: F160W, F125W, F105W, F850LP, F775W, F606W, F435W, from top to bottom. On the right we show the same galaxy fit with two components, a bulge and disk, across the same seven wavelengths. Each Galfit output image includes the original postage stamp on the left, the model of the galaxy convolved with the PSF in the center, and the residual on the right.

5.2.5 Mass, SFR, and Metallicity Measurements

Stellar masses were estimated using the MOSDEF redshifts and pre-existing photometric data assembled by the 3D-HST team (Skelton et al., 2014). The photometric data set for each galaxy was modeled with the SED-fitting program FAST (Kriek et al., 2009), assuming the stellar pop-

ulation synthesis models of Conroy et al. (2009) and a Chabrier (2003) IMF. Star-formation histories were parameterized using so-called delayed-τ models of the form SFR(t) $\propto te^{-t/\tau}$, where t is the stellar-population age, and τ is the e-folding timescale in the SFR. Dust extinction was described using the Calzetti et al. (2000) attenuation curve. For each galaxy, a grid in stellar population age, e-folding timescale, metallicity, and dust extinction was explored and χ^2 minimization was used to find the best-fitting model. The normalization of the best-fit model yielded the stellar mass. Confidence intervals in each stellar population parameter were determined using Monte Carlo simulations where the input SED was perturbed and refit 500 times. SFRs are based on dust-corrected Hα luminosities. Dust corrections are estimated from the ratio of Hα/Hβ, in which Hα and Hβ fluxes have been corrected for underlying Balmer absorption (Reddy et al., 2015). Balmer absorption equivalent widths for Hα and Hβ are measured from the best-fit SED model for each galaxy. E(B - V)$_{neb}$ is calculated assuming an intrinsic ratio of 2.86 and using the dust-attenuation curve of Calzetti et al. (2000). Dust-corrected Hα luminosities are translated into SFRs using the calibration of Kennicutt (1998), converted to a Chabrier (2003) IMF (Sanders et al., 2015). The dust-corrected SFR and mass are plotted as the star-forming main sequence in Figure 5.2. A linear regression was fit to the data in green, while the fit from Shivaei et al. (2015) is shown in red. The difference in the best-fit to the data is due to different mass measurements used in each study. The mass measurements in Shivaei et al. (2015) were also determined using SED-fitting but assuming a 50 Myr lower limit on the age of the galaxies, assumed to be the typical dynamical time scale at this redshift (Reddy et al., 2015).

Oxygen abundances, or metallicity, were estimated using the N2 (log ([NII]λ6584/Hα)) and O3N2 (log ([OIII]λ5007/Hβ)/log ([NII]λ6584/Hα)) indicators. These indicators were calibrated using the prescription from Pettini and Pagel (2004), which are based on a sample of HII regions with direct electron temperature measurements, and are calibrated by

$$12 + \log(\mathrm{O/H}) = 8.90 + 0.57 \times \mathrm{N2} \tag{5.1}$$

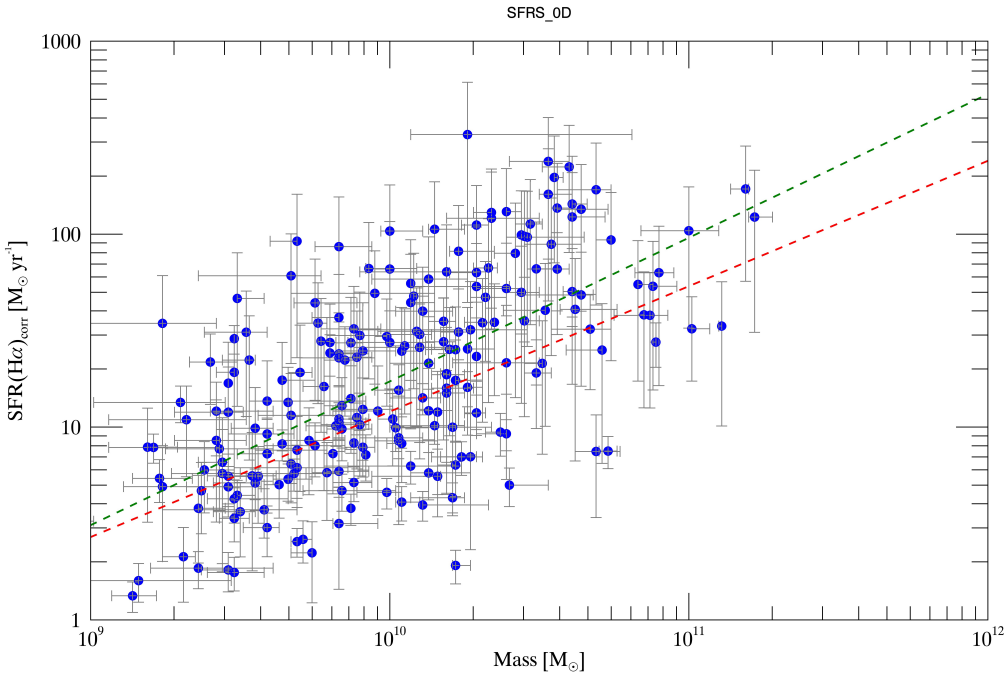

Figure 5.2: SFR(Hα) as a function of stellar mass for star-forming galaxies in the MOSDEF survey in the range of $1.37 \leq z \leq 2.61$, known as the star-forming main sequence. All points have both Hα and Hβ detections. The green dashed line shows the best linear fit to the data for galaxies with $\log(M_*/M_\odot) > 9.5$, while the red dashed line shows the best-fit line to the $1.37 \leq z \leq 2.61$ MOSDEF sample presented in Shivaei et al. (2015) also for galaxies with $\log(M_*/M_\odot) > 9.5$.

$$12 + \log(O/H) = 8.73 - 0.32 \times O3N2, \tag{5.2}$$

where $12 + \log(O/H)$ is the oxygen abundance. The initial MZR relation for the 143 galaxies is shown in Figure 5.3.

5.3 Results

5.3.1 Rest-frame Optical Morphology

We classify the overall morphology of the galaxy sample based on the two different morphological measurements. Galaxies with Sérsic index, $n \geq 2.5$, and the bulge-to-total flux ratio, $B/T \geq 0.5$, are typically classified as bulge-dominated, elliptical galaxies, while galaxies with

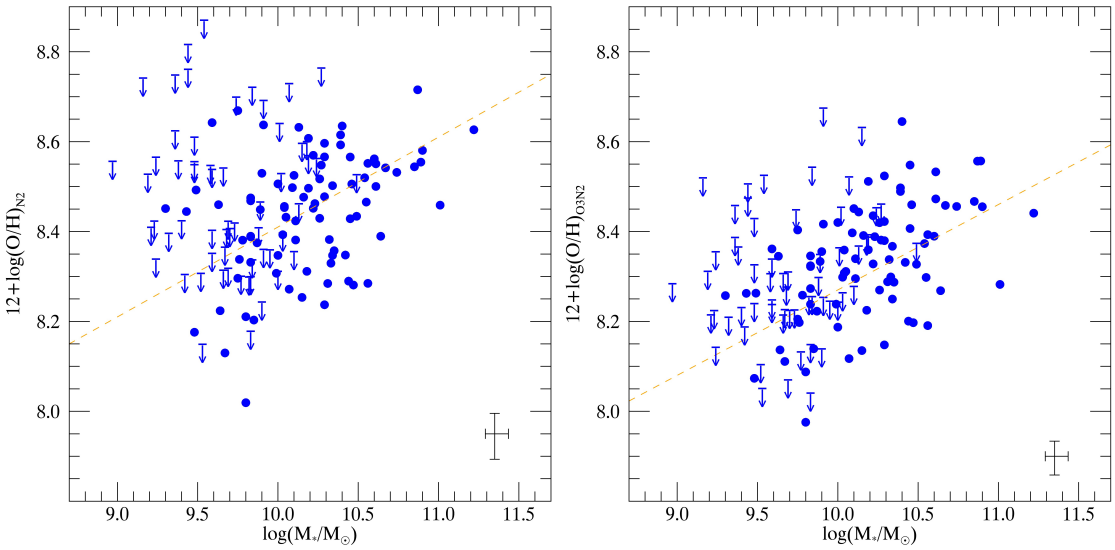

Figure 5.3: MZR for $z \sim 2.3$ star-forming galaxies with metallicities determined using N2 (left) and O3N2 (right) indicators. Blue circles indicate MOSDEF galaxies with 3σ or greater significance in Hα, Hβ, and [OIII] λ5007. Blue arrows indicate 3σ upper limits where [NII] λ6584 was not detected. The orange dashed line is the best-fit line to the $z \sim 2.3$ N2 and O3N2 MZR as observed by Steidel et al. (2014). The black error bar in the lower left-hand corner shows the mean uncertainty in $12 + \log$ (O/H) and stellar mass for individual MOSDEF galaxies, excluding the calibration error.

$n < 2.5$ are disk galaxies with varying degrees of bulge fraction. Those with $B/T \geq 0.5$, are more like Hubble Type Sa or Sb, galaxies with a larger bulge concentration, while those with $B/T < 0.5$ are more late-type spirals, with a small bulge fraction. Example color images of the different galaxy classifications are shown in Figure 5.4. We first look at the distribution of Sérsic indices and B/T for the sample, shown in Figure 5.5. The MOSDEF sample used in this chapter consists primarily of emission line galaxies with on-going star formation. We therefore expect that the majority of the galaxies will have $n < 2.5$, but could have a variety of B/T values. The distributions show that the Sérsic indices peak around $n = 1$, and contains very few galaxies with $n \geq 2.5$. The B/T peaks between $B/T \sim 0.5$ and $B/T \sim 0.6$ with the sample being more heavily weighted towards $B/T < 0.5$.

Next, we investigate the correlation between n and B/T. Previous work has found that the galaxy Sérsic index is a poor proxy for B/T (Gadotti, 2009), meaning there is not a one to

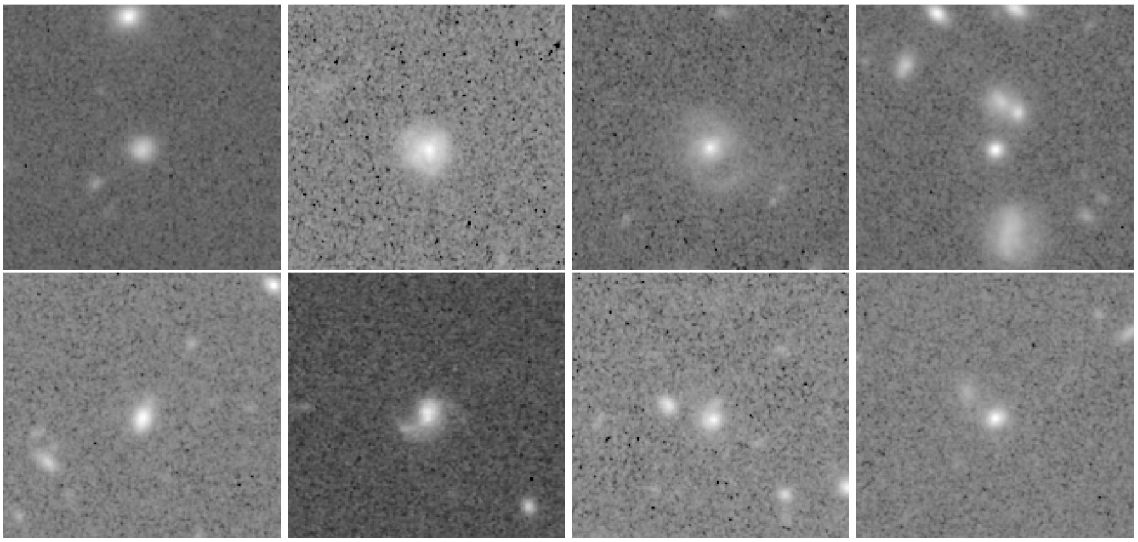

Figure 5.4: Rest-frame B-band images of galaxies from different morphological classifications observed in the MOSDEF survey. The top row shows galaxies from the redshift range $1.37 \leq z \leq 1.70$ and the bottom shows galaxies with $2.09 \leq z \leq 2.61$. From left to right we shows galaxies with the following morphologies: $n < 2.5$ and $B/T < 0.5$, $n < 2.5$ and $B/T \geq 0.5$, $n \geq 2.5$ and $B/T < 0.5$, $n \geq 2.5$ and $B/T \geq 0.5$

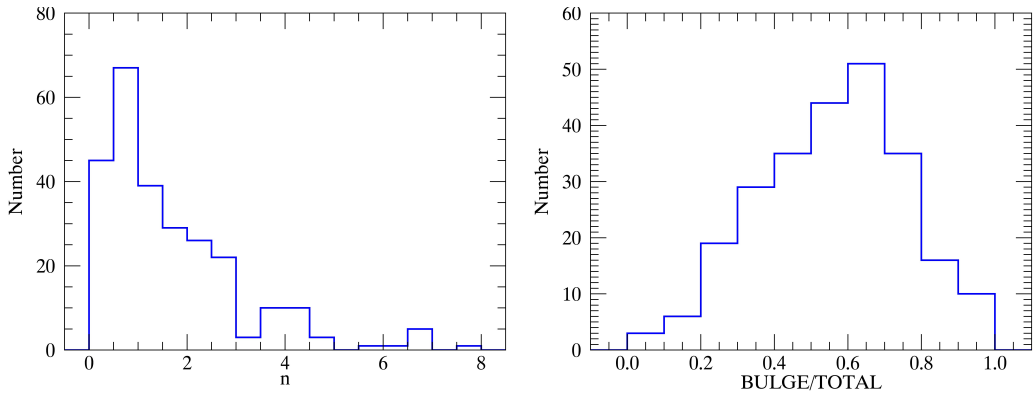

Figure 5.5: Measured Sérsic index, n, and bulge-to-total flux ratios, B/T, distributions for the MOSDEF galaxies with reliable morphology measurements. The Sérsic index is obtained from a single Sérsic function fit to the galaxy representing the overall galaxy n, while the B/T is determine using a two-component bulge-disk decomposition with a Sérsic function bulge and an exponential disk.

one translation between n and B/T (Lang et al., 2014; Andredakis et al., 1995; de Jong et al., 2004; Cibinel et al., 2013; Bruce et al., 2012). However, information regarding the morphology of the galaxy sample can still be obtained using a combination of the two values. Figure 5.6,

shows a large scatter with little or no correlation between the overall galaxy Sérsic index and the measured bulge-to-total flux ratio. This is in contrast to other high redshift work on two-component decomposition of galaxies in the CANDELS fields (Lang et al., 2014), but previous work completed bulge-disk decomposition using a DeVaucouleur's $n = 4$ profile for the bulge while we allow the bulge Sérsic index to vary in the range $0.2 < n < 8.0$. This allows the possibility of both classical and pseudobulges to exist in the galaxy sample, similar to a study of nearby galaxies done by Gadotti (2009), which could provide insight into galaxy formation and evolution. To further understand what this distribution indicates, we look at four different possible galaxy classifications: galaxies with $n \geq 2.5$ and $B/T \geq 0.5$, galaxies with $n \geq 2.5$ and $B/T < 0.5$, galaxies with $n < 2.5$ and $B/T \geq 0.5$, and galaxies with $n < 2.5$ and $B/T < 0.5$.

Galaxies with $n \geq 2.5$ and $B/T \geq 0.5$ are typically elliptical galaxies, but due to the nature of the emission line galaxies observed in the MOSDEF survey, we do not expect to find these galaxies in the sample. Compact galaxies or galaxies containing active galactic nuclei (AGN) could cause a high n as well as a high B/T. Of the 26 galaxies found with $n \geq 2.5$ and $B/T \geq 0.5$, we find that 5 are AGN candidates as classified by their IR and X-ray properties, although one additional galaxy is an optical AGN candidate that lies above the Kewley et al. (2013) BPT classification line. This leaves 21 galaxies, which after visual inspection appear to be highly compact or low-surface brightness. Two of these parent sample galaxies do not have spectroscopic data, and 10 of the remaining galaxies have Hα dust-corrected SFR measurements. Stellar masses of these high Sérsic index and high B/T galaxies range from $9.59 \leq log(M_*/M_\odot) \leq 11.24$ with $7.46 \leq \mathrm{SFR(H}\alpha)_{corr} \leq 131.8\ M_\odot \mathrm{yr}^{-1}$. We also look at the 20 galaxies with $n \geq 2.5$ but with $B/T < 0.5$. By visual inspection, these galaxies appear to be interesting morphologies containing a bright central, compact component with a surrounding low surface brightness distribution. Some of these galaxies are rather irregular in nature, mergers, and two even contain low surface brightness spiral features surrounding the bright central core. We find that only one of these galaxies is an AGN candidate, and instead this high Sérsic index, low B/T morphology is caused by a bright, compact central bulge.

Overall we find that 148 of the 194 galaxies (76.3%) of the MOSDEF galaxies have rest-frame

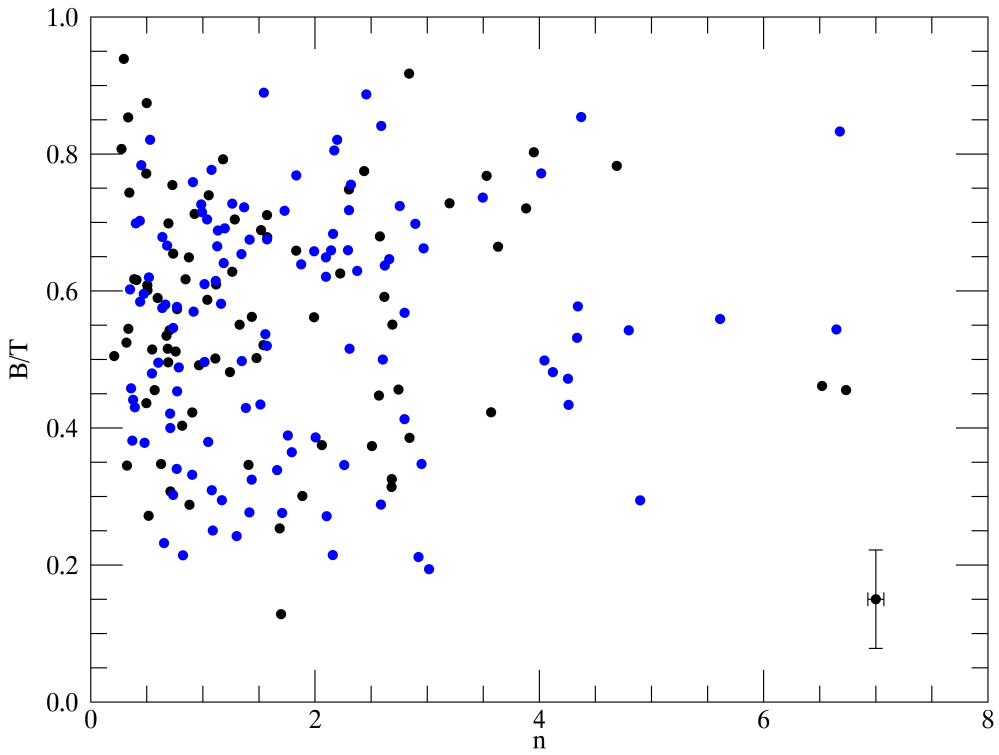

Figure 5.6: Rest-frame B-band B/T vs. galaxy Sérsic index for the sample of 194 galaxies with reliable single-component and two-component fits in the five fields observed in the MOSDEF survey. We separate the $1.37 \leq z \leq 1.70$ sample (black) and the $2.09 \leq z \leq 2.61$ sample (blue), taking morphologies measured in J-band and H-band, respectively, to achieve rest-frame optical. In the lower left, we show the average errors in each measurement.

optical disk-like Sérsic indices with a wide range of B/T ($0.12 \leq B/T \leq 0.94$). Disk galaxies can have a variety of bulge fractions depending on the Hubble type of the galaxy (Hubble, 1926). Galaxies with larger B/T have a strong bulge component such as Hubble Type Sa/Sab/Sb galaxies, while galaxies with larger disk contribution have a much weaker bulge and are more like Hubble Type Sc/Scd/Sd galaxies. In Figure 5.4, we show examples of these various types of disk galaxies in the MOSDEF star-forming galaxy sample.

Another important analysis is how the measured galaxy morphology depends on wavelength as well as how it compares to other galaxy properties such as stellar mass, SFR, and metallicity.

In Sections 5.3.3 and 5.3.4 we investigate how rest-frame optical morphology compares to other galaxy properties, while in section 5.3.2, we investigate how parameters such as size, Sérsic index and B/T depend on wavelength.

5.3.2 Multi-wavelength Dependence and Evolution

One of the most beneficial aspects of today's large legacy surveys, is the multi-wavelength data that is available. For our samples, we have observational data ranging from optical to infrared, which allows us to study rest-frame optical and ultraviolet as well as to try to understand how morphological properties depend on wavelength and evolves across cosmological timescales. In this section, we investigate how the sizes, r_e, and morphologies, n and B/T, vary with observed wavelength. We also separate the samples in to the two redshift bins, $1.37 \leq z \leq 1.70$ and $2.09 \leq z \leq 2.61$, to see if this changes with time. For this analysis, we take the MOSDEF parent samples described in Section 5.2, and select the galaxies with reliable morphology measurements for both a single component Sérsic fit and a two-component bulge-disk decomposition in the observed HST band that the 5 fields have in common: F160W, F125W, F814W/F775W, and F606W (H-, J-, i-, and v-band, respectively). For the COSMOS, AEGIS, and UDS fields F814W was observed, while ancillary HST ACS data for GOODS-N and GOODS-S provides F775W for those fields. Here we analyze the morphological parameters of the 195 $z \sim 1.5$ galaxies and 76 $z \sim 2.3$ galaxies.

Multi-wavelength n and B/T Measurements

In previous studies, the longest observed wavelength was typically used to analyze the morphology of galaxies across a wide redshift range (Wuyts et al., 2011; Lang et al., 2014; Bruce et al., 2012). Throughout this paper, we have applied a morphological k-correction to compare galaxy morphologies at the same rest-frame wavelength. Different rest-frame wavelengths will sample different galaxy populations, implying the importance of a morphological k-correction to ensure we are comparing the properties of the same stellar populations.

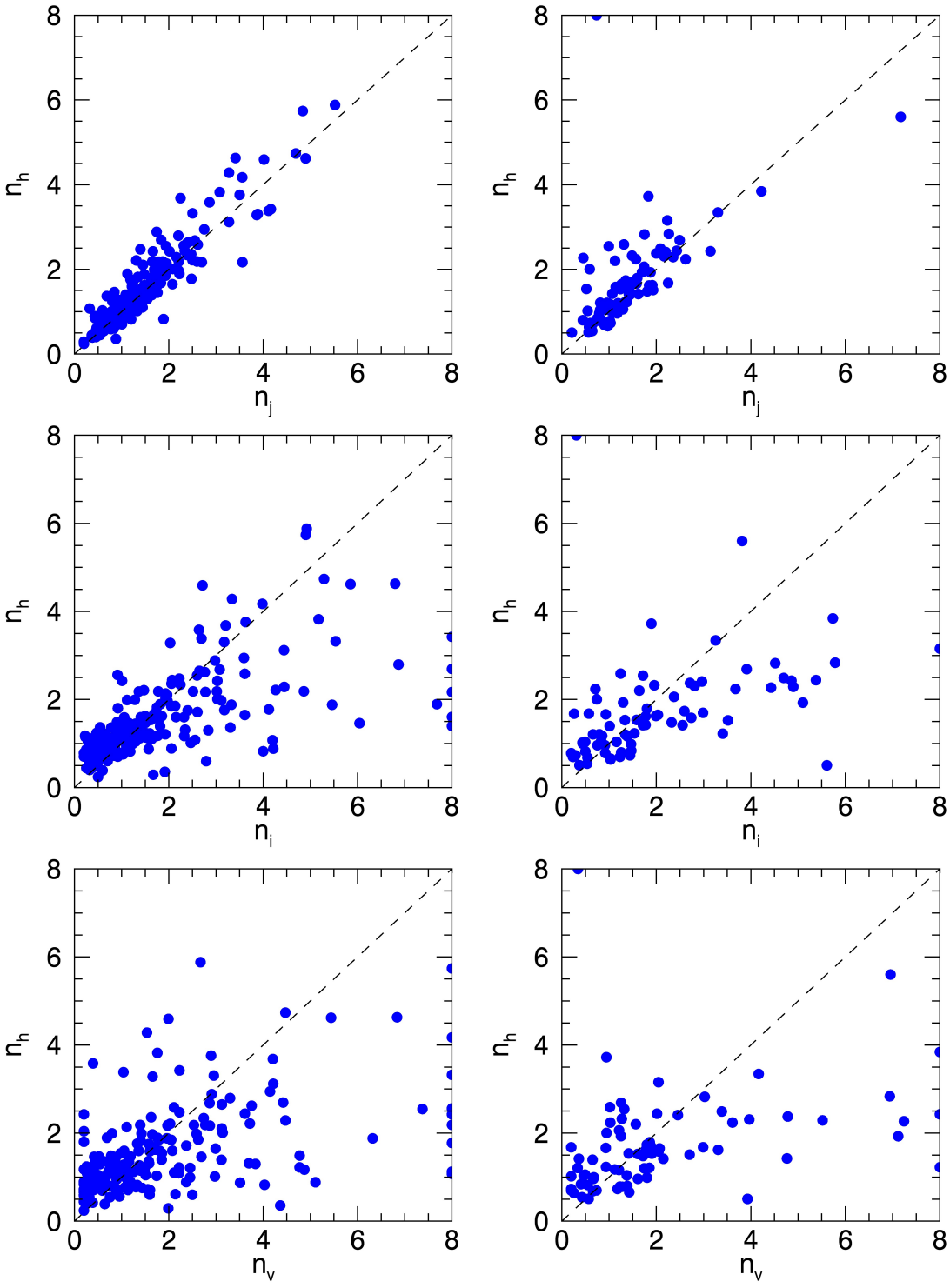

Figure 5.7: Measured H-band galaxy Sérsic index, n, compared to n measured in WFC3 J-band and ACS v- and i-band (Left, middle and right, respectively). Indices were obtained through single Sérsic profile fits to the parent sample galaxies, and the results are shown for two different redshift bins, $1.37 \leq z \leq 1.70$ (top) and $2.09 \leq z \leq 2.61$ (bottom).

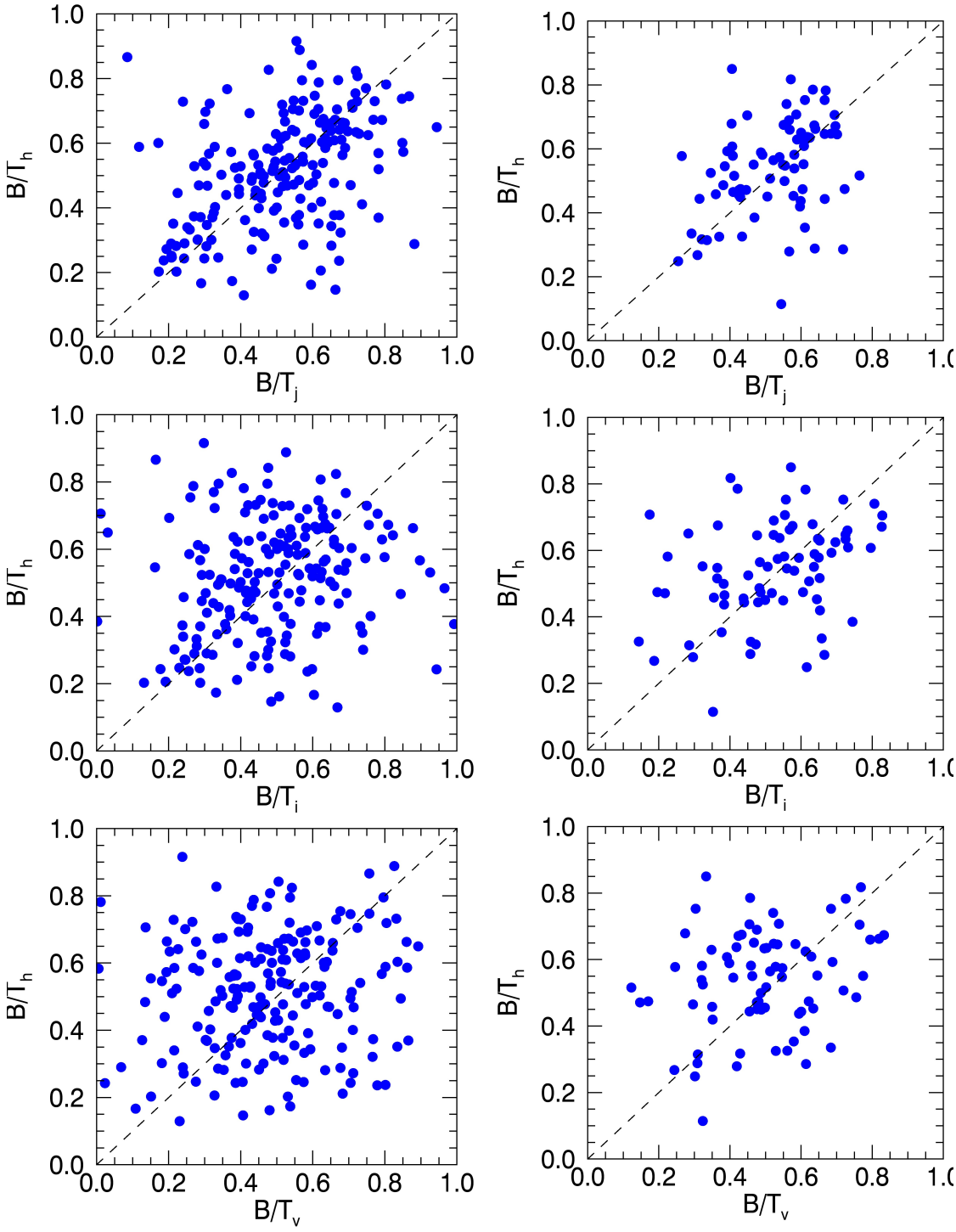

Figure 5.8: Measured H-band bulge-to-total flux ratio, B/T, compared to B/T measured in WFC3 J-band and ACS v- and i-band (Left, middle and right, respectively). Ratios were obtained through two component models with a Sérsic bulge profile and an exponential disk to the parent sample galaxies, and the results are shown for two different redshift bins, $1.37 \leq z \leq 1.70$ (top) and $2.09 \leq z \leq 2.61$ (bottom).

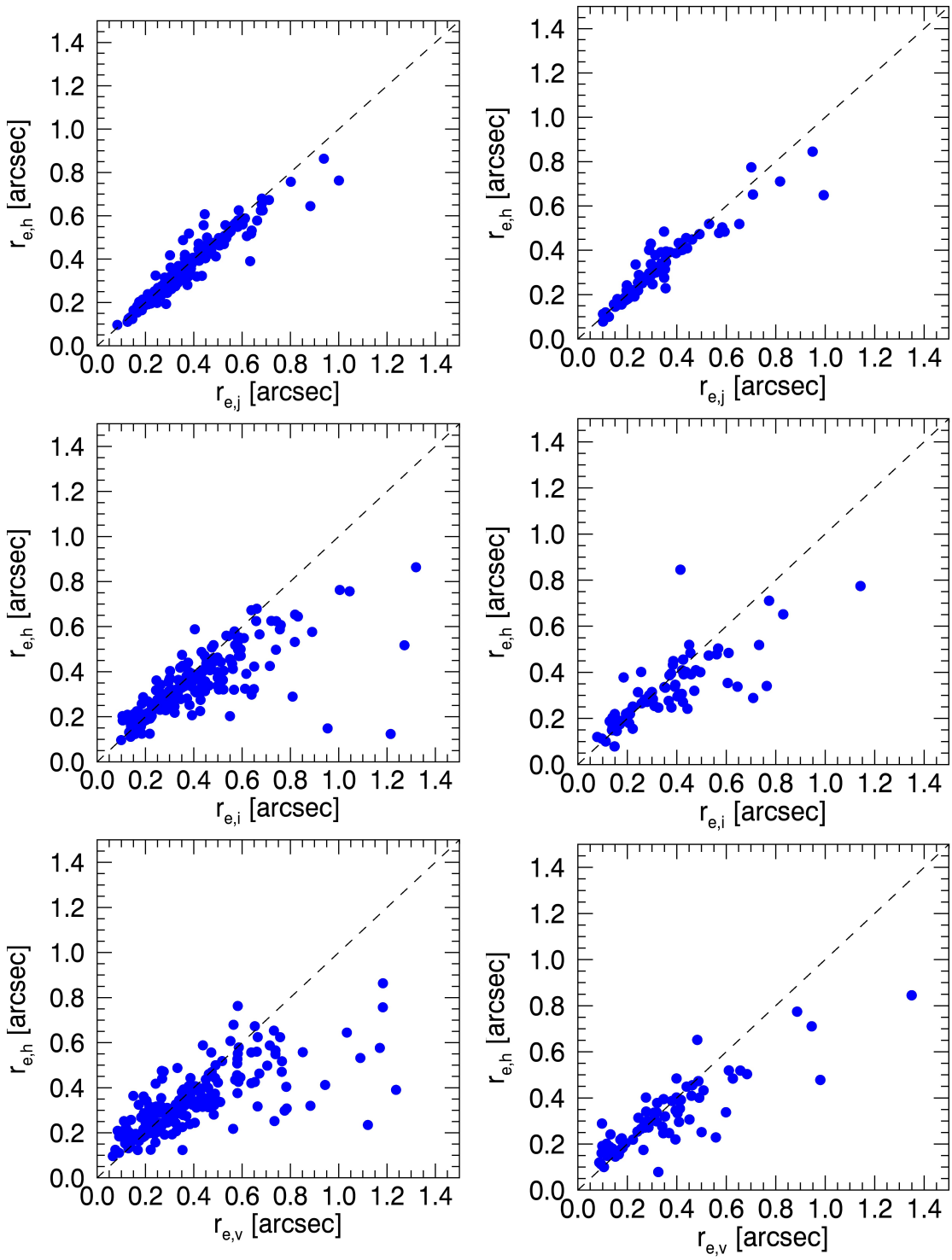

Figure 5.9: Measured H-band effective radius, r_e, compared to r_e measured in WFC3 J-band and ACS v- and i-band (Left, middle and right, respectively). Sizes were obtained through single Sérsic profile fits to the parent sample galaxies, and the results are shown for two different redshift bins, $1.37 \leq z \leq 1.70$ (top) and $2.09 \leq z \leq 2.61$ (bottom).

We investigate the dependence of morphological parameters on observed wavelength to determine if a morphological *k*-correction is necessary. In Figure 5.7 and 5.8, we show galaxy n and B/T measurements in H-band compared to the three other bands, J, i, and v (left to right) for the two different redshift bins, $1.37 \leq z \leq 1.70$ (top) and $2.09 \leq z \leq 2.61$ (bottom). We show the one-to-one correlation with the H-band morphology measurements with the dashed black line.

For galaxies with $1.37 \leq z \leq 1.70$, we see no dependence on the measured galaxy n between HST WFC3 H and J values, and the values seem to be overall in agreement with one another. However, when we look at the shorter, optical wavelengths, many galaxies have a measured n greater than what was found in H-band. The lower Sérsic index galaxies are mostly in agreement, but the scatter with respect to the one-to-one line is much greater in shorter wavelengths. For the $z \sim 2.3$ galaxies, we observe a similar trend but with less scatter in that the H- and J-band, infrared morphologies are mostly in agreement. The low n galaxies have more agreement in the shorter wavelengths, but higher n galaxies have even higher values measured in i and v, but with less scatter than the lower redshift galaxies. The comparison of B/T shows a lot of scatter in the measurements across all wavelengths. We observe no trend in B/T when compared to H-band, but different B/T values could be found depending on what wavelength is used to measure morphology.

Multi-wavelength Galaxy Size, r_e, Measurements

Another useful property that results from galaxy morphology measurements is the size, given by the effective radius r_e, of the galaxy. We investigate the size measurement of the galaxy sample and its dependence on redshift and wavelength. Figure 5.9 shows the HST WFC3 H-band r_e of each galaxy compared to the measured r_e in J-,i-, and v-band for the two different redshift bins. For galaxies with $1.37 \leq z \leq 1.70$, we find that the galaxy size correlates very well one-to-one between H and J, similar to the results of galaxy n across wavelengths. As we go to shorter wavelengths, we see more scatter in the larger sizes and find that galaxy sizes measure larger in v and i when compared to H. The $2.09 \leq z \leq 2.61$ galaxies show a very similar trend, but with

less scatter. This decreased scatter could be due to the smaller sample size. Overall we find that a morphological k-correction should be applied to compare same galaxy properties, due to the different in morphology measurements in n, B/T, and r_e.

5.3.3 Structural Main Sequence Analysis

We combine the star-forming main sequence sample, selection described in 5.2.2, and the morphology sample, 5.2.4, resulting in a final sample of 94 galaxies with Hα dust-corrected SFRs, mass measurements, and morphological measurements of galaxy Sérsic index and B/T. We summarize the results in Table 5.1 including both the observed scatter and intrinsic scatter. These measurements were calculated using the description in Shivaei et al. (2015). The intrinsic scatter takes into consideration the errors in both the mass and SFR measurements, but still includes galaxy-to-galaxy variations in the dust corrections. In Figure 5.10, we show the SFR-M_* relation as a function of their morphology. On the left, we have separated the Sérsic index morphological classification into three separate bins ($n < 1.0, 1.0 \leq n < 2.5$, and $2.5 \leq n \leq 5.0$). We find no galaxies in the sample with $n > 5.0$. The circles indicate galaxies in the redshift bin $2.09 \leq z \leq 2.61$, while the plus signs indicate galaxies with $1.37 \leq z \leq 1.70$. Overall we still see a significant scatter across the two n bins that are indicative of disk galaxies ($n < 2.5$), and no obvious correlation. We observe a smaller scatter in the $n < 1.0$ sample than the $1.0 \leq n < 2.5$ sample, as summarized in Table 5.1, but a significant scatter is still present for both. While this is a much smaller sample of very accurately measured Hα dust-corrected SFRs, when compared with the results of Wuyts et al. (2011), we find some agreement for high n gaalxies. In the study, they found a clearly present "structural main sequence" from $0.02 < z < 2.5$, but with a much larger sample. The galaxies they found with higher Sérsic indices, $n \sim 4$, were located towards the tip and upper envelope of the main sequence (MS), as well as in the quiescent zone below the MS, suggesting they could be intermediate, cuspy galaxies transitioning from star-forming to red and dead systems. Our results, using a smaller sample containing very few high Sérsic index galaxies, but we do observe many of these galaxies lying on the upper envelope as

well as one positioned close to the quiescent zone. These galaxies may be at the end of their star-formation and transitioning to quiescence.

While we find some cuspy, elliptical type galaxies along the upper edge of the SFR-M_* trend, we find many close to the linear regression where we expect only disk-like, star-forming galaxies with $n < 2..5$. We find 14 of the 94 galaxies (15%) have high Sérsic indices indicative of an elliptical type galaxy. AGN have already been removed from the sample, which could have caused a misclassification of a high n, so after visual inspection we find that these are compact or low surface brightness galaxies which would return a high Sérsic index. Compact, star-forming galaxies, such as these $n \geq 2.5$ galaxies found along the MS, have been found in other studies to be progenitors of the first quiescent galaxies at $z \sim 2$ (Barro et al., 2014). These galaxies could be transitioning to quiescence, quenching star formation due to the compact nature, which occurs before they lose their gas and dust. On the right of Figure 5.10, we show the SFR-M_* relation dependence on galaxy B/T. We observe that galaxies with $B/T \geq 0.5$ show a similar scatter as the entire MOSDEF sample of galaxies discussed in Section 5.2.2, but they have a shallower slope than the entire sample. We also observe a different relation with a smaller scatter for galaxies with $B/T < 0.5$. We separate these two populations of galaxies and include a linear best-fit line to the data in Figure 5.11. The galaxies with $B/T < 0.5$ have a much steeper slope of 1.22 ± 0.15 in the SFR-M_* plane, indicating that higher mass disk-dominated systems have a greater SFR than the average star-forming population. At lower mass, the large scatter in the $B/T \geq 0.5$ sample, 0.34 compared to 0.23 for $B/T < 0.5$, along with the $B/T < 0.5$ galaxies shows that SFR is primarily mass dependent at the low mass end. We summarize the slopes found for the SFR-M_* relations for the separate galaxy populations in Table 5.1, although due to the lower number of galaxies with $n \geq 2.5$, those quantities suffer from small number statistics and may be unreliable.

5.3.4 Structural MZR Analysis

We combine the MZR sample described in 5.2.3 with the morphology sample resulting in a final sample of 62 galaxies with reliable rest-frame optical morphology measurements and accurate

Table 5.1: Parameters of the log(SFR) - log(M_*) Linear Fit

Redshift Range	Sample[a]	N_{gal}[b]	Slope	Intercept	Observed Scatter	Intrinsic Scatter
$z = 1.37 - 2.61$	Full MOSDEF	181	0.74 ± 0.08	-6.21 ± 0.78	0.41	0.37
	Morphology Selected	82	0.77 ± 0.11	-6.45 ± 1.15	0.37	0.32
	$n \geq 2.5$	14	0.56 ± 0.37	-4.11 ± 3.69	0.37	0.31
	$n < 2.5$	68	0.82 ± 0.11	-6.94 ± 1.12	0.36	0.31
	$B/T \geq 0.5$	48	0.61 ± 0.13	-4.87 ± 1.34	0.40	0.34
	$B/T < 0.5$	34	1.22 ± 0.15	-11.00 ± 1.55	0.31	0.23
$z = 2.09 - 2.61$	Full MOSDEF	123	0.61 ± 0.10	-4.74 ± 0.97	0.39	0.33
	Morphology Selected	57	0.64 ± 0.15	-5.03 ± 1.54	0.37	0.31
	$n \geq 2.5$	13	0.57 ± 0.37	-4.24 ± 3.64	0.38	0.32
	$n < 2.5$	44	0.66 ± 0.16	-5.31 ± 1.57	0.36	0.31
	$B/T \geq 0.5$	32	0.44 ± 0.17	-3.00 ± 1.73	0.40	0.34
	$B/T < 0.5$	25	1.16 ± 0.17	-10.32 ± 1.71	0.29	0.21
$z = 1.37 - 2.61$	Shivaei et al. 2015[c]	185	0.65 ± 0.09	-5.42 ± 0.88	0.40	0.36
$z = 2.09 - 2.61$	Shivaei et al. 2015[c]	128	0.59 ± 0.11	-4.68 ± 1.06	0.36	0.31

[a] Parameters are calculated for galaxies with $M_* > 10^{9.5}$ $M_\odot$
[b] Number of objects.
[c] Different mass estimates. Please see Shivaei et al. (2015) for details.

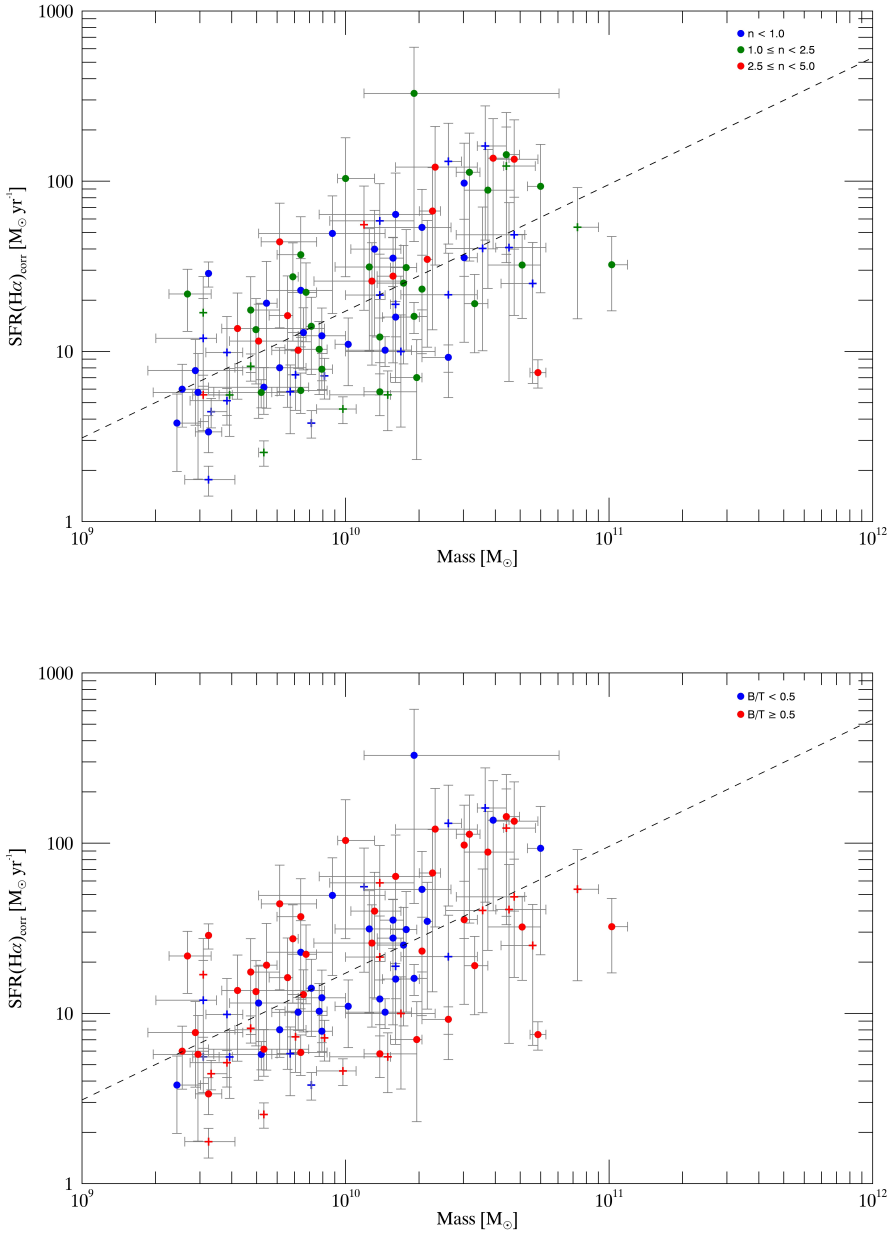

Figure 5.10: SFR-M_* relation for $1.37 \leq z \leq 1.70$ and $2.09 \leq z \leq 2.61$ star-forming galaxies with 3σ significance Hα and Hβ measurements. Quiescent galaxies have been removed and only those with corrected SFR are shown. We show the galaxy Sérsic index (left) for the galaxies on the left color-coded for galaxies with $n < 1.0$, $1.0 \leq n < 2.5$, and $n \geq 2.5$. We also show the measured B/T fraction (right) with galaxies havig $B/T < 0.5$ in blue and $B/T \geq 0.5$ in red. Additionally we distinguish between the $1.37 \leq z \leq 1.70$ sample (plus) and the $2.09 \leq z \leq 2.61$ sample (circles).

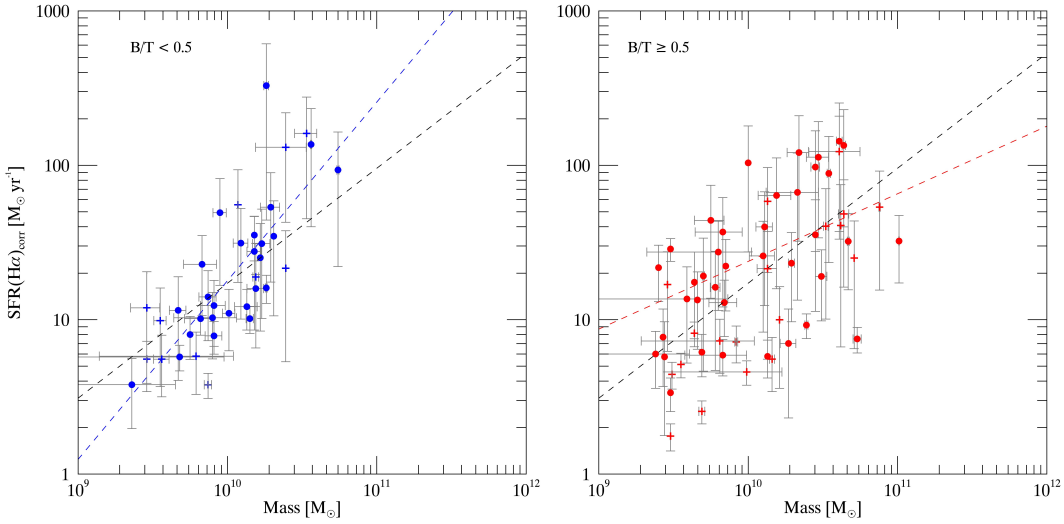

Figure 5.11: SFR-M$_*$ relation for $1.37 \leq z \leq 1.70$ and $2.09 \leq z \leq 2.61$ star-forming galaxies with 3σ significance Hα and Hβ measurements. Quiescent galaxies have been removed and only those with corrected SFR are shown. We show the B/T morphological dependence of the galaxies by separating $B/T < 0.5$ (left) and $B/T \geq 0.5$ (right). The best-fit linear line to the entire MOSDEF sample is shown by the black dashed line, while the linear fit to the separate morphological populations is shown by the blue dashed line for galaxies with $B/T < 0.5$ (left) and by the red dashed line for galaxies with $B/T \geq 0.5$ (right).

metallicity and mass measurements. Of these 62 galaxies, 39 have 3σ detections in Hα, [NII] λ6584, Hβ, and [OIII] λ5007, while 23 are upper limits, where [NII] λ6584 was not detected. We first investigate the MZR dependence on galaxy Sérsic index in Figure 5.12.

We find a small dependence of the MZR on the Sersic index using either N2 or O3N2 indicators. We find 8 N2 detection galaxies and 4 upper limit galaxies with $n \geq 2.5$, which are not be expected in a star-forming sample. These galaxies lie close to the Steidel et al. (2014) linear fit when using the O3N2 indicator, but show a large scatter when using the N2 indicator. After visual inspection, we find that they are compact or low surface brightness galaxies, just like those described in Section 5.3.3. The largest sample of galaxies with N2 detections have $1.0 \leq n < 2.5$, which span the whole range of the MZR with little correlation. We also see no correlation between galaxy n and MZR for galaxies with $n < 1.0$. Overall, the observed MZR seems to have no dependence on the galaxy Sérsic index.

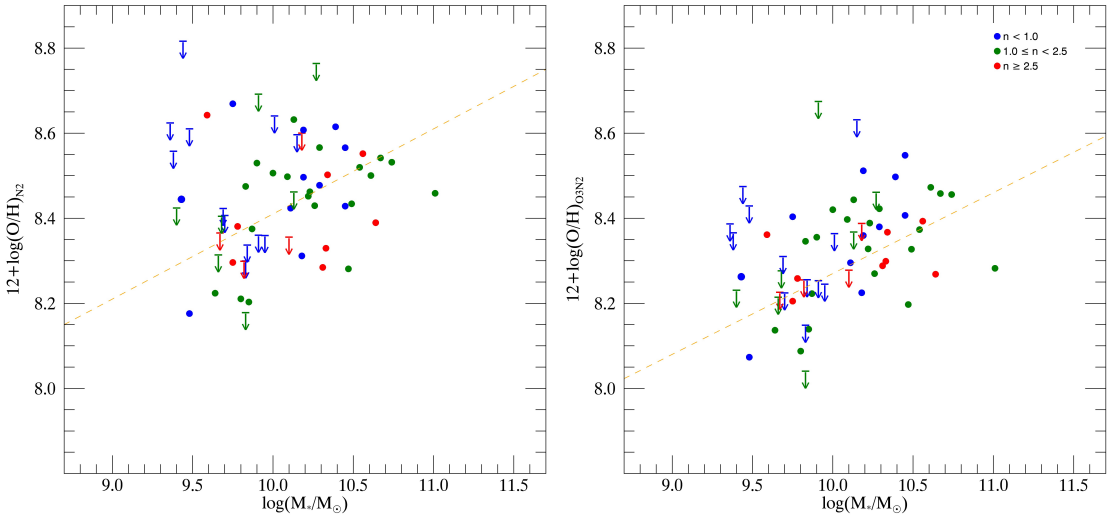

Figure 5.12: MZR for $z \sim 2.3$ star-forming galaxies with metallicities determined using N2 (left) and O3N2 (right) indicators with rest-frame optical morphology measurements. Circles indicate MOSDEF galaxies with 3σ or greater significance in Hα, Hβ, and [OIII] λ5007. Arrows indicate 3σ upper limits where [NII] λ6584 was not detected. Galaxies are color-coded based on their rest-frame optical morphology. Red points indicate galaxies with Sérsic index, $n \geq 2.5$, while blue points are galaxies with $n < 2.5$. The orange dashed line is the best-fit line to the $z \sim 2.3$ N2 and O3N2 MZR as observed by Steidel et al. (2014).

Next we investigate if there is a correlation between the observed MZR at $z \sim 2.3$ in the MOSDEF survey, and the measured B/T. We find a large fraction of the galaxies (66.7% of detected, 47.8% of upper limits) with $B/T \geq 0.5$. Of these 37 galaxies, we find that 7 (18.9%) also have $n \geq 2.5$, and are the compact galaxies determined by visual inspection. These star-forming galaxies that follow the MZR with compact, high n and B/T morphologies have a median SFR of 45.0 $M_{\odot}$ yr^{-1} indicating that these are not quiescent galaxies, but instead compact and highly star-forming, perhaps also similar to those found by Barro et al. (2014), which may be galaxies transitioning to quiescence. Disk galaxies with varying degree of bulge fraction are scattered along the entire MZR, with no apparent relation, however there is a larger population of high B/T galaxies at the high mass end, suggesting that high mass galaxies with higher metallicity have larger bulge fractions, indicating that metallicity builds up in the bulge of galaxies.

We also measured effective radii, r_e of MOSDEF galaxies, and investigate size dependence

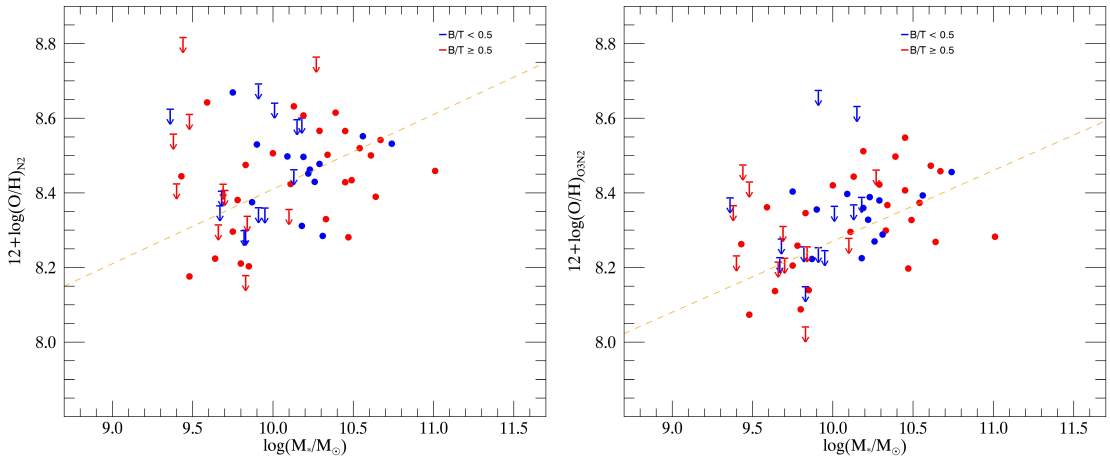

Figure 5.13: MZR for $z \sim 2.3$ star-forming galaxies with metallicities determined using N2 (left) and O3N2 (right) indicators with rest-frame optical morphology measurements. Circles indicate MOSDEF galaxies with 3σ or greater significance in Hα, Hβ, and [OIII] λ5007. Arrows indicate 3σ upper limits where [NII] λ6584 was not detected. Galaxies are color-coded based on their rest-frame optical morphology. Red points indicate galaxies with bulge-to-total flux ratio, $B/T \geq 0.5$, while blue points are galaxies with $B/T < 0.5$. The orange dashed line is the best-fit line to the $z \sim 2.3$ N2 and O3N2 MZR as observed by Steidel et al. (2014).

of the MZR in Figure 5.14. We see a trend of increasing size with increasing metallicity and stellar mass for galaxies with N2 detections. While there is some scatter in the relation, we do see an overall size dependence of the MZR even with this small sample size. We summarize the average values for the different morphological properties in 4 different mass bins in Table 5.2 as well as median value for SFR for the mass bin.

5.4 Conclusions and Discussion

In this chapter, we have used observations from the MOSDEF survey to investigate the morphology of the spectroscopically observed sample as well as how these measurements correlate with other galaxy properties including stellar mass, SFR, and metallicity. Objects were selected from the *H*-band selected parent catalog, which was derived from the 3D-HST survey, and morphology was measured using both a single Sérsic component fit as well as a two-component bulge-disk decomposition. After goodness of fit was determined and the parent catalog matched to ob-

Table 5.2: Galaxy properties for MZR relation

$\log\left(\frac{M_*}{M_\odot}\right)^a$	$\left\langle \log\left(\frac{M_*}{M_\odot}\right)\right\rangle^b$	N^c	$\langle r_e\rangle^d$ (kpc)	$\langle n\rangle^d$	$\langle B/T\rangle^d$	SFR$_{med}{}^e$ ($M_\odot$ yr^{-1})
N2 Detection Sample						
$9.43-9.86$	9.69	10	1.47	1.96	0.63	17.49
$9.86-10.22$	10.09	10	2.49	1.18	0.50	31.34
$10.23-10.46$	10.33	10	2.36	1.90	0.54	53.51
$10.46-11.01$	10.64	9	3.20	2.14	0.64	93.29

[a] Range of $\log(M_*/M_\odot)$ of galaxies in bin.
[b] Average $\log(M_*/M_\odot)$ of galaxies in bin.
[c] Number of objects.
[d] Average values of r_e, n, and B/T for galaxies in mass bin.
[e] Median dust-corrected Hα SFR of galaxies in bin.

jects targeted in the MOSDEF survey, we analyzed a sample of 194 galaxies with redshifts of $1.37 \leq z \leq 1.70$ and $2.09 \leq z \leq 2.61$.

We investigated the general morphology of 194 galaxies, and observe that these emission line galaxies have primarily disk-dominated Sérsic indices with a scatter in B/T. This indicates a variety of Hubble Type spiral galaxies with varying degree of bulge fraction. We do find $\sim 13\%$ of the galaxies have cuspy, elliptical-like Sérsic indices and high B/T, which are primarily compact or low surface brightness galaxies. This morphology is unexpected for star-forming galaxies, and we investigated if the morphological classifications could be caused by the presence of AGN. Only 5 of the 26 galaxies were found to contain an AGN candidate, leaving 21 galaxies with a compact, star-forming morphology indicating that compact, elliptical type galaxies at higher redshift, ($1.37 \leq z \leq 1.70$ and $2.09 \leq z \leq 2.61$) have some remaining star-formation, and have not yet evolved into quiescent galaxies. Galaxies found to have high Sérsic index and disk-dominated B/T, are primarily irregular galaxies or galaxies with a bright central bulge component, producing a more cuspy surface brightness profile.

A key importance of our study is that we apply a morphological k-correction to compare the same rest-frame morphology measurements of the galaxy sample. Previous studies have completed and analyzed morphology in the longest, observed wavelength available, and we investigated the wavelength dependence to determine if a morphological k-correction is neces-

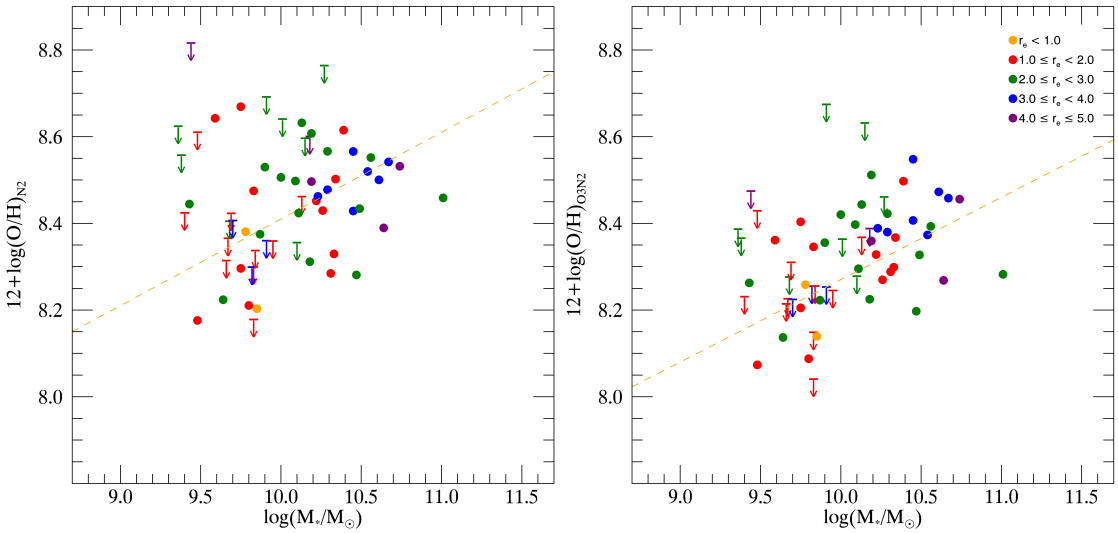

Figure 5.14: MZR for $z \sim 2.3$ star-forming galaxies with metallicities determined using N2 (left) and O3N2 (right) indicators with rest-frame optical morphology measurements. Circles indicate MOSDEF galaxies with 3σ or greater significance in Hα, Hβ, and [OIII] λ5007. Arrows indicate 3σ upper limits where [NII] λ6584 was not detected. Galaxies are color-coded based on their sizes taken from their rest-frame optical morphology. Galaxies are color-coded based on 5 different size bins: $r_e < 1.0$ kpc (orange), $1.0 \leq r_e < 2.0$ kpc (red), $2.0 \leq r_e < 3.0$ kpc (green), $3.0 \leq r_e < 4.0$ kpc (blue), $4.0 \leq r_e \leq 5.0$ kpc (purple). The orange dashed line is the best-fit line to the $z \sim 2.3$ N2 and O3N2 MZR as observed by Steidel et al. (2014)

sary to implement. We observed very little dependence between the two IR wavelengths used in this study, WFC3 IR F160W and F125W, however we do observe a larger Sérsic index and r_e for galaxies observed in shorter wavelengths indicating that when quantifying morphology over a large redshift range, a morphological k-correction should always be implemented. Different wavelengths of light will investigate different stellar populations, and it is important to compare the morphology of the same galaxy properties. However, we observe no dependence of B/T across wavelengths due to the large scatter in this property. This could possibly be attributed to the larger error in the measurement due to the large amount of free parameters in the parametric fitting.

Another important aspect of our study is how galaxy morphology relates to other spectroscopically measured galaxy properties including SFR, stellar mass, and metallicity. We find no

correlation between the galaxy Sérsic index for the star-forming galaxies on the SFR-M_* relation, otherwise known as the star-forming main sequence. A significant scatter, similar to the overall galaxy sample, is observed for the different morphological populations. However, when we studied the B/T dependence of the relation we found that galaxies with disk-dominated B/T follow a stepper linear relation with less scatter than the overall galaxy sample, while galaxies with high B/T follow closer to the same linear relation as the total sample. This shows that later-type spiral galaxies with low bulge fractions have higher dust-correct SFR with increasing mass than those with large bulge fractions. This could suggest that as mass increases and galaxies evolve towards quiescence, the bulge fraction increases with decreasing SFR leading to the evolution into early-type galaxies. However, at the lower mass end of the relation, the SFR becomes dependence on the overall galaxy mass as opposed to the overall galaxy morphology. In our study of the morphological dependence of the MZR, we find no apparent relation between galaxy Sérsic index and measured B/T with a large scatter throughout the relation. However, we do find a size dependence for the relation showing that lower mass galaxies with lower metallicity are typically smaller than the high mass, high Z end of the relation.

In conclusion, we emphasize that through robust measurements of galaxy properties including SFR and metallicity, galaxy evolution can be further understood while implementing a morphological k-correction. In order to truly understand how the morphological properties of a galaxy sample, including n, B/T, and r_e, evolve with time and correlate with galactic properties the morphology should be compared in the same rest-frame wavelength to ensure comparison of similar stellar populations.

Chapter 6

Summary and Conclusions

Summary of Morphological Technique

Throughout this work, I measure parametric galaxy morphology using GALFIT. In order to do this, I have developed my own code that extracts postage stamps to enclose all of the galaxy light as well as background sky pixels, take into account other galaxies within the postage stamp and either masks them out or fits them simultaneously, as well as measure the background sky value using a flux-growth method. All of these aspects are then taken into consideration as I execute GALFIT on the galaxy samples completing single Sérsic fits to the overall galaxy surface brightness profiles, as well as completing two-component bulge-disk decompositions using a Sérsic function to describe the bulge component of the galaxy and exponential disk. Goodness of fit is taken into consideration by investigating errors and the reduced χ^2 value from GALFIT, resulting in morphology measurements of the galaxy Sérsic index n, the galaxy size given by the effective radius r_e, and the bulge-to-total flux ratio B/T.

Parametric vs. Non-Parametric Morphology Measurements

Many techniques have been developed to study and quantify galaxy morphology. While I use parametric measurements assuming an analytical model, non-parametric techniques are also useful in identifying galaxy types as well as irregularities in the surface brightness profiles. I

compared my Sérsic and bulge-disk fits to the measurements of the Gini coefficient and second-order moment of galaxy brightness, M_{20}, and found that overall the two methods agree on the morphological classification of the sample. Gini-M_{20} diagrams separate galaxies into three main classifications, bulge-dominated, disk-dominated, and irregular or merging systems, while the information gathered from fitting Sérsic profiles to galaxies results in Sérsic indices and B/T that separate galaxies into elliptical systems, and bulge- and disk-domainted spiral Hubble Type galaxies. By comparing the Gini-M_{20} diagram and the combination of galaxy n and B/T, I find agreement between morphological classifications.

Morphology of Star-Forming Galaxies

In Chapter 4, I investigated the rest-frame optical morphology of a sample of galaxies with MIPS 24 μm detection. These galaxies are typically star-forming galaxies due to the nature of 24 μm emission, and I found that the majority of the sample did have a Sérsic index indicative of this, with a wide range of bulge fractions. Once I removed galaxies with unreliable morphology measurements and with low axis ratios ($b/a < 0.3$) to eliminate edge-on galaxies, the overall MIPS sample consisted of 100 galaxies. Of this sample, 76% of the galaxies were found to be disk galaxies with varying bulge fractions indicative star forming galaxies. While 24 of the galaxies had galaxy Sérsic indices indicative of elliptical galaxies, only 9 of these galaxies also had bulge dominated B/T. The cause of MIPS 24 μm detection in these galaxies was determined to be AGN activity for 2 of the galaxies, and although the remaining 7 did not have X-ray detection indicative of an AGN candidate, they could still contain an obscured AGN causing the 24 μm emission. I also studied control sample of galaxies, selected in the same manner but without 24 μm detection. I find that they also have a large fraction of disk-dominated galaxies, but also contained 49 (of the 226 galaxies) with large n indicative of elliptical galaxies. A large fraction of these galaxies (63%) also had bulge dominated B/T, with only 2 containing an AGN candidate. For galaxies in the MIPS and control sample to be found with high Sérsic indices and low B/T, it was found that these galaxies have morphologies of transitional Hubble Types, perhaps in the stage between ellipticals and disks. These galaxies had large central point sources with lower

surface brightness extended features, showing that the combination of the two morphology indicators make for a better galaxy type classification.

In Chapter 5, I analyzed the galaxies observed in the MOSDEF survey. These primarily emission line galaxies are mostly star-forming, and I find 76.3% of the sample to have Sérsic indices indicative of a disk galaxy. These low n galaxies ($n < 2.5$) have a wide range of B/T showing a wide variety of bulge fractions and therefore spanning the whole range of Hubble Type spiral galaxies. I find 46 of the galaxies (23.7%) of these galaxies have $n \geq 2.5$, with 26 of these galaxies also having bulge dominated B/T. Only 5 of these galaxies were found to be AGN candidates, and the remaining were found to be compact or low surface brightness galaxies after visual inspection.

Morphology Wavelength Dependence

Throughout this work, we have selected the observed wavelength of the galaxy morphology to correspond to rest-frame optical measurements. This applies a morphological k-correction to be sure that I compare the same stellar populations and therefore morphology of the objects. To determine if this correction is necessary, I compared the measured n, B/T and galaxy size r_e in the common wavelengths available in all five fields of the MOSDEF survey. For observed wavelengths that are fairly close, such as HST WFC3 H and J, I found very little variation in the measured morphological parameters. However, when comparing HST WFC3 H and HST ACS v or i, we find some agreement for low n values, but beyond $n \sim 2$ shorter wavelength measurements are typically found to be larger than the H-band measurements. For B/T, there was a large scatter in all wavelengths compared to H, and results for the size r_e followed the same trend as n. Overall, I found that applying a morphological k-correction is important in comparing galaxies across different redshifts.

Structural Star-Forming Main Sequence

The morphological dependence of the SFR-M_* relation, also known as the star-forming main sequence, was investigated in Chapter 5. The relation was first studied in Shivaei et al. (2015),

and I further investigated n or B/T dependence. I found no correlation with the galaxy n, seeing as only star-forming galaxies were present, but did find high n galaxies along the linear best-fit line, opposite of the results of Wuyts et al. (2011). Theses galaxies were compact galaxies with a range of dust-correct SFR, but due to their compact nature the morphology of these galaxies is difficult to understand. However, when the correlation between the measured B/T and the SFR-M_* relation was investigated, we found that galaxies with lower B/T (< 0.5) followed a steeper linear relation with less scatter than the bulge-dominated galaxies or the sample as a whole. This indicates that high mass galaxies with small bulge fractions have higher SFR. These galaxies would be primarily late-type disk galaxies with high star formation in the spirals features.

Morphological Dependence of the Mass-Metallicity Relation at $z \sim 2.3$

The mass-metallicity relation has long been studied out to $z \sim 3.5$, and the MOSDEF survey has investigated this relation at $z \sim 2.3$ for the first season's data (Sanders et al., 2015). Understanding the morphological dependence of galaxies along the relation could aid in understanding galaxy formation and evolution scenarios. In Chapter 5, a large scatter was found along the relation for measured n and B/T indicating no morphological dependence. I also investigated a size dependence of the galaxies along the MZR and found that on average, smaller galaxies ($r_{e,ave} = 1.47$ kpc) occupy the low mass and low metallicity end of the MZR, while the larger galaxies of the sample ($r_{e,ave} = 3.20$ kpc) were found to have higher mass and metallicity measurements. While morphology parameters of Sérsic index and B/T show no correlation with the MZR, we do find that the relation is size dependent.

Limitations

The primary limitations of the work described in this dissertation are related to the small sample sizes used in the analyses. With improvements in success rate for reliable morphology measurements, and larger samples of galaxies with more elliptical or quiescent galaxies would improve the overall morphological comparison.

References

Abraham, R. G., van den Bergh, S., Glazebrook, K., Ellis, R. S., Santiago, B. X., Surma, P., and Griffiths, R. E.: 1996, *ApJl Supp.* **107**, 1

Abraham, R. G., van den Bergh, S., and Nair, P.: 2003, *ApJ* **588**, 218

Andredakis, Y. C., Peletier, R. F., and Balcells, M.: 1995, *MNRAS* **275**, 874

Andredakis, Y. C. and Sanders, R. H.: 1994, *MNRAS* **267**, 283

Andrews, B. H. and Martini, P.: 2013, *ApJ* **765**, 140

Barden, M., Häußler, B., Peng, C. Y., McIntosh, D. H., and Guo, Y.: 2012, *MNRAS* **422**, 449

Barden, M., Rix, H.-W., Somerville, R. S., Bell, E. F., Häußler, B., Peng, C. Y., Borch, A., Beckwith, S. V. W., Caldwell, J. A. R., Heymans, C., Jahnke, K., Jogee, S., McIntosh, D. H., Meisenheimer, K., Sánchez, S. F., Wisotzki, L., and Wolf, C.: 2005, *ApJ* **635**, 959

Barro, G., Faber, S. M., Pérez-González, P. G., Pacifici, C., Trump, J. R., Koo, D. C., Wuyts, S., Guo, Y., Bell, E., Dekel, A., Porter, L., Primack, J., Ferguson, H., Ashby, M. L. N., Caputi, K., Ceverino, D., Croton, D., Fazio, G. G., Giavalisco, M., Hsu, L., Kocevski, D., Koekemoer, A., Kurczynski, P., Kollipara, P., Lee, J., McIntosh, D. H., McGrath, E., Moody, C., Somerville, R., Papovich, C., Salvato, M., Santini, P., Tal, T., van der Wel, A., Williams, C. C., Willner, S. P., and Zolotov, A.: 2014, *ApJ* **791**, 52

Bauer, A. E., Conselice, C. J., Pérez-González, P. G., Grützbauch, R., Bluck, A. F. L., Buitrago, F., and Mortlock, A.: 2011, *MNRAS* **417**, 289

Bershady, M. A., Jangren, A., and Conselice, C. J.: 2000, *The Astronomical Journal* **119**, 2645

Bertin, E. and Arnouts, S.: 1996, **117**, 393

Bond, N. A., Gawiser, E., and Koekemoer, A. M.: 2011, *ApJ* **729**, 48

Bouwens, R., Cayón, L., and Silk, J.: 1999, *ApJ* **516**, 77

Brinchmann, J., Abraham, R., Schade, D., Tresse, L., Ellis, R. S., Lilly, S., Le Fèvre, O., Glazebrook, K., Hammer, F., Colless, M., Crampton, D., and Broadhurst, T.: 1998, *ApJ* **499**, 112

Bruce, V. A., Dunlop, J. S., Cirasuolo, M., McLure, R. J., Targett, T. A., Bell, E. F., Croton, D. J., Dekel, A., Faber, S. M., Ferguson, H. C., Grogin, N. A., Kocevski, D. D., Koekemoer, A. M., Koo, D. C., Lai, K., Lotz, J. M., McGrath, E. J., Newman, J. A., and van der Wel, A.: 2012, *MNRAS* **427**, 1666

Calzetti, D., Armus, L., Bohlin, R. C., Kinney, A. L., Koornneef, J., and Storchi-Bergmann, T.: 2000, *ApJ* **533**, 682

Calzetti, D., Kennicutt, R. C., Engelbracht, C. W., Leitherer, C., Draine, B. T., Kewley, L., Moustakas, J., Sosey, M., Dale, D. A., Gordon, K. D., Helou, G. X., Hollenbach, D. J., Armus, L., Bendo, G., Bot, C., Buckalew, B., Jarrett, T., Li, A., Meyer, M., Murphy, E. J., Prescott, M., Regan, M. W., Rieke, G. H., Roussel, H., Sheth, K., Smith, J. D. T., Thornley, M. D., and Walter, F.: 2007, *ApJ* **666**, 870

Calzetti, D., Kennicutt, Jr., R. C., Bianchi, L., Thilker, D. A., Dale, D. A., Engelbracht, C. W., Leitherer, C., Meyer, M. J., Sosey, M. L., Mutchler, M., Regan, M. W., Thornley, M. D., Armus, L., Bendo, G. J., Boissier, S., Boselli, A., Draine, B. T., Gordon, K. D., Helou, G., Hollenbach, D. J., Kewley, L., Madore, B. F., Martin, D. C., Murphy, E. J., Rieke, G. H., Rieke, M. J., Roussel, H., Sheth, K., Smith, J. D., Walter, F., White, B. A., Yi, S., Scoville, N. Z., Polletta, M., and Lindler, D.: 2005, *ApJ* **633**, 871

Casey, C. M., Narayanan, D., and Cooray, A.: 2014, **541**, 45

Chabrier, G.: 2003, *Publications of the Astronomical Society of the Pacific* **115**, 763

Cibinel, A., Carollo, C. M., Lilly, S. J., Miniati, F., Silverman, J. D., van Gorkom, J. H., Cameron, E., Finoguenov, A., Norberg, P., Peng, Y., Pipino, A., and Rudick, C. S.: 2013, *ApJ* **776**, 72

Cirasuolo, M., McLure, R. J., Dunlop, J. S., Almaini, O., Foucaud, S., Smail, I., Sekiguchi, K., Simpson, C., Eales, S., Dye, S., Watson, M. G., Page, M. J., and Hirst, P.: 2007, *MNRAS* **380**, 585

Coil, A. L., Aird, J., Reddy, N., Shapley, A. E., Kriek, M., Siana, B., Mobasher, B., Freeman, W. R.,

Price, S. H., and Shivaei, I.: 2015, *ApJ* **801**, 35

Conroy, C., Gunn, J. E., and White, M.: 2009, *ApJ* **699**, 486

Conselice, C. J.: 2003, *ApJl Supp.* **147**, 1

Conselice, C. J.: 2014, *Annual Reviews of Astronomy and Astrophysics* **52**, 291

Conselice, C. J., Bershady, M. A., and Jangren, A.: 2000, *ApJ* **529**, 886

Conselice, C. J., Blackburne, J. A., and Papovich, C.: 2005, *ApJ* **620**, 564

Conselice, C. J., Chapman, S. C., and Windhorst, R. A.: 2003, *ApJl* **596**, L5

Dahlen, T., Mobasher, B., Dickinson, M., Ferguson, H. C., Giavalisco, M., Grogin, N. A., Guo, Y., Koekemoer, A., Lee, K.-S., Lee, S.-K., Nonino, M., Riess, A. G., and Salimbeni, S.: 2010, *ApJ* **724**, 425

Dahlen, T., Mobasher, B., Faber, S. M., Ferguson, H. C., Barro, G., Finkelstein, S. L., Finlator, K., Fontana, A., Gruetzbauch, R., Johnson, S., Pforr, J., Salvato, M., Wiklind, T., Wuyts, S., Acquaviva, V., Dickinson, M. E., Guo, Y., Huang, J., Huang, K.-H., Newman, J. A., Bell, E. F., Conselice, C. J., Galametz, A., Gawiser, E., Giavalisco, M., Grogin, N. A., Hathi, N., Kocevski, D., Koekemoer, A. M., Koo, D. C., Lee, K.-S., McGrath, E. J., Papovich, C., Peth, M., Ryan, R., Somerville, R., Weiner, B., and Wilson, G.: 2013, *ApJ* **775**, 93

Dale, D. A., Bendo, G. J., Engelbracht, C. W., Gordon, K. D., Regan, M. W., Armus, L., Cannon, J. M., Calzetti, D., Draine, B. T., Helou, G., Joseph, R. D., Kennicutt, R. C., Li, A., Murphy, E. J., Roussel, H., Walter, F., Hanson, H. M., Hollenbach, D. J., Jarrett, T. H., Kewley, L. J., Lamanna, C. A., Leitherer, C., Meyer, M. J., Rieke, G. H., Rieke, M. J., Sheth, K., Smith, J. D. T., and Thornley, M. D.: 2005, *ApJ* **633**, 857

Davis, M., Guhathakurta, P., Konidaris, N. P., Newman, J. A., Ashby, M. L. N., Biggs, A. D., Barmby, P., Bundy, K., Chapman, S. C., Coil, A. L., Conselice, C. J., Cooper, M. C., Croton, D. J., Eisenhardt, P. R. M., Ellis, R. S., Faber, S. M., Fang, T., Fazio, G. G., Georgakakis, A., Gerke, B. F., Goss, W. M., Gwyn, S., Harker, J., Hopkins, A. M., Huang, J.-S., Ivison, R. J., Kassin, S. A., Kirby, E. N., Koekemoer, A. M., Koo, D. C., Laird, E. S., Le Floc'h, E., Lin, L., Lotz, J. M., Marshall, P. J., Martin, D. C., Metevier, A. J., Moustakas, L. A., Nandra, K., Noeske, K. G., Papovich, C., Phillips, A. C., Rich, R. M., Rieke, G. H., Rigopoulou, D., Salim, S., Schiminovich, D., Simard, L., Smail, I., Small, T. A., Weiner, B. J., Willmer, C. N. A., Willner, S. P., Wilson, G., Wright, E. L., and Yan, R.: 2007, *ApJl* **660**, L1

de Jong, R. S.: 1996, **118**, 557

de Jong, R. S., Simard, L., Davies, R. L., Saglia, R. P., Burstein, D., Colless, M., McMahan, R., and Wegner, G.: 2004, *MNRAS* **355**, 1155

de Souza, R. E., Gadotti, D. A., and dos Anjos, S.: 2004, *ApJl Supp.* **153**, 411

de Vaucouleurs, G.: 1948, *Annales d'Astrophysique* **11**, 247

de Vaucouleurs, G.: 1953, *MNRAS* **113**, 134

de Vaucouleurs, G.: 1956, *Occasional Notes of the Royal Astronomical Society* **3**, 18

Dickinson, M., Giavalisco, M., and GOODS Team: 2003, in R. Bender and A. Renzini (eds.), *The Mass of Galaxies at Low and High Redshift*, p. 324

Erb, D. K., Shapley, A. E., Pettini, M., Steidel, C. C., Reddy, N. A., and Adelberger, K. L.: 2006, *ApJ* **644**, 813

Ferrarese, L., van den Bosch, F. C., Ford, H. C., Jaffe, W., and O'Connell, R. W.: 1994, *The Astronomical Journal* **108**, 1598

Freeman, K. C.: 1970, *ApJ* **160**, 811

Freeman, P. E., Izbicki, R., Lee, A. B., Newman, J. A., Conselice, C. J., Koekemoer, A. M., Lotz, J. M., and Mozena, M.: 2013, *MNRAS* **434**, 282

Gadotti, D. A.: 2009, *MNRAS* **393**, 1531

Galametz, A., Grazian, A., Fontana, A., Ferguson, H. C., Ashby, M. L. N., Barro, G., Castellano, M., Dahlen, T., Donley, J. L., Faber, S. M., Grogin, N., Guo, Y., Huang, K.-H., Kocevski, D. D., Koekemoer, A. M., Lee, K.-S., McGrath, E. J., Peth, M., Willner, S. P., Almaini, O., Cooper, M., Cooray, A., Conselice, C. J., Dickinson, M., Dunlop, J. S., Fazio, G. G., Foucaud, S., Gardner, J. P., Giavalisco, M., Hathi, N. P., Hartley, W. G., Koo, D. C., Lai, K., de Mello, D. F., McLure, R. J., Lucas, R. A., Paris, D., Pentericci, L., Santini, P., Simpson, C., Sommariva, V., Targett, T., Weiner, B. J., Wuyts, S., and the CANDELS Team: 2013, *ApJl Supp.* **206**, 10

Giavalisco, M., Ferguson, H. C., Koekemoer, A. M., Dickinson, M., Alexander, D. M., Bauer, F. E., Bergeron, J., Biagetti, C., Brandt, W. N., Casertano, S., Cesarsky, C., Chatzichristou, E.,

Conselice, C., Cristiani, S., Da Costa, L., Dahlen, T., de Mello, D., Eisenhardt, P., Erben, T., Fall, S. M., Fassnacht, C., Fosbury, R., Fruchter, A., Gardner, J. P., Grogin, N., Hook, R. N., Hornschemeier, A. E., Idzi, R., Jogee, S., Kretchmer, C., Laidler, V., Lee, K. S., Livio, M., Lucas, R., Madau, P., Mobasher, B., Moustakas, L. A., Nonino, M., Padovani, P., Papovich, C., Park, Y., Ravindranath, S., Renzini, A., Richardson, M., Riess, A., Rosati, P., Schirmer, M., Schreier, E., Somerville, R. S., Spinrad, H., Stern, D., Stiavelli, M., Strolger, L., Urry, C. M., Vandame, B., Williams, R., and Wolf, C.: 2004, *ApJl* **600**, L93

Grogin, N. A., Kocevski, D. D., Faber, S. M., Ferguson, H. C., Koekemoer, A. M., Riess, A. G., Acquaviva, V., Alexander, D. M., Almaini, O., Ashby, M. L. N., Barden, M., Bell, E. F., Bournaud, F., Brown, T. M., Caputi, K. I., Casertano, S., Cassata, P., Castellano, M., Challis, P., Chary, R.-R., Cheung, E., Cirasuolo, M., Conselice, C. J., Roshan Cooray, A., Croton, D. J., Daddi, E., Dahlen, T., Davé, R., de Mello, D. F., Dekel, A., Dickinson, M., Dolch, T., Donley, J. L., Dunlop, J. S., Dutton, A. A., Elbaz, D., Fazio, G. G., Filippenko, A. V., Finkelstein, S. L., Fontana, A., Gardner, J. P., Garnavich, P. M., Gawiser, E., Giavalisco, M., Grazian, A., Guo, Y., Hathi, N. P., Häussler, B., Hopkins, P. F., Huang, J.-S., Huang, K.-H., Jha, S. W., Kartaltepe, J. S., Kirshner, R. P., Koo, D. C., Lai, K., Lee, K.-S., Li, W., Lotz, J. M., Lucas, R. A., Madau, P., McCarthy, P. J., McGrath, E. J., McIntosh, D. H., McLure, R. J., Mobasher, B., Moustakas, L. A., Mozena, M., Nandra, K., Newman, J. A., Niemi, S.-M., Noeske, K. G., Papovich, C. J., Pentericci, L., Pope, A., Primack, J. R., Rajan, A., Ravindranath, S., Reddy, N. A., Renzini, A., Rix, H.-W., Robaina, A. R., Rodney, S. A., Rosario, D. J., Rosati, P., Salimbeni, S., Scarlata, C., Siana, B., Simard, L., Smidt, J., Somerville, R. S., Spinrad, H., Straughn, A. N., Strolger, L.-G., Telford, O., Teplitz, H. I., Trump, J. R., van der Wel, A., Villforth, C., Wechsler, R. H., Weiner, B. J., Wiklind, T., Wild, V., Wilson, G., Wuyts, S., Yan, H.-J., and Yun, M. S.: 2011, *ApJl Supp.* **197**, 35

Guo, Y., Ferguson, H. C., Giavalisco, M., Barro, G., Willner, S. P., Ashby, M. L. N., Dahlen, T., Donley, J. L., Faber, S. M., Fontana, A., Galametz, A., Grazian, A., Huang, K.-H., Kocevski, D. D., Koekemoer, A. M., Koo, D. C., McGrath, E. J., Peth, M., Salvato, M., Wuyts, S., Castellano, M., Cooray, A. R., Dickinson, M. E., Dunlop, J. S., Fazio, G. G., Gardner, J. P., Gawiser, E., Grogin, N. A., Hathi, N. P., Hsu, L.-T., Lee, K.-S., Lucas, R. A., Mobasher, B., Nandra, K., Newman, J. A., and van der Wel, A.: 2013, *ApJl Supp.* **207**, 24

Häussler, B., McIntosh, D. H., Barden, M., Bell, E. F., Rix, H.-W., Borch, A., Beckwith, S. V. W., Caldwell, J. A. R., Heymans, C., Jahnke, K., Jogee, S., Koposov, S. E., Meisenheimer, K., Sánchez, S. F., Somerville, R. S., Wisotzki, L., and Wolf, C.: 2007, *ApJl Supp.* **172**, 615

Henry, A., Scarlata, C., Domínguez, A., Malkan, M., Martin, C. L., Siana, B., Atek, H., Bedregal, A. G., Colbert, J. W., Rafelski, M., Ross, N., Teplitz, H., Bunker, A. J., Dressler, A., Hathi, N., Masters, D., McCarthy, P., and Straughn, A.: 2013, *ApJl* **776**, L27

Hubble, E. P.: 1922, *ApJ* **56**, 162

Hubble, E. P.: 1926, *ApJ* **64**, 321

Hubble, E. P.: 1936, *Realm of the Nebulae*

Im, M., Griffiths, R. E., Naim, A., Ratnatunga, K. U., Roche, N., Green, R. F., and Sarajedini, V. L.: 1999, *ApJ* **510**, 82

Im, M., Simard, L., Faber, S. M., Koo, D. C., Gebhardt, K., Willmer, C. N. A., Phillips, A., Illingworth, G., Vogt, N. P., and Sarajedini, V. L.: 2002, *ApJ* **571**, 136

Jedrzejewski, R. I.: 1987, *MNRAS* **226**, 747

Kartaltepe, J. S., Mozena, M., Kocevski, D., McIntosh, D. H., Lotz, J., Bell, E. F., Faber, S., Ferguson, H., Koo, D., Bassett, R., Bernyk, M., Blancato, K., Bournaud, F., Cassata, P., Castellano, M., Cheung, E., Conselice, C. J., Croton, D., Dahlen, T., de Mello, D. F., DeGroot, L., Donley, J., Guedes, J., Grogin, N., Hathi, N., Hilton, M., Hollon, B., Inami, H., Kassin, S., Koekemoer, A., Lani, C., Liu, N., Lucas, R. A., Martig, M., McGrath, E., McPartland, C., Mobasher, B., Morlock, A., Mutch, S., O'Leary, E., Peth, M., Pforr, J., Pillepich, A., Poole, G. B., Rizer, Z., Rosario, D., Soto, E., Straughn, A., Telford, O., Sunnquist, B., Weiner, B., and Wuyts, S.: 2014, *ArXiv e-prints*

Kennicutt, Jr., R. C.: 1998, *Annual Reviews of Astronomy and Astrophysics* **36**, 189

Kent, S. M., Dame, T. M., and Fazio, G.: 1991, *ApJ* **378**, 131

Kewley, L. J. and Ellison, S. L.: 2008, *ApJ* **681**, 1183

Kewley, L. J., Maier, C., Yabe, K., Ohta, K., Akiyama, M., Dopita, M. A., and Yuan, T.: 2013, *ApJl* **774**, L10

Koekemoer, A. M., Faber, S. M., Ferguson, H. C., Grogin, N. A., Kocevski, D. D., Koo, D. C., Lai, K., Lotz, J. M., Lucas, R. A., McGrath, E. J., Ogaz, S., Rajan, A., Riess, A. G., Rodney, S. A., Strolger, L., Casertano, S., Castellano, M., Dahlen, T., Dickinson, M., Dolch, T., Fontana, A., Giavalisco, M., Grazian, A., Guo, Y., Hathi, N. P., Huang, K.-H., van der Wel, A., Yan, H.-J., Acquaviva, V., Alexander, D. M., Almaini, O., Ashby, M. L. N., Barden, M., Bell, E. F., Bournaud, F., Brown, T. M., Caputi, K. I., Cassata, P., Challis, P. J., Chary, R.-R., Cheung, E., Cirasuolo, M., Conselice, C. J., Roshan Cooray, A., Croton, D. J., Daddi, E., Davé, R., de Mello, D. F., de Ravel, L., Dekel, A., Donley, J. L., Dunlop, J. S., Dutton, A. A., Elbaz, D., Fazio, G. G., Filippenko, A. V., Finkelstein, S. L., Frazer, C., Gardner, J. P., Garnavich, P. M., Gawiser, E., Gruetzbauch, R., Hartley, W. G., Häussler, B., Herrington, J., Hopkins, P. F., Huang, J.-S., Jha,

S. W., Johnson, A., Kartaltepe, J. S., Khostovan, A. A., Kirshner, R. P., Lani, C., Lee, K.-S., Li, W., Madau, P., McCarthy, P. J., McIntosh, D. H., McLure, R. J., McPartland, C., Mobasher, B., Moreira, H., Mortlock, A., Moustakas, L. A., Mozena, M., Nandra, K., Newman, J. A., Nielsen, J. L., Niemi, S., Noeske, K. G., Papovich, C. J., Pentericci, L., Pope, A., Primack, J. R., Ravindranath, S., Reddy, N. A., Renzini, A., Rix, H.-W., Robaina, A. R., Rosario, D. J., Rosati, P., Salimbeni, S., Scarlata, C., Siana, B., Simard, L., Smidt, J., Snyder, D., Somerville, R. S., Spinrad, H., Straughn, A. N., Telford, O., Teplitz, H. I., Trump, J. R., Vargas, C., Villforth, C., Wagner, C. R., Wandro, P., Wechsler, R. H., Weiner, B. J., Wiklind, T., Wild, V., Wilson, G., Wuyts, S., and Yun, M. S.: 2011, *ApJl Supp.* **197**, 36

Kormendy, J. and Kennicutt, Jr., R. C.: 2004, *Annual Reviews of Astronomy and Astrophysics* **42**, 603

Kriek, M., Shapley, A. E., Reddy, N. A., Siana, B., Coil, A. L., Mobasher, B., Freeman, W. R., de Groot, L., Price, S. H., Sanders, R., Shivaei, I., Brammer, G. B., Momcheva, I. G., Skelton, R. E., van Dokkum, P. G., Whitaker, K. E., Aird, J., Azadi, M., Kassis, M., Bullock, J. S., Conroy, C., Davé, R., Kereš, D., and Krumholz, M.: 2015, *ApJl Supp.* **218**, 15

Kriek, M., van Dokkum, P. G., Labbé, I., Franx, M., Illingworth, G. D., Marchesini, D., and Quadri, R. F.: 2009, *ApJ* **700**, 221

Laidler, V. G., Papovich, C., Grogin, N. A., Idzi, R., Dickinson, M., Ferguson, H. C., Hilbert, B., Clubb, K., and Ravindranath, S.: 2007, *Publications of the Astronomical Society of the Pacific* **119**, 1325

Lang, P., Wuyts, S., Somerville, R. S., Förster Schreiber, N. M., Genzel, R., Bell, E. F., Brammer, G., Dekel, A., Faber, S. M., Ferguson, H. C., Grogin, N. A., Kocevski, D. D., Koekemoer, A. M., Lutz, D., McGrath, E. J., Momcheva, I., Nelson, E. J., Primack, J. R., Rosario, D. J., Skelton, R. E., Tacconi, L. J., van Dokkum, P. G., and Whitaker, K. E.: 2014, *ApJ* **788**, 11

Lawrence, A., Warren, S. J., Almaini, O., Edge, A. C., Hambly, N. C., Jameson, R. F., Lucas, P., Casali, M., Adamson, A., Dye, S., Emerson, J. P., Foucaud, S., Hewett, P., Hirst, P., Hodgkin, S. T., Irwin, M. J., Lodieu, N., McMahon, R. G., Simpson, C., Smail, I., Mortlock, D., and Folger, M.: 2007, *MNRAS* **379**, 1599

Lilly, S., Schade, D., Ellis, R., Le Fèvre, O., Brinchmann, J., Tresse, L., Abraham, R., Hammer, F., Crampton, D., Colless, M., Glazebrook, K., Mallen-Ornelas, G., and Broadhurst, T.: 1998, *ApJ* **500**, 75

Lintott, C. J., Schawinski, K., Slosar, A., Land, K., Bamford, S., Thomas, D., Raddick, M. J., Nichol, R. C., Szalay, A., Andreescu, D., Murray, P., and Vandenberg, J.: 2008, *MNRAS* **389**,

1179

Lorenz, M. O.: 1905, *Publications of the American Statistical Association, Volume 9, Number 70, p. 209-219* **9**, 209

Lotz, J. M., Primack, J., and Madau, P.: 2004, *The Astronomical Journal* **128**, 163

MacArthur, L. A., Courteau, S., and Holtzman, J. A.: 2003, *ApJ* **582**, 689

Magnelli, B., Elbaz, D., Chary, R. R., Dickinson, M., Le Borgne, D., Frayer, D. T., and Willmer, C. N. A.: 2011, *Astronomy and Astrophysics* **528**, A35

Maier, C., Lilly, S. J., Ziegler, B. L., Contini, T., Pérez Montero, E., Peng, Y., and Balestra, I.: 2014, *ApJ* **792**, 3

Maiolino, R., Nagao, T., Grazian, A., Cocchia, F., Marconi, A., Mannucci, F., Cimatti, A., Pipino, A., Ballero, S., Calura, F., Chiappini, C., Fontana, A., Granato, G. L., Matteucci, F., Pastorini, G., Pentericci, L., Risaliti, G., Salvati, M., and Silva, L.: 2008, *Astronomy and Astrophysics* **488**, 463

Mannucci, F., Cresci, G., Maiolino, R., Marconi, A., and Gnerucci, A.: 2010, *MNRAS* **408**, 2115

Marleau, F. R. and Simard, L.: 1998, *ApJ* **507**, 585

Maseda, M. V., van der Wel, A., Rix, H.-W., da Cunha, E., Pacifici, C., Momcheva, I., Brammer, G. B., Meidt, S. E., Franx, M., van Dokkum, P., Fumagalli, M., Bell, E. F., Ferguson, H. C., Förster-Schreiber, N. M., Koekemoer, A. M., Koo, D. C., Lundgren, B. F., Marchesini, D., Nelson, E. J., Patel, S. G., Skelton, R. E., Straughn, A. N., Trump, J. R., and Whitaker, K. E.: 2014, *ApJ* **791**, 17

McLean, I. S., Steidel, C. C., Epps, H. W., Konidaris, N., Matthews, K. Y., Adkins, S., Aliado, T., Brims, G., Canfield, J. M., Cromer, J. L., Fucik, J., Kulas, K., Mace, G., Magnone, K., Rodriguez, H., Rudie, G., Trainor, R., Wang, E., Weber, B., and Weiss, J.: 2012, in *Society of Photo-Optical Instrumentation Engineers (SPIE) Conference Series*, Vol. 8446 of *Society of Photo-Optical Instrumentation Engineers (SPIE) Conference Series*, p. 0

Méndez-Abreu, J., Aguerri, J. A. L., Corsini, E. M., and Simonneau, E.: 2008, *Astronomy and Astrophysics* **478**, 353

Nayyeri, H.: in prep.

Noeske, K. G., Weiner, B. J., Faber, S. M., Papovich, C., Koo, D. C., Somerville, R. S., Bundy, K., Conselice, C. J., Newman, J. A., Schiminovich, D., Le Floc'h, E., Coil, A. L., Rieke, G. H., Lotz, J. M., Primack, J. R., Barmby, P., Cooper, M. C., Davis, M., Ellis, R. S., Fazio, G. G., Guhathakurta, P., Huang, J., Kassin, S. A., Martin, D. C., Phillips, A. C., Rich, R. M., Small, T. A., Willmer, C. N. A., and Wilson, G.: 2007, *ApJl* **660**, L43

Oke, J. B. and Gunn, J. E.: 1983, *ApJ* **266**, 713

Oohama, N., Okamura, S., Fukugita, M., Yasuda, N., and Nakamura, O.: 2009, *ApJ* **705**, 245

Patterson, F. S.: 1940, *Harvard College Observatory Bulletin* **914**, 9

Peng, C. Y., Ho, L. C., Impey, C. D., and Rix, H.-W.: 2002, *The Astronomical Journal* **124**, 266

Peng, C. Y., Ho, L. C., Impey, C. D., and Rix, H.-W.: 2010, *The Astronomical Journal* **139**, 2097

Peth, M. A., Lotz, J. M., Freeman, P. E., McPartland, C., Mortazavi, S. A., Snyder, G. F., Grogin, N. A., Guo, Y., Hemati, S., Karteltepe, J. S., Kocevski, D. D., Koekemoer, A. M., McIntosh, D. H., Nayyeri, H., Papovich, C., Primack, J. R., Simons, R. C., and van der Wel, A.: 2015, *ArXiv e-prints*

Petrosian, V.: 1976, *ApJl* **209**, L1

Pettini, M. and Pagel, B. E. J.: 2004, *MNRAS* **348**, L59

Pignatelli, E., Fasano, G., and Cassata, P.: 2006, *Astronomy and Astrophysics* **446**, 373

Ravindranath, S., Ferguson, H. C., Conselice, C., Giavalisco, M., Dickinson, M., Chatzichristou, E., de Mello, D., Fall, S. M., Gardner, J. P., Grogin, N. A., Hornschemeier, A., Jogee, S., Koekemoer, A., Kretchmer, C., Livio, M., Mobasher, B., and Somerville, R.: 2004, *ApJl* **604**, L9

Ravindranath, S., Giavalisco, M., Ferguson, H. C., Conselice, C., Katz, N., Weinberg, M., Lotz, J., Dickinson, M., Fall, S. M., Mobasher, B., and Papovich, C.: 2006, *ApJ* **652**, 963

Reddy, N. A., Kriek, M., Shapley, A. E., Freeman, W. R., Siana, B., Coil, A. L., Mobasher, B., Price, S. H., Sanders, R. L., and Shivaei, I.: 2015, *ArXiv e-prints*

Sandage, A.: 1961, *The Hubble atlas of galaxies*

Sanders, R. L., Shapley, A. E., Kriek, M., Reddy, N. A., Freeman, W. R., Coil, A. L., Siana, B., Mobasher, B., Shivaei, I., Price, S. H., and de Groot, L.: 2015, *ApJ* **799**, 138

Schade, D., Lilly, S. J., Crampton, D., Ellis, R. S., Le Fèvre, O., Hammer, F., Brinchmann, J., Abraham, R., Colless, M., Glazebrook, K., Tresse, L., and Broadhurst, T.: 1999, *ApJ* **525**, 31

Scoville, N., Aussel, H., Brusa, M., Capak, P., Carollo, C. M., Elvis, M., Giavalisco, M., Guzzo, L., Hasinger, G., Impey, C., Kneib, J.-P., LeFevre, O., Lilly, S. J., Mobasher, B., Renzini, A., Rich, R. M., Sanders, D. B., Schinnerer, E., Schminovich, D., Shopbell, P., Taniguchi, Y., and Tyson, N. D.: 2007, *ApJl Supp.* **172**, 1

Sersic, J. L.: 1968, *Atlas de galaxias australes*

Shivaei, I., Reddy, N. A., Shapley, A. E., Kriek, M., Siana, B., Mobasher, B., Coil, A. L., Freeman, W. R., Sanders, R., Price, S. H., de Groot, L., and Azadi, M.: 2015, *ArXiv e-prints*

Simard, L.: 1998, in R. Albrecht, R. N. Hook, and H. A. Bushouse (eds.), *Astronomical Data Analysis Software and Systems VII*, Vol. 145 of *Astronomical Society of the Pacific Conference Series*, p. 108

Simard, L., Koo, D. C., Faber, S. M., Sarajedini, V. L., Vogt, N. P., Phillips, A. C., Gebhardt, K., Illingworth, G. D., and Wu, K. L.: 1999, *ApJ* **519**, 563

Skelton, R. E., Whitaker, K. E., Momcheva, I. G., Brammer, G. B., van Dokkum, P. G., Labbé, I., Franx, M., van der Wel, A., Bezanson, R., Da Cunha, E., Fumagalli, M., Förster Schreiber, N., Kriek, M., Leja, J., Lundgren, B. F., Magee, D., Marchesini, D., Maseda, M. V., Nelson, E. J., Oesch, P., Pacifici, C., Patel, S. G., Price, S., Rix, H.-W., Tal, T., Wake, D. A., and Wuyts, S.: 2014, *ApJl Supp.* **214**, 24

Stanford, S. A., Dickinson, M., Postman, M., Ferguson, H. C., Lucas, R. A., Conselice, C. J., Budavári, T., and Somerville, R.: 2004, *The Astronomical Journal* **127**, 131

Steidel, C. C., Rudie, G. C., Strom, A. L., Pettini, M., Reddy, N. A., Shapley, A. E., Trainor, R. F., Erb, D. K., Turner, M. L., Konidaris, N. P., Kulas, K. R., Mace, G., Matthews, K., and McLean, I. S.: 2014, *ApJ* **795**, 165

Stetson, P. B.: 1987, *Publications of the Astronomical Society of the Pacific* **99**, 191

Taylor-Mager, V. A., Conselice, C. J., Windhorst, R. A., and Jansen, R. A.: 2007, *ApJ* **659**, 162

Tremonti, C. A., Heckman, T. M., Kauffmann, G., Brinchmann, J., Charlot, S., White, S. D. M., Seibert, M., Peng, E. W., Schlegel, D. J., Uomoto, A., Fukugita, M., and Brinkmann, J.: 2004, *ApJ* **613**, 898

Trujillo, I. and Aguerri, J. A. L.: 2004, *MNRAS* **355**, 82

van den Bergh, S.: 2001, *The Astronomical Journal* **122**, 621

Williams, R. J., Quadri, R. F., Franx, M., van Dokkum, P., and Labbé, I.: 2009, *ApJ* **691**, 1879

Windhorst, R. A., Taylor, V. A., Jansen, R. A., Odewahn, S. C., Chiarenza, C. A. T., Conselice, C. J., de Grijs, R., de Jong, R. S., MacKenty, J. W., Eskridge, P. B., Frogel, J. A., Gallagher, III, J. S., Hibbard, J. E., Matthews, L. D., and O'Connell, R. W.: 2002, *ApJl Supp.* **143**, 113

Wuyts, S., Förster Schreiber, N. M., van der Wel, A., Magnelli, B., Guo, Y., Genzel, R., Lutz, D., Aussel, H., Barro, G., Berta, S., Cava, A., Graciá-Carpio, J., Hathi, N. P., Huang, K.-H., Kocevski, D. D., Koekemoer, A. M., Lee, K.-S., Le Floc'h, E., McGrath, E. J., Nordon, R., Popesso, P., Pozzi, F., Riguccini, L., Rodighiero, G., Saintonge, A., and Tacconi, L.: 2011, *ApJ* **742**, 96

Wyse, R. F. G., Gilmore, G., and Franx, M.: 1997, *Annual Reviews of Astronomy and Astrophysics* **35**, 637

Xue, Y. Q., Luo, B., Brandt, W. N., Bauer, F. E., Lehmer, B. D., Broos, P. S., Schneider, D. P., Alexander, D. M., Brusa, M., Comastri, A., Fabian, A. C., Gilli, R., Hasinger, G., Hornschemeier, A. E., Koekemoer, A., Liu, T., Mainieri, V., Paolillo, M., Rafferty, D. A., Rosati, P., Shemmer, O., Silverman, J. D., Smail, I., Tozzi, P., and Vignali, C.: 2011, *ApJl Supp.* **195**, 10

Zhu, Y.-N., Wu, H., Cao, C., and Li, H.-N.: 2008, *ApJ* **686**, 155

Appendix

A1 PSF Construction Using IRAF

Point-spread functions (PSFs) play a very important role in many techniques of measuring parametric morphology. The convolution of the model galaxy with the PSF is meant to represent seeing of the telescope, and an inaccurate PSF can produce incorrect surface brightness distributions. The process of creating a PSF using the IRAF DAOPHOT package (Stetson, 1987) is done using a simple combination of packages, but first a list of isolated, unsaturated stars must be obtained. I have found that the best results come from stacking stars in IRAF using a minimum of 5 stars, and large mosaic images are ideal for this. To first obtain a sample of just the stars in the image, I use the class_star parameter from a SExtractor catalog, and select objects with class_star ≥ 0.9, or higher if the limit of 0.9 provides too many stars. I first investigate the stars visually to determine if there are any contaminating galaxies/objects that would lead to irregularities in a stacked-star PSF, and remove those stars with contamination from my sample. Finally, I inspect the remaining stars using "imexamine" in IRAF to determine if the stars are saturated or not, as can be seen in the surface plots. If the surface plot, taken from the center of the star, plateaus at the top, that is an indication of saturation, and the star should be excluded from the sample. The DAOPHOT package FIND can also be used to create a star list. For further details about the FIND package please see Stetson (1987).

Once the star list is finalized, four main packages can be used in IRAFs DAOPHOT package to create a stacked-star PSF for the image. The DAOPHOT package can be found in IRAF under the DIGIPHOT package which is part of the NOAO package. The first package used in creat-

ing the PSF is PHOT. This package performs aperture photometry and returns crude apparent-magnitude estimates and sky determinations for the list of stars returned in a '.mag' file. This requires the image that the PSF is being created for as well as the list of image x and y coordinates of the stars in a text file. The next package is PSTSELECT, which selects the PSF candidate stars and generates a .pst file. This can be done interactively, for which the package will go through all of the star individually showing surface, radial, and contour plots enabling the user to choose to accept or remove that star as a candidate. Seeing as I do this step before using the DAOPHOT package altogether, I use PSTSELECT in non-interactive mode to generate the output file, to be used in the next package. The third package used in generating a psf through IRAF is the PSF package. This task builds the PSF using stars selected as indicated by the input files from the first two packages described. This task stores the information in the image header as a 2D analytic function. The final task, SEEPSF, takes this output file and generates a PSF image. The last step is to normalize the generated PSF, which can be done quickly by using the IRAF task IMARITH. By obtaining the image statistics of the number of pixels, NPIX, and the average pixel value, IMARITH can be used to divide the PSF image from SEEPSF by the product of these two image statistics.

During this process, a few other parameters must be taken into account. In particular, the parameter set task DAOPARS has many optional inputs, but I always make sure to define the psf radius in scale units, PSFRAD, and check to make sure a gaussian function is being used to create the PSF. I also suggest setting the zeropoint magnitude, zmag, in the photometry parameters, PHOTPARS. By following these procedures carefully, an intrinsic PSF can be obtained as long as enough isolated stars are available in the image.

A2 Bulge-to-Total Flux Ratio Definition

Throughout this work, I discuss the measured bulge-to-total flux ratio, B/T, of the galaxy samples. The B/T is determined using the measured apparent magnitudes of the bulge and disk components from the parametric fits using GALFIT. First the apparent (AB) magnitudes are converted into fluxes using

$$F = 10^{-0.4(m-zp)},$$

where F is the flux, m is the magnitude, and zp is the photometric zeropoint. The B/T is then determined using the formula

$$B/T = \frac{F_B}{F_D + F_B},$$

where B and D represent the bulge and disk components, respectively.